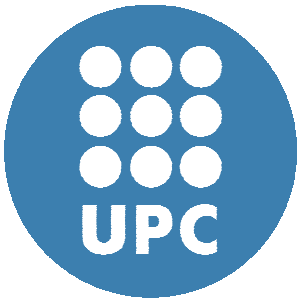

CIRAM
Centro Interdipartimentale
di Ricerca Ambiente

UNIVERSITA' DEGLI STUDI DI NAPOLI "FEDERICO II"
C.I.R.Am. – Centro Interdipartimentale di Ricerca Ambiente

UNIVERSITAT POLITÈCNICA DE CATALUNYA
RSLab - Remote Sensing Laboratory

Dottorato di Ricerca in Analisi dei Sistemi Ambientali
XXV Ciclo

Application of DInSAR data for slow-moving landslides monitoring

Tutors:
Ing. Massimo Ramondini
Prof. Jordi J. Mallorqui
Co-Tutor
Prof. Domenico Calcaterra

Coordinatore della Scuola di dottorato
Prof. Maurizio Fedi

Contents

CHAPTER 1

1. Introduction

Landslides are among the most important and most frequent natural calamities. After earthquakes, they cause the highest number of victims and of damages to man-built structures.

Thus, landslides risk assessment and prevention is the key step to correct territory planning and management, as witnessed by growing scientific evidence in this field.

Landslides' studies rely first of all on territory monitoring, essential for the detection of at-risk phenomena. Territory monitoring is a complex and dynamic process, which requires continuous technological adjustments in order to obtain the most precise and up-to-date information on natural events and on their evolution. Identification of the most efficacious monitoring system is difficult and it is based on the one that best meets technical, logistical and economic requirements of the local community and needing careful cost-benefits analyses.

Owing to the high number of contributing factors, the optimization of monitoring processes is known to be quite complex. Integrated monitoring networks for the assessment of mass movements are thus being developed in order to obtain useful information on both triggering factors and magnitude of the studied phenomenon. Such networks also include technical and logistical aspects.

Final comparison of the results obtained from the application of different methods allows to achieve their validation.

The present study develops in the above-mentioned field. In detail, this work focuses on Remote Sensing, on its potential as an additional monitoring technique and as an alternative method, at least in preliminary phenomena evaluations, to traditional ground monitoring systems.

Remote sensing studies complex territorial contexts by means of spectral sensors located at high distances from the analyzed object. There are two kind of sensors; one, named passive sensor, measures energy that is naturally available. Such sensors can only be used to detect energy when the naturally occurring energy is available and this can only take place while the sun illuminates the Earth (optical sensors). Active sensors, on the other hand, transmit short bursts or 'pulses' of electromagnetic energy in the direction of interest and record the origin and strength of the backscatter received from objects within the system's field of view (SAR sensons).

Over the past fifty years many changes have occurred: from the initial uniband sensors installed on meteorological platforms, bearing kilometrical spatial resolutions, nowadays commercial platforms, such as the American GeoEye, WorldView and Quickbird, are available.

These modern systems produce multispectral images with sub-metric ground pixel resolution in the panchromatic band. Satellite technology development, together with images elaboration and classification methods, have allowed Remote sensing applications to extend to many fields, such as environmental monitoring, risk analyses and territory planning.

This work analyzes a specific type of landslide event, the slow- or intermittent-moving phenomena on territorial scale. Monitoring and parameterization of these dynamic processes are particularly relevant: for instance, ground velocity maps may significantly affect territory planning and urban development, or they may help in post-event damages evaluation. Remote sensing has proved to be highly suitable for these and for many other necessities, since it captures data "from above" in form of images that cover vast study areas.

Among the different types of Remote sensing techniques, one that very well meets dynamic processes' requirements is the Interferometry SAR (InSAR). This branch of Remote sensing uses active monitoring sensors that measure the backscattering radiation produced by the sensor-originated impulse directed to the Earth's surface. Such systems use radar antenna that are able to produce and receive electromagnetic signals; in detail, modern satellites are equipped with Synthetic Aperture Radar (SAR) sensors which can obtain good ground resolution. The images obtained from a SAR is composed by the amplitude which depends on the scene reflectivity and the phase, among others, is proportional to the two-way distance from satellite to ground.

InSAR is the method used to process SAR generated images and it is based on the combination between one or more pairs of satellite images whose orbital parameters are all known. The combination of two SAR images of the same scene acquired from different orbits, i.e., incidence angles, produces an interferogram. The interferogram is obtained by multiplying one image by the complex conjugate of the other and contains, on a pixel by pixel basis, the phase difference between the two acquisitions (Massonet et al.,1993). This phase difference can be exploited in combination with the orbital information for each acquisition to derive a Digital Elevation Model (DEM) of the scene. If the latter is already known, InSAR allows to calculate the terrain displacement.

Over the past twenty years, SAR technology has greatly improved and many satellite constellations have been launched: ERS1/2 and ENVISTAT ASAR (European Space Agency), JERS-1 SAR (Japanese Aerospace Exploration Agency), RADARSAT-1/2 (Canadian Space Agency), TerraSAR-X and TanDEM-X (Infoterra (Germany)), and COSMO-SKYMed (Italian

Space Agency) (Fig. 1.1). This has allowed the scientific community to develop image processing algorithms which produce increasingly reliable velocity maps and temporal series of deformation.

Moreover, the availability of a now several decades long (since 1992) images archive made it possible to reconstruct the history and evolution of previously not monitored landslides.

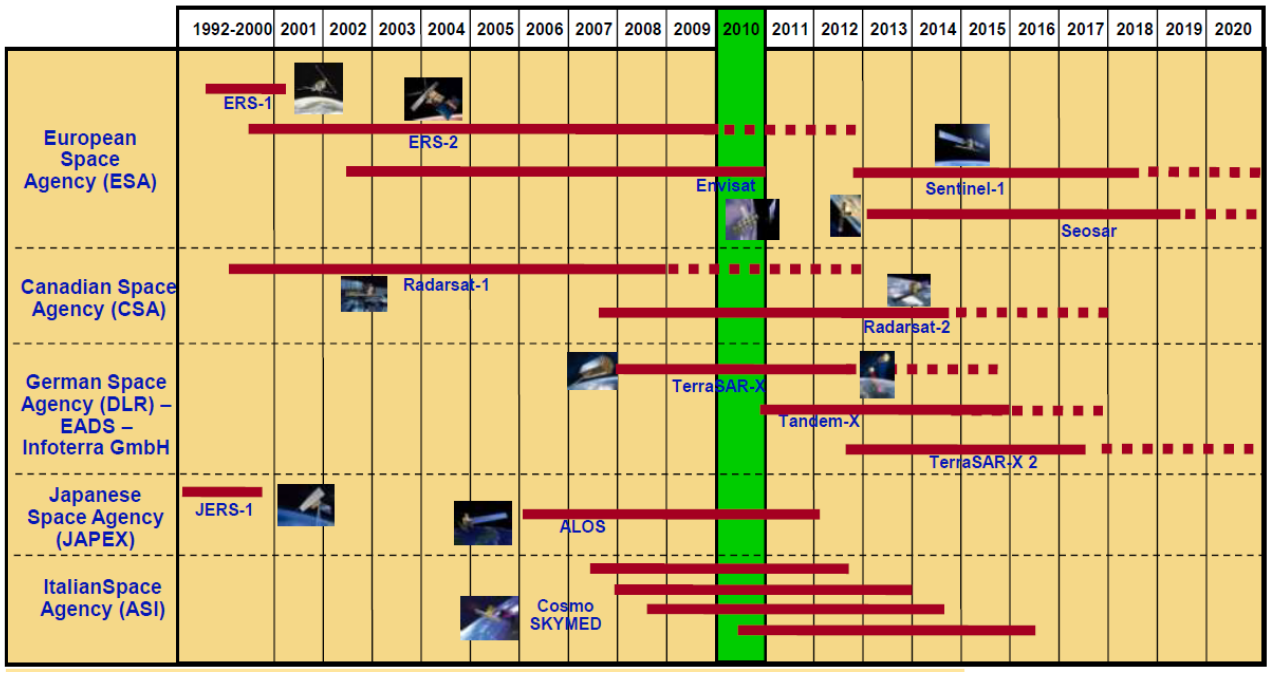

Figure 1.1: Temporal schedule of the most important SAR missions.

The growing use of such innovative technologies is nowadays frequently limited to aseptic data elaborations that do not take into account the geological, geomorphological, geotechnical and hydraulic characteristics of the observed area, which, instead, are fully considered by traditional monitoring systems. Therefore, if in one hand satellite data have to be precisely processed, on the other data control and validation procedures will be needed and are based on the comparison with traditionally acquired data and on careful on-site surveys. Such information has to be integrated from the very beginning in the SAR processing in order to achieve its optimization.

1.1 Structure of the thesis

The thesis develops in six chapters.

The first chapter briefly depicts landslides related problems and provides the description of the purpose of the research project and the thesis' summary.

The second chapter explains the basic elements of landslides' mechanisms/dynamics from both geological and geotechnical points of view.

The third chapter illustrates the different landslides monitoring systems.

The fourth chapter provides a detailed description of the SAR Remote sensing technique with regard to both platforms and sensors characteristics and different data processing systems.

The fifth chapter shows the application of DInSAR to the four studied sites (Calitri, Moio della Civitella, Costa della Gaveta, and Agnone). Two types of images were processed: old generation ENVISTAT ASAR images of ESA and last generation Very High Resolution images acquired from the Cosmo-SkyMed satellite constellation of ASI.

The sixth and last chapter illustrates the work's conclusions and provides a critical analysis of the obtained results. Furthermore, it identifies possible future applications of the studied technology.

Finally, the Appendix is a short tutorial of SUBSIDENCE for end-users.

1.2 Objectives

The aim of this work is to evaluate the applicability of satellite interferometry monitoring in the center-southern Italian Appennine. This area is characterized by structurally complex geological formations that give rise to slow to extremely slow velocity deformative phenomena, which can be well studied with SAR-based monitoring technique.

A preliminary, detailed study of the different SAR data processing techniques and available algorithms was made in order to detect limits and potentials of each one. Velocity maps and deformation time series were then elaborated in order to evaluate phenomena extension and activity and consequently to define the events' evolution. Finally, the obtained results were compared with ancillary data, where available, for validation. Ancillary data included inclinometer data, GPS, topographic measurements and rain data which, in some cases, allowed a better phenomena interpretation.

Studied sites displayed representative phenomena and were sufficiently supplied with traditional monitoring data. Four experimental study sites were identified and are listed below (Fig. 1.2):

- Calitri (Campania Region - Avellino Province), interested by the presence of a huge complex landslide, reactivated after the main shock of the M = 6.9 November 23, 1980 earthquake;

- Moio della Civiltella (Campania Region - Salerno Province) where two urban centres, Moio and Pellare are interested by slide-flows and roto-translational slides;

- Potenza, Costa della Gaveta zone (Basilicata Region) involved by many complex mass movements occurred on the northern slope of the Basento River valley;

- Agnone (Molise Region - Isernia Province) where in the catchment of the Vallone S. Nicola, a complex slope movement, to be considered as a reactivation of a pre-existing landslide, took place as a consequence of an intense rainfall event occurred on January 2003.

For each of these sites, available data have been elaborated by means of the processing procedures that best allowed objective data interpretation.

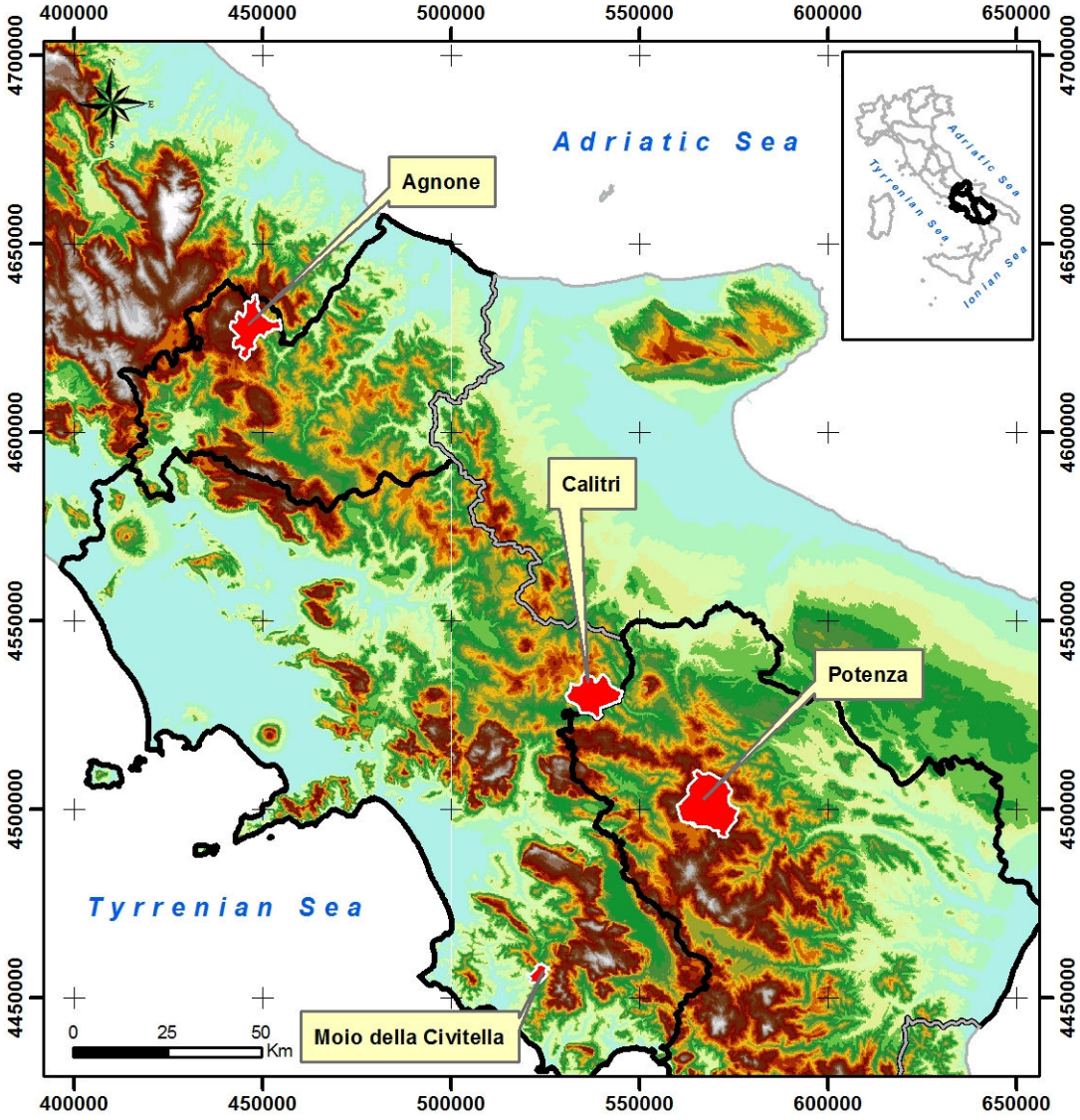

Figure 1.2: Location of the case studies, Agnone (IS), Calitri (AV), Moio della Civitella (SA) and Costa della Gaveta (PT).

CHAPTER 2

2. Landslides

Landslides are a major hazard because they are widespread. It has been calculated that approximately 3.7 million km^2 of the Earth fall in "exposed" areas; of these, 820 000 km^2 represent high risk zones. Moreover, as urban and infrastructures development has expanded to hillside areas, the landslides exposed population counts approximately 300 million individuals (4-5% of world population), with 66 million people living in high risk zones (Fig. 2.1).

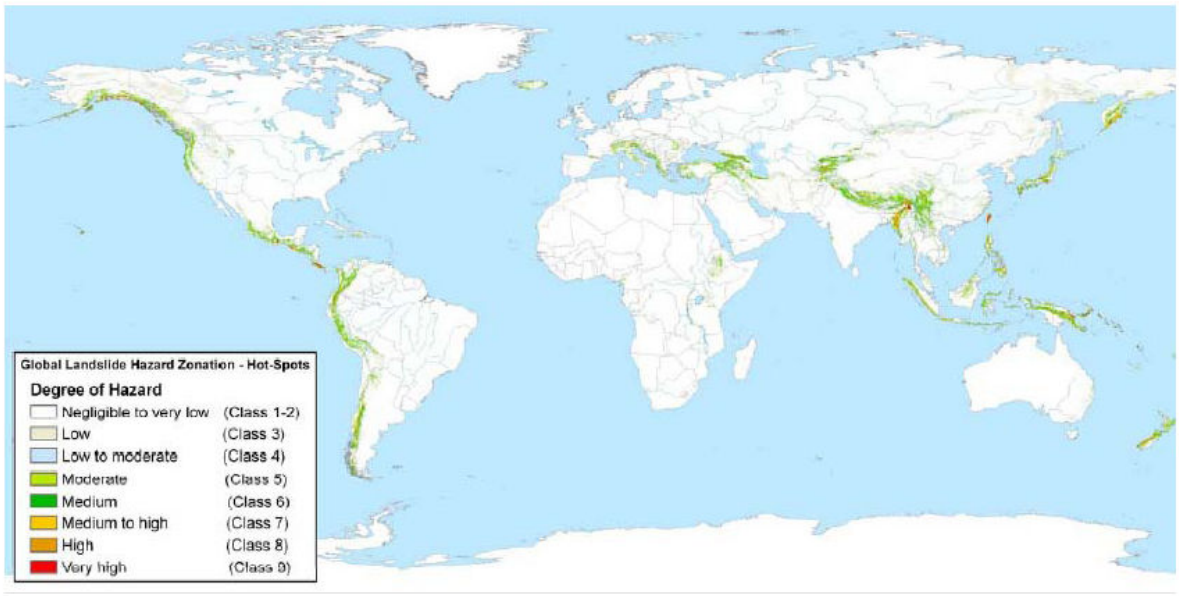

Figure 2.1: Global landslide Hazard zonation (Nadim et al., 2006)

2.1 Definition and classification

A landslide represents "the movement of a mass of rock, debris or earth down a slope" accordingly to Varnes 1978 and Cruden 1991. The phenomena described as landslides are not limited to either "land" or "sliding", and the use of the word has implied a much more extensive meaning than its component parts suggest. It has to be pointed out that ground subsidence and collapse are excluded from this definition.

Landslide classification is based on Varnes (1978) system which contemplates two terms: the first term describes the material type and the second one describes the type of movement.

The material types which can be involved in a landslide are rock, earth and debris, being classified as follows:

- Rock: is “a hard or firm mass that was intact and in its natural place before the initiation of movement.”
- Soil: is “an aggregate of solid particles, generally of minerals and rocks, which either was transported or was formed by the weathering of rock in place. Gases or liquids filling the pores of the soil form part of the soil.”
- Earth: “describes material in which 80% or more of the particles are smaller than 2 mm, the upper limit of sand sized particles.”
- Debris: “contains a significant proportion of coarse material; 20% to 80% of the particles are larger than 2 mm and the remainder is less than 2 mm.”

It is important to point out that material types should describe the displaced material in the landslide before the event occurs.

The types of movement describe how the landslide movement is distributed through the displaced mass (Cruden & Varnes 1996). The five cinematically distinct types of movement are described in the sequence fall, topple, slide, spread and flow. Table 2.1.1 and Figure 2.1.1 show how the two terms are combined to give the landslide type.

Table 2.1.1: Mass movement classification based on process type and material (Cruden and Varnes 1996; Dikau et al.1996)

Process type		Type of material		
		Rock	Debris	Earth
Topple		Rock topple	Debris topple	Earth topple
Fall		Rock fall	Debris fall	Earth fall
Slide	Translational	Rock slide	Debris slide	Earth slide
	Rotational			
Flow		Rock flow	Debris flow	Earth flow
Spread		Rock spread	Debris spread	Earth spread
Complex		e.g., rock avalanche	e.g., flow slide	e.g., slump-earthflow

In order to analyze the phenomenon and then to carry out better procedures to prevent or mitigate the landslide hazard, more information about its type and velocity become useful. The velocity of the mass movement is one of the most important aspects in landslide studies. In the table 3.1.2, as described by Cruden & Varnes in 1996, seven classes of velocity have been identified,

from extremely rapid events whose rate can exceed the speed of a person running (5 m/sec) to extremely slow events (below 16 mm/year) that are imperceptible without appropriate instruments.

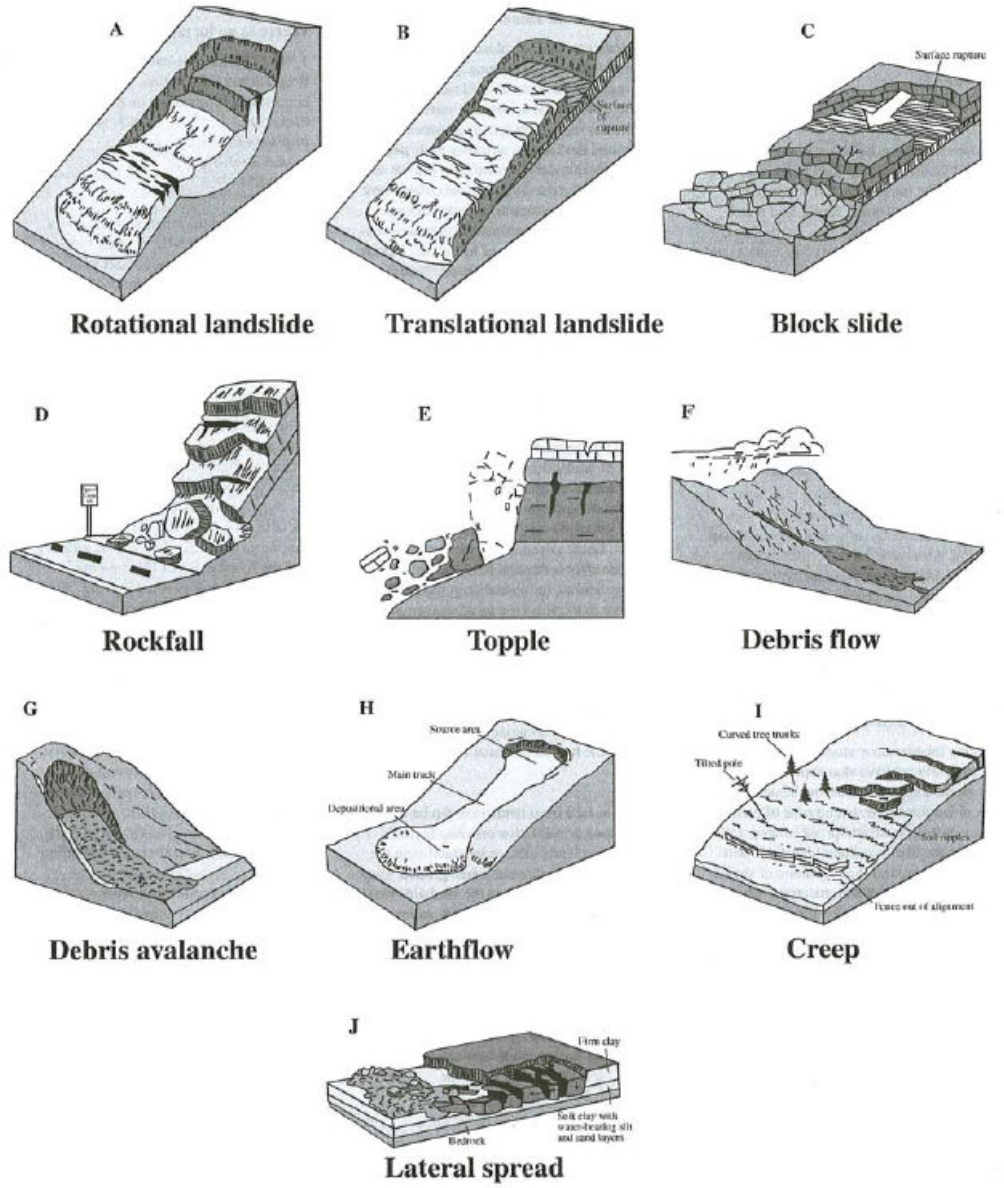

Figure 2.1.1: Mass movement classification (Cruden and Varnes, 1996).

Table 2.1.2 also shows the importance of the velocity factor with respect to the identification of landslides risk mitigation procedures. A complete picture is offered, for instance, by several relatively frequent phenomena which took place in the Italian center-southern Appennine: on one hand the debris flows that involved pyroclastic deposits resting over carbonate ridges, at the end of the 1990s (Sarno - 1998, Quindici - 1998 and Cervinara – 1999), which caused many victims and considerable damage. On the other, large slope instability phenomena characterized by slow to

extremely slow velocity that involved slopes in structurally complex formations (Calitri – 1980, Agnone - 2003), which caused no victims, but only damage to man-built structures, and which allows the population's coexistence.

Table 2.1.2: Mass movement classification based on velocity of displacement (after Cruden and Varnes 1996).

Class	Description	Typical velocity	Expected damages and population reaction
1	Extremely rapid	>5 m/sec	Disaster of major violence; buildings destroyed by impact of displaced material; many deaths; escape unlikely
2	Very rapid	>3 m/min	Some lives lost; velocity too great to permit all persons to escape
3	Rapid	>1.8 m/h	Escape evacuation possible; structures destroyed
4	Moderate	>13 m/month	Some temporary and insensitive structures can be temporarily maintained
5	Slow	>1.6 m/year	Remedial constructions can be undertaken during movement; insensitive structures can be maintained with frequent maintenance work if total movement is not large during a particular acceleration phase
6	Very slow	>15 mm/year	Some permanent structures undamaged by movement
7	Extremely slow	<15 mm/year	Imperceptible without instruments; construction possible with precautions

Examples above described show that the effects on people and structures, deriving from event, are connected with landslide velocity. Therefore, considering the types of movement and the velocity classes, new definitions are given by Cruden & Varnes (1996):

a) Fall: this landslide, whose velocity varies from very rapid to extremely rapid, consists in the detachment of rock or soil from steep slopes, that can be preceded by a small slide or topple of the material involved; subsequently, the detached material moves mainly in the air, going down by falling, bouncing or rolling. The dominance of one of these movement's modes will depend upon the slope: free fall can occur if the involved slope is characterized by angle > 76°; decreasing of the slope angle will cause a transition to bouncing and, then, to rolling when angles ≤ 45° are reached. It is clear that local slope variations may infer on the modes of movements (Hungr & Evans, 1988).
b) Topple: in this case, the movement, that can assume velocities from extremely slow to extremely rapid, is a rotation around a point/axis below the gravity centre of the involved mass of soil or rock. Subsequently, the phenomenon can evolve into fall or slide, depending

on the geometry of the surface of separation and of the displacing mass as well, and also on the orientation and extent of the discontinuities.

c) Slide: a slide indicates a downslope movement of soil or rock that mainly occurs on zones of intense shear strain or along a rupture surface, usually starting by local failures on the ground that subsequently will enlarge forming the main scarp of the landslide. By depending on the shape of the surface of rupture, rotational and translational slides can be distinguished (Varnes, 1978), moving along a curve and planar surface, respectively. In the first case, the ratio between the depth of the surface of rupture and its length ranges usually in the interval $0.15 \div 0.33$ (Skempton & Hutchinson, 1969); the slope failure follows inhomogeneities and discontinuities eventually present in the material involved by landslide (Varnes, 1978). In the case of translational slide, that are usually shallower than rotational, the ratio of depth of the surface of rupture to its length is less than 0.1 (Skempton & Hutchinson, 1969). Moreover, rotational and translational slides show different behaviors, that need to be taken into account in the stability analysis and control measures: while the first ones, in fact, tend to restore the equilibrium of the sliding mass, the translational phenomena can continue to move on long slopes, depending upon the inclination of the surface of rupture, and frequently, if the velocity and water content increase, can evolve into a flow.

d) Lateral Spread: it describes the lateral extension of soil or rock mass combined with the subsidence in softer and more plastic underlying material. Spreads involving rock do not show the presence of a defined surface of rupture, while phenomena occurring in cohesive soils can result from liquefaction or plastic flowing of the underlying material (Varnes, 1978).

e) Flow: these phenomena have kinematics and distribution of velocities in the landslide body similar to those of a viscous liquid. They are characterized by continuous movement in which shear surfaces are not usually preserved. Differently than in a slide, considerable deformations can interest the body of a flow. As above highlighted, flows can derive from slide movements, when the moving material presents an increase of water amount and a decrease of its cohesion, or when it encounters steeper slopes, leading in this case even to an increase of the potential damages on the affected territory.

2.2 Landslide causes

The great variety of slope movements reflects the diversity of conditions that cause the slope to become unstable and the many processes that trigger the movement. Opposite forces face

themselves inside all slopes: on one hand there are forces which promote the downslope movement and on the other, there are forces which tend to resist to it. The stability of a slope depends on the balance between the downslope shear stress and the shear strength of the soil, along a sliding surface. On the basis of such theory, two main landslide causes categories have been identified (Terzaghi, 1950): external factors, which result in an increase of the shearing stress (e.g. geometrical changes, unloading the slope toe, loading the slope crest, shocks and vibrations, drawdown, changes in water regime) and internal factors which result in a decrease of the shearing resistance (e.g. progressive failure, weathering, seepage erosion). Hardly ever landslides take place because of only one factor. Actually, ground conditions alone (weak strength, sensitive fabric, degree of weathering and fracturing) cannot be considered as causes, but rather as significant contributors, being necessary for an unstable slope to develop, in addition to environmental criteria of stress, pore water pressure and temperature.

The process leading to the development of the slide begins with the formation of the rock itself, when its basic properties are determined and includes all the subsequent events of crustal movement, erosion and weathering (Varnes, 1978). For this reason, and from the physical point of view, it is more correct to consider three stages of slopes' stability: stable, marginally stable and actively unstable (Crozier, 1986). Stable slopes are those in which stability forces are sufficiently strong and higher than the destabilizing ones. Marginally stable slopes are those in which destabilizing forces reach a certain level of activity and prevail some time on stability forces.

Finally, actively unstable slopes are those in which destabilizing forces produce continuous or intermittent movement. The transition from one stage to another is the result of two causal factors categories:

1. Preparatory causal factors which make the slope susceptible to movement without actually initiating it and thereby tending to place the slope in a marginally stable state.
2. Triggering causal factors which initiate movement. The causal factors shift the slope from a marginally stable to an actively unstable state.

A simple classification system of landslide causal factors is useful because landslide causes assessment is complex and landslides are not always investigated in great detail. The operational approach proposed by the WP/WLI Working Group on Causes of Landslides (WP/WLI, 1994) covers the majority of landslides and considers the available data from simple site investigation and information furnished by other site observations.

Landslide causal factors are divided according to their effect (preparatory or triggering) and their origin (ground conditions and geomorphological, physical or man-made processes). Ground conditions may not have a triggering function, while any ground condition or process may have a

preparatory function. Table 2.2.1 is a short checklist of landslide causal factors arranged in four practical groups.

Ground conditions or the material and mass characteristics of the ground, can be mapped on the surface of the landslide and in the surrounding ground and explored in the subsurface by drilling and trenching. Mechanical characteristics can be determined by testing.

Geomorphological processes, or changes in the morphology of the ground, can be documented by pre-existing maps, aerial photographs, surveys of the landslide, or careful observation over time by the local population.

Physical processes concern the environment and can be documented at the site by instrumentation, such as rainfall, earthquake, seismographs or piezometers.

Table 2.2.1. A landslide causal factors (after Popescu M.E., Seve G., 2001).

1. GROUND CONDITIONS
(1) Plastic weak material
(2) Sensitive material
(3) Collapsible material
(4) Weathered material
(5) Sheared material
(6) Jointed or fissured material
(7) Adversely oriented mass discontinuities (including bedding, schistosity, cleavage)
(8) Adversely oriented structural discontinuities (including faults, unconformities, flexural shears, sedimentary contacts)
(9) Contrast in permeability and its effects on ground water contrast in stiffness (stiff, dense material over plastic material)
2. GEOMORPHOLOGICAL PROCESSES
(1) Tectonic uplift
(2) Volcanic uplift
(3) Glacial rebound
(4) Fluvial erosion of the slope toe
(5) Wave erosion of the slope toe
(6) Glacial erosion of the slope toe
(7) Erosion of the lateral margins
(8) Subterranean erosion (solution, piping)
(9) Deposition loading of the slope or its crest
(10) Vegetation removal (by erosion, forest fire, drought)
3. PHYSICAL PROCESSES
(1) Intense, short period rainfall
(2) Rapid melt of deep snow
(3) Prolonged high precipitation
(4) Rapid drawdown following floods, high tides or breaching of natural dams
(5) Earthquake
(6) Volcanic eruption
(7) Breaching of crater lakes
(8) Thawing of permafrost
(9) Freeze and thaw weathering
(10) Shrink and swell weathering of expansive soils
4. MAN-MADE PROCESSES
(1) Excavation of the slope or its toe
(2) Loading of the slope or its crest
(3) Drawdown (of reservoirs)
(4) Irrigation
(5) Defective maintenance of drainage systems
(6) Water leakage from services (water supplies, sewers, stormwater drains)
(7) Vegetation removal (deforestation)
(8) Mining and quarrying (open pits or underground galleries)
(9) Creation of dumps of very loose waste
(10) Artificial vibration (including traffic, pile driving, heavy machinery)

Careful local observations over time of water wells or damage from earthquakes may be acceptable substitutes. Variations in mechanical properties with distance from the surface may, in some circumstances, indicate changes of these properties with time.

Man-made processes can be documented by site observations and from construction or excavation records at the site. Separate identification of artificial and natural landslides is useful for both administrative and theoretical reasons.

2.3 Hazard mitigation

Landslide activity, regardless of slope movements' different configurations, materials involved and arisen phenomena, can defined by the following four possible different stages (Leroueil, 1996):

1. Pre-failure stage, when the soil mass is still continuous. This stage is mostly controlled by progressive failure and creep;
2. Onset of failure characterized by the formation of a continuous shear surface through the entire soil or rock mass;
3. Post-failure stage which includes movement of the soil or rock mass involved in the landslide, from just after failure until it essentially stops;
4. Reactivation stage when the soil or rock mass slides along one or several pre-existing shear surfaces. This reactivation can be occasional or continuous with seasonal variations of the rate of movement.

Hazard is the probability that a phenomenon such as a first-time slope failure or an active landslide reaching a given rate of movement occurs. In the failure stage, hazard is directly related to the probability that the triggering factor reaches a critical value leading to failure. For the pre-failure and reactivation stages, hazard associated with a rate of movement is related to the probability that the aggravating factor reaches a given value leading to such rate. For the post-failure stage, the hazard associated with a given rate of movement is very much governed by the materials involved and the predisposing factors, and thus it is more difficult to be defined.

When dealing with a slope of precarious stability and/or presenting a risk which is considered too high, there are three main options:

1. Do nothing to the slope and possibly reduce its possible consequences;
2. Do nothing but install a warning system in order to insure or improve the safety of people;
3. Improve the safety of the slope to a satisfactory level in order to reduce the risk to an acceptable level.

When the size of the moving or potentially moving mass is too large or when the cost associated to mitigation is too high, the possibility to relocate the structure elsewhere should be examined. Obviously, it is preferable to consider such a possibility during the planning stage.

It is worth noting that warning systems do not modify the hazard but contribute to reduce the consequences of the landslide and thus the risk, in particular the risk associated with the loss of lives. Many types of warning systems have been proposed and the selection of the appropriate one should take into account the stage of landslide activity:

1. At pre-failure stage, the warning system can be applied either to identify revealing factors or aggravating factors. Useful revealing factors are, for example, the opening of fissures or the movement of given points on the slope; in such cases, the warning criterion will be the magnitude or rate of movement. When the warning system is associated with triggering or aggravating factors, the first step is to define the relation between the magnitude of the controlling factors and the stability condition or the rate of movement of the slope. The warning criterion can be a given pore water pressure, a given stage of erosion, a minimum negative pore pressure in a loess deposit, etc. It can be also based on rainfall; for example, the hourly rainfall and the cumulative rainfall during a two-day period have been combined in an alarm criterion.
2. At failure stage, the warning system can only be linked to revealing factors, generally a sudden acceleration of movements or the disappearance of a target.
3. At post-failure stage, the warning system has to be associated with the expected consequences of the movement. It is generally associated with the rate of movement and run out distance.
4. Inform the public or the users of facilities about the dangers.

In this perspective, monitoring of landslides plays an increasingly important role in the context of living and coping with these natural hazards. The classical methods of land surveys, inclinometers, extensometers and piezometers are still the most appropriate ones. But the development of methods based on remote sensing and remote access techniques should be of primary interest.

DOE (1994) identifies the following categories of monitoring designed for slightly differing purposes but generally involving similar techniques:

(1) Preliminary monitoring involves provision of data on pre-existing landslides so that the dangers can be assessed and remedial measures properly designed or the site abandoned.

(2) Precautionary monitoring is carried out during construction in order to ensure safety and to facilitate redesign if necessary.

(3) Post-construction monitoring in order to check on the performance of stabilization measures and to focus attention on problems that require remedial measures.

Monitoring techniques will analysed in the next chapter.

2.4 Landslides in structurally complex formations in Southern Italian Appennine

The Southern Apennine chain represents an African-verging fold and thrust belt build on during the Neogene tectogenesis. Starting in the middle Miocene and extending to the upper Pliocene, several compressional tectonic phases (Patacca et al., 1990), associated with the collision between Africa and Europe, caused progressive thrusting and piling of different tectonic units corresponding to different paleogeographic domains, toward stable external domains of the Apulo-Adriatic foreland. Deformation front direction was NW-SE and migrated toward NE. During the Quaternary, the Southern Apennines were affected by an important extensional tectonic phase, with a NE-SW extensional trend which caused further chain fragmenting into several isolated blocks. In the same period, counter-Apenninic regional transcurrent faults were generated.

The geological, geotechnical and geomorphological characteristics of the Southern Appennine represent the basis of rather frequent mass movements. Their magnitude appears to be variable and as such they variably involve man-made structures and activities; relevant events can dramatically affect a given area in terms of economic and social development and of territory planning and utilization. They may actually cause destruction of villages, upsetting of the drainage network and damages to large public works (motorways, aqueducts, dams, etc.), thus posing complex and expensive problems of prevention and correction which are in some cases beyond man's control.

The geological and geotechnical aspects and the mechanism of the landslides of Southern Italy are varied and extremely complex and have been analyzed in several studies of general character (Almagià 1910, Cotecchia 1971, Guida and Iaccarino, 1991, Di Maio et al., 2010).

The stability conditions principally depend upon present morphological, geological, geotechnical features which, in turn, depend upon the genesis and constitution of the involved materials and upon the succession of the events modeling landforms. This is particularly true for slopes occurring in formations that have been referred to as structurally complex formations (Fig. 2.4.1) (ESU, 1977).

These formations (Esu, 1977) can be distinguished in three main groups (A, B and C): the first one is constituted by fine materials, lithologically homogeneous, with presence of structural discontinuities, while the second one by heterogeneous material, like flysch, characterized by the presence of two kind of soils with different mechanical characteristics and the last one constituted by heterogeneous material like rock or less weathered rocks in a clayey matrix.

Further, depending on the geologic structure, the A and B types can be subdivided in: a1) fissured and/or fractured clays (or argillites), and a2) scaly clays (or argillites); b1) regular alternance of rock and fissured and/or fractured clays (or argillites), b2) chaotic setting of rock

strata and highly fissured/fractured or scaly clays (or argillites), and, eventually, b3) scaly clays (or argillites) produced as effect of tectonics, which include rocks.

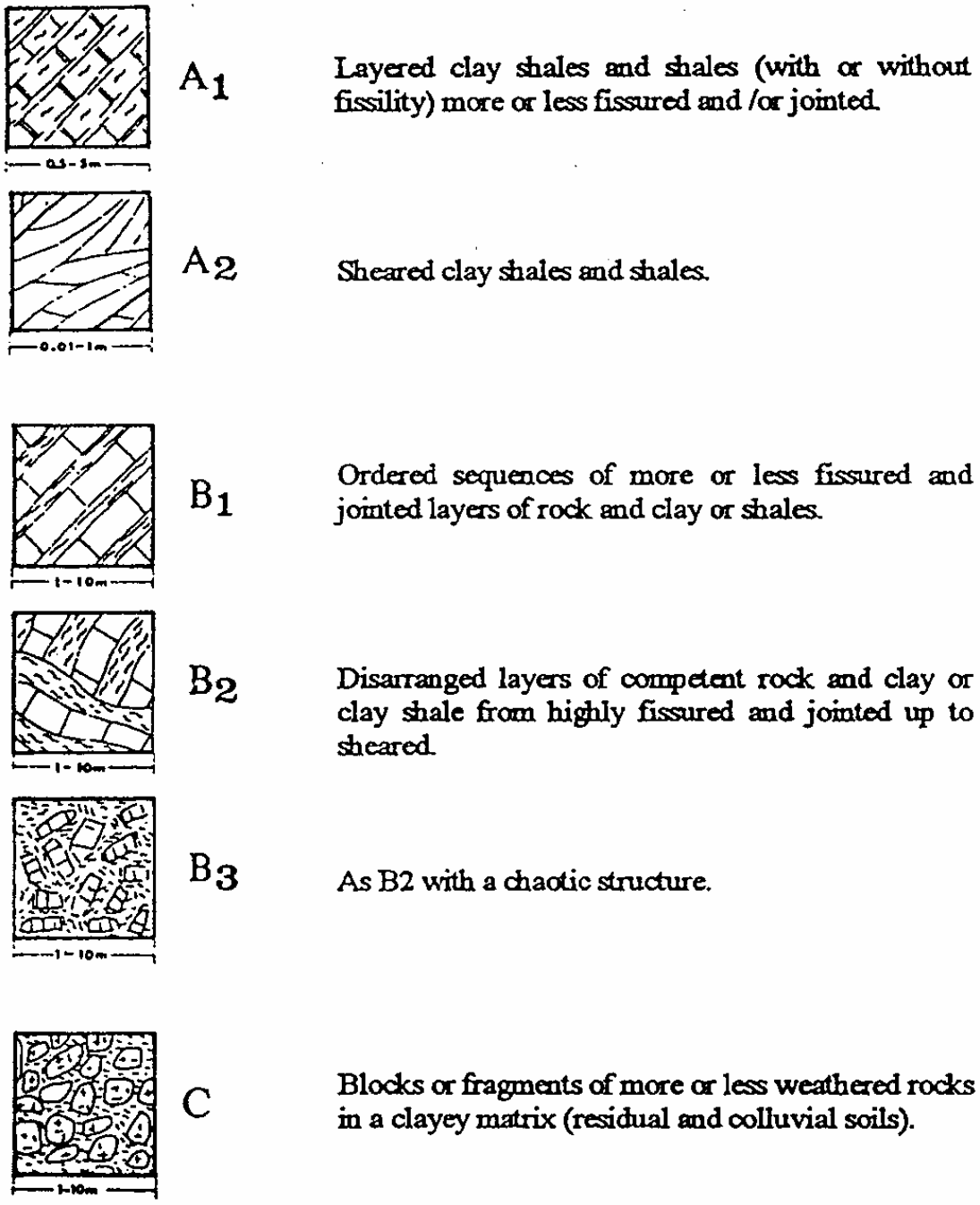

Figure 2.4.1. Types of Structural complexities (after Esu, 1977)

All sites are characterized by the outcropping of structurally complex formations, that, like noted above, have a key-role in the control of the mechanical and hydrological behaviour of the slopes. Such materials are affected by many mass movements because of their poor mechanical properties, due to the weathering of the shallow layers,

A picture of the magnitude and number of landslides in the Southern Italy is given in Fig. 2.4.2 which shows the landslide index obtained from IFFI Project. The IFFI project (Italian Landslide Inventory - 2008) was carried out by the Geological Survey of Italy in ISPRA (National Institute for Environmental Protection and Research) in cooperation with the Italian Regions and Indipendent Provinces. More than 480.000 events have been inventoried in this project which represents the first updated and homogeneous inventory map on the entire national territory.

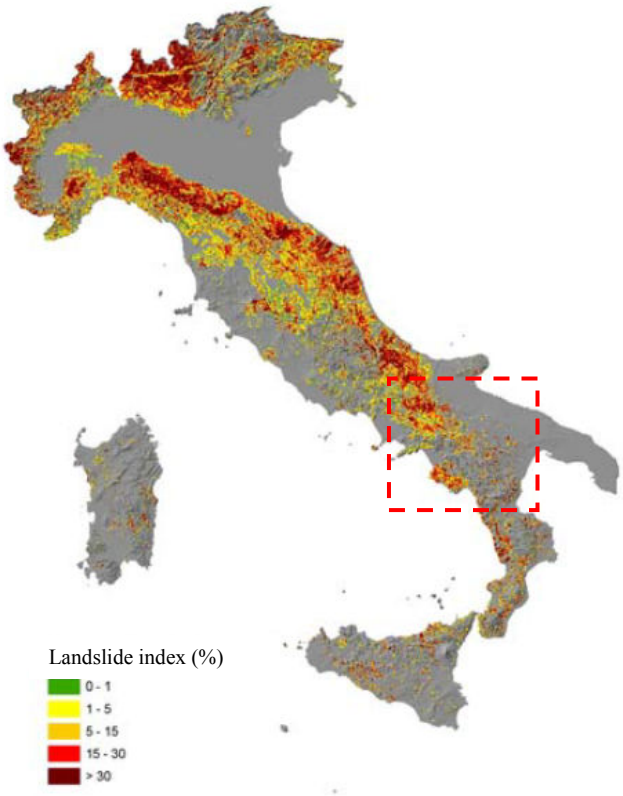

Figure 2.4.2. Landslide index (%): area affected by landslide/total area; the area of interest is in red dashed line.

The main aims of IFFI Project were to give a complete and updated overview of landslide phenomena in the Italian territory, by collecting data obtained from different institutions (River Basin Authorities, Regions, Independent Provinces and Municipalities) and to put up a cognitive tool in order to assess landslide hazard, for the environmental protection and land use planning on national and local scale.

Figure 2.4.3 represents a sketch of Landslide Inventory Map where the detected landslides, by means of points shape (PIFF), are showed. The area of interest is composed by three administrative Italian Regions (Basilicata, Campania and Molise) where a part of the relieves of the Southern Appennine chain are present and in which the studied sites are located. As shown in Figure 2.4.4 the number of landslides is very high. Approximately 56000 landslides have been inventoried, representing about the 12% of the identified phenomena on the entire Italian Nation.

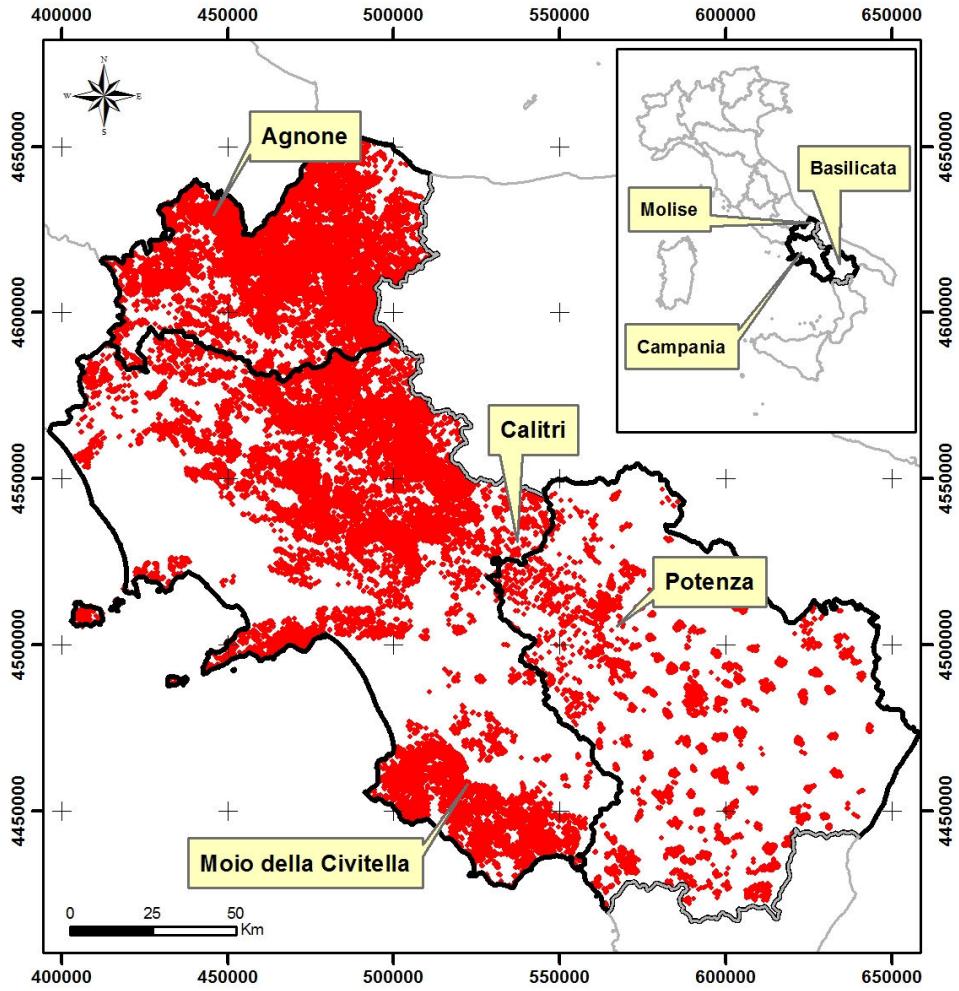

Figure 2.4.3. Sketch of Landslide Inventory Map for the area of interest.

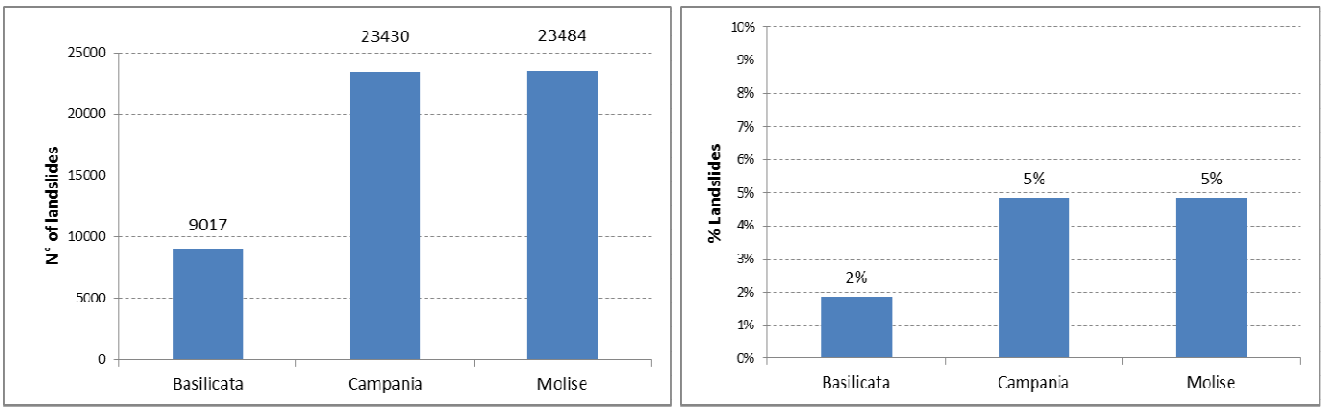

Figure 2.4.4. Number and percentage of landslides in the area of interest.

In detail, in Agnone, Calitri, Moio della Civitella and Potenza municipalities 529, 72, 83 and 129 landslides have been identified, respectively (Figures 2.4.5, 2.4.6, 2.4.7, and 2.4.8). Landslide density (number of landslide/Km^2) varies between 0,7 for Calitri and Potenza sites to higher values, about 5, in Agnone and Moio della Civitella municipalities.

Landslides involve structurally complex formations, largely outcropping in the area of interest. The phenomena are generally slow-moving or intermittent landslides, with a complex style of activity (Cruden & Varnes 1996). As shown in Figure 2.4.9 slides, earth flows and slides evolving into earthflows (complex phenomena) are the most common typologies, characterized by slow or extremely slow velocity (Cruden e Varnes, 1996).

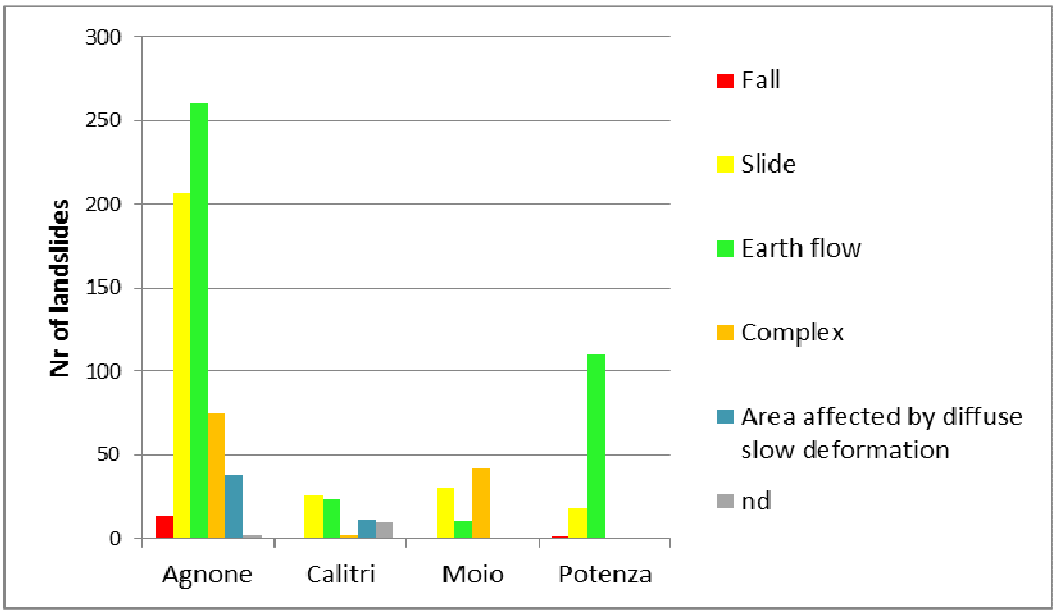

Figure 2.4.9. Distribution of inventoried landslides with relation to typology

It is worth pointing out that in the last years (2010-2013) the River Basin Authorities, which are the reference territorial entities in charge of land planning and management in terms of landslide risk assessment, are working to revise the Landslide Inventory Maps, each for their respective territorial area. Such update involved, in some instances, the growth of the inventoried landslides. The case of the Basin's Authority of Sele River whose territory falls in both Campania and Basilicata regions is emblematic. The Landslide Inventory Map update identified approximately 10000 more phenomena (Fig. 2.4.10). Such increase can be explained on one hand by the natural evolution of the slope, and on the other by the detection method used. More detailed survey scales, in situ studies, photointerpretation of higher resolution aerial photographs and the availability of updated maps allowed to identify otherwise unknown phenomena. Finally, a relevant contribution to landslide

identification was made by new techniques of Remote Sensing, which will be further analyzed in the following chapters. Such techniques, together with traditional methods, were used to obtain a comparable accuracy of ground surface displacements, being less expensive and time consuming.

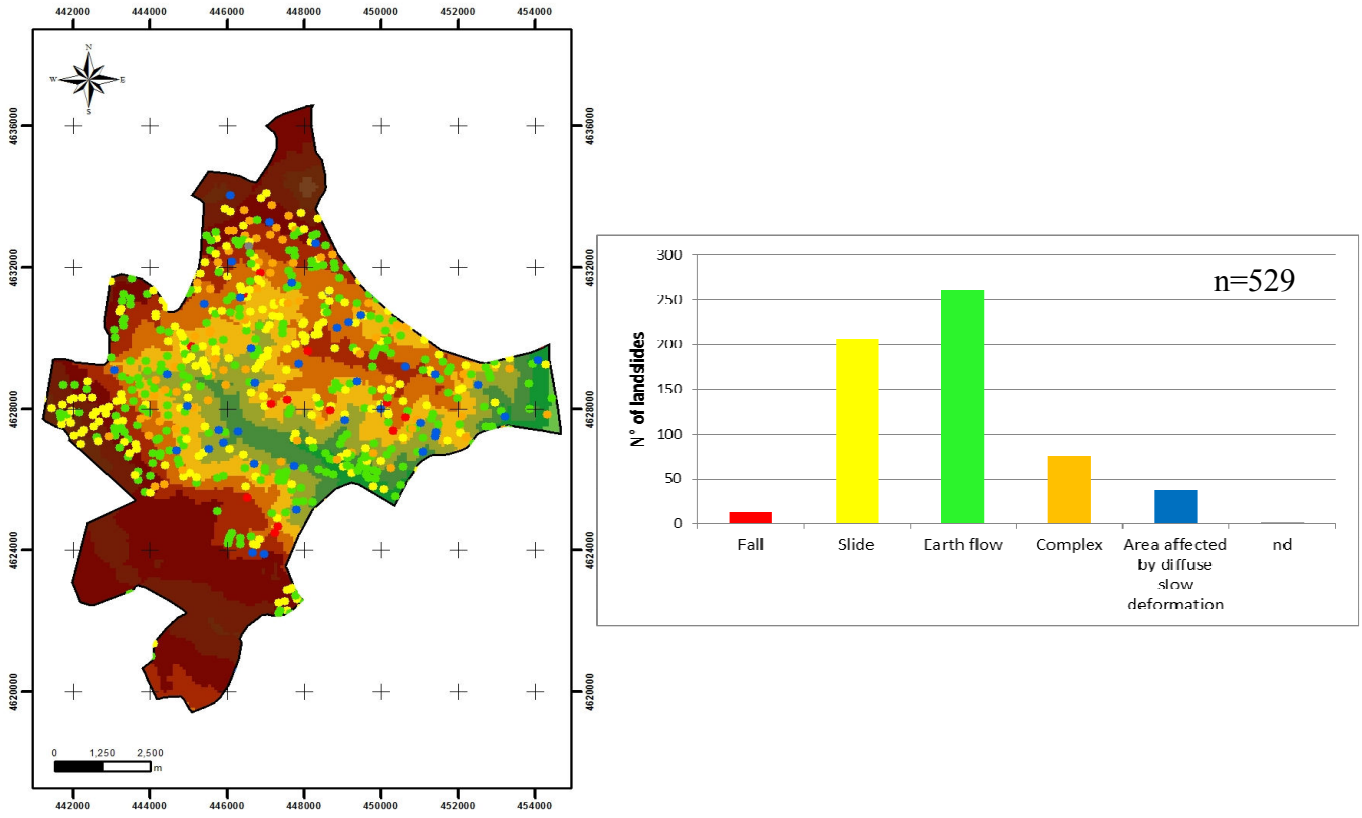

Figure 2.4.5. Distribution of inventoried landslides with relation to typology for Agnone site.

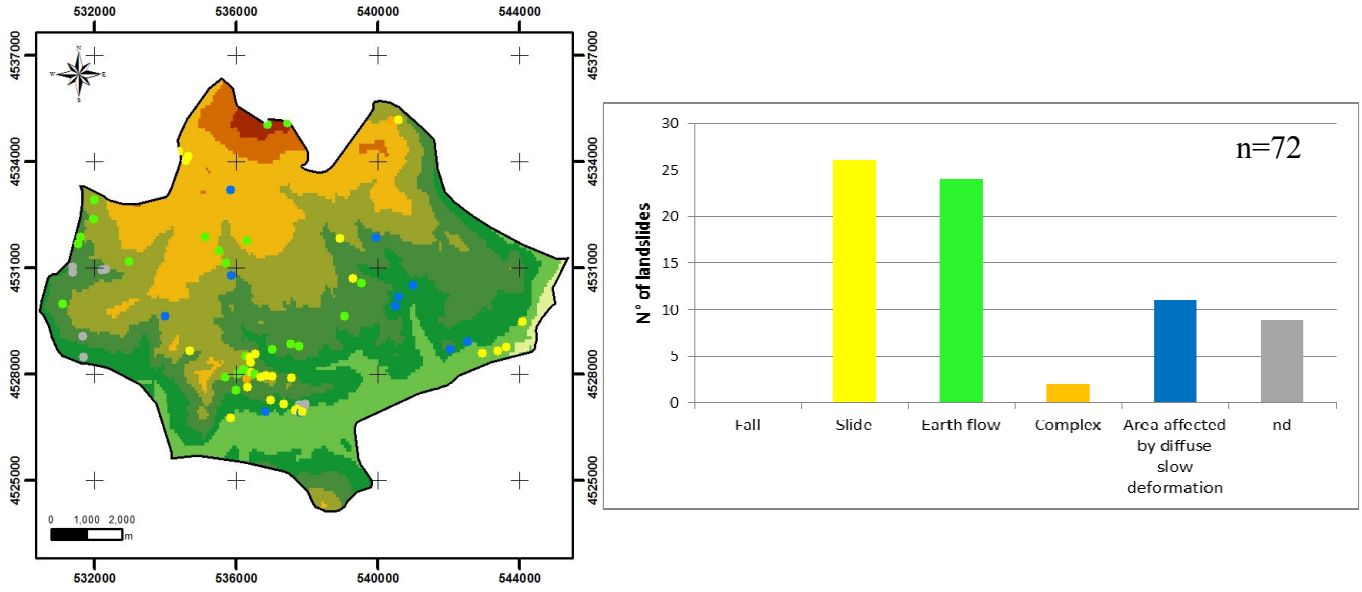

Figure 2.4.6. Distribution of inventoried landslides with relation to typology for Calitri site.

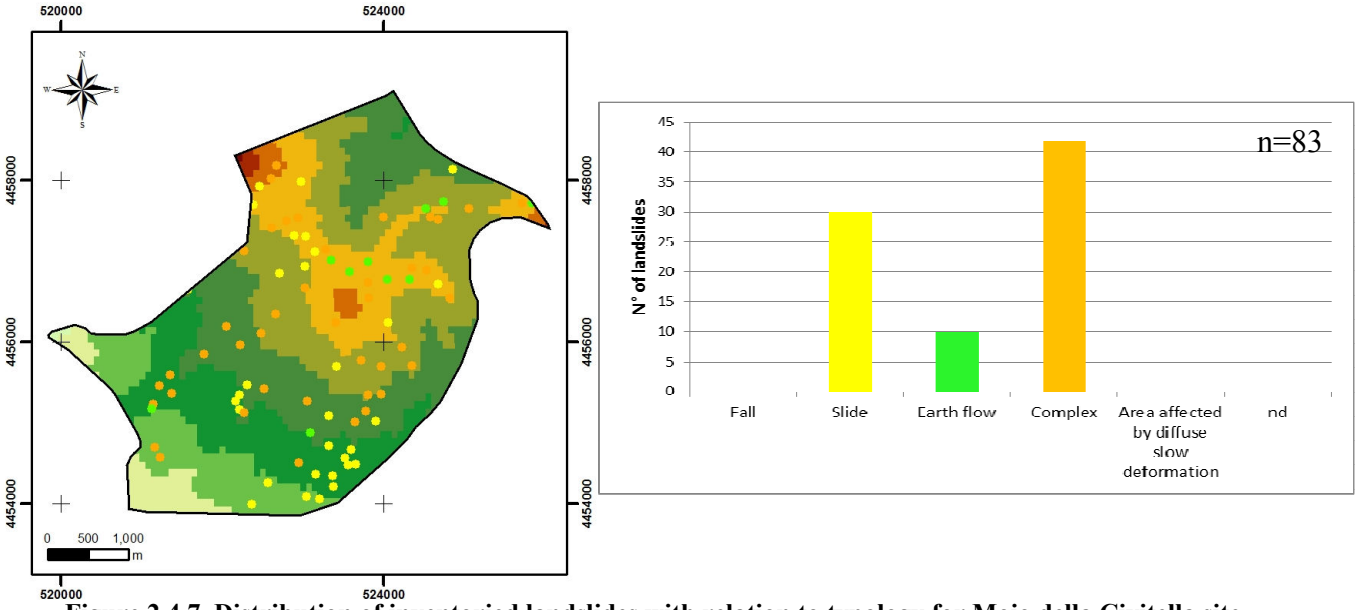

Figure 2.4.7. Distribution of inventoried landslides with relation to typology for Moio della Civitella site

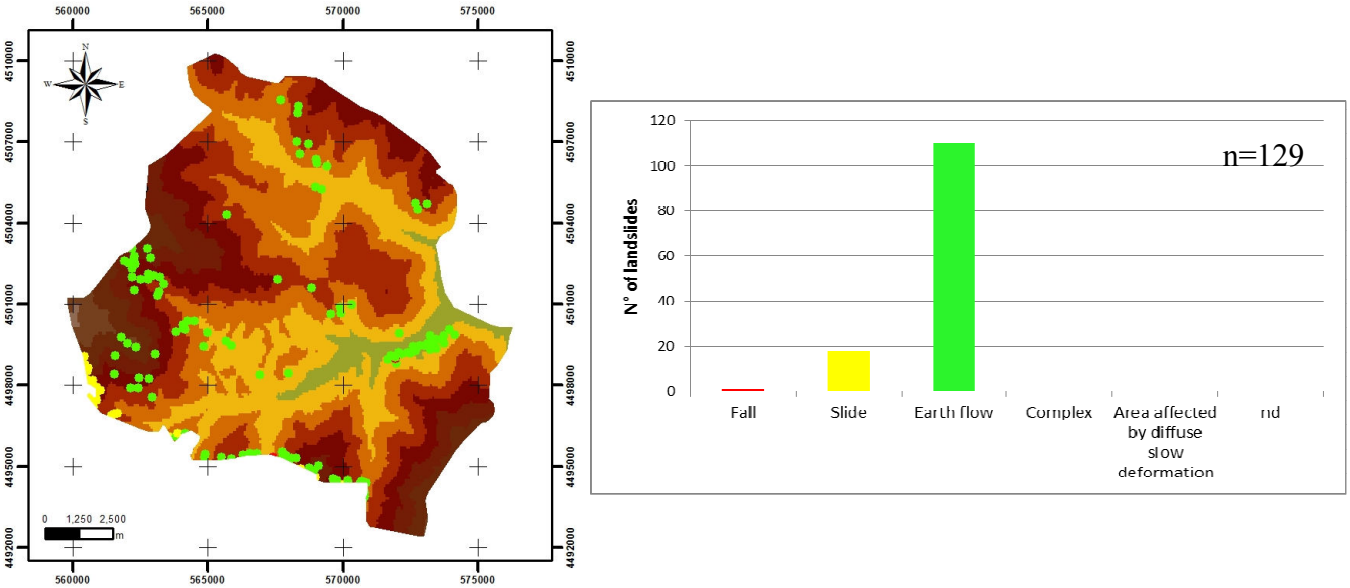

Figure 2.4.8. Distribution of inventoried landslides with relation to typology for Potenza site.

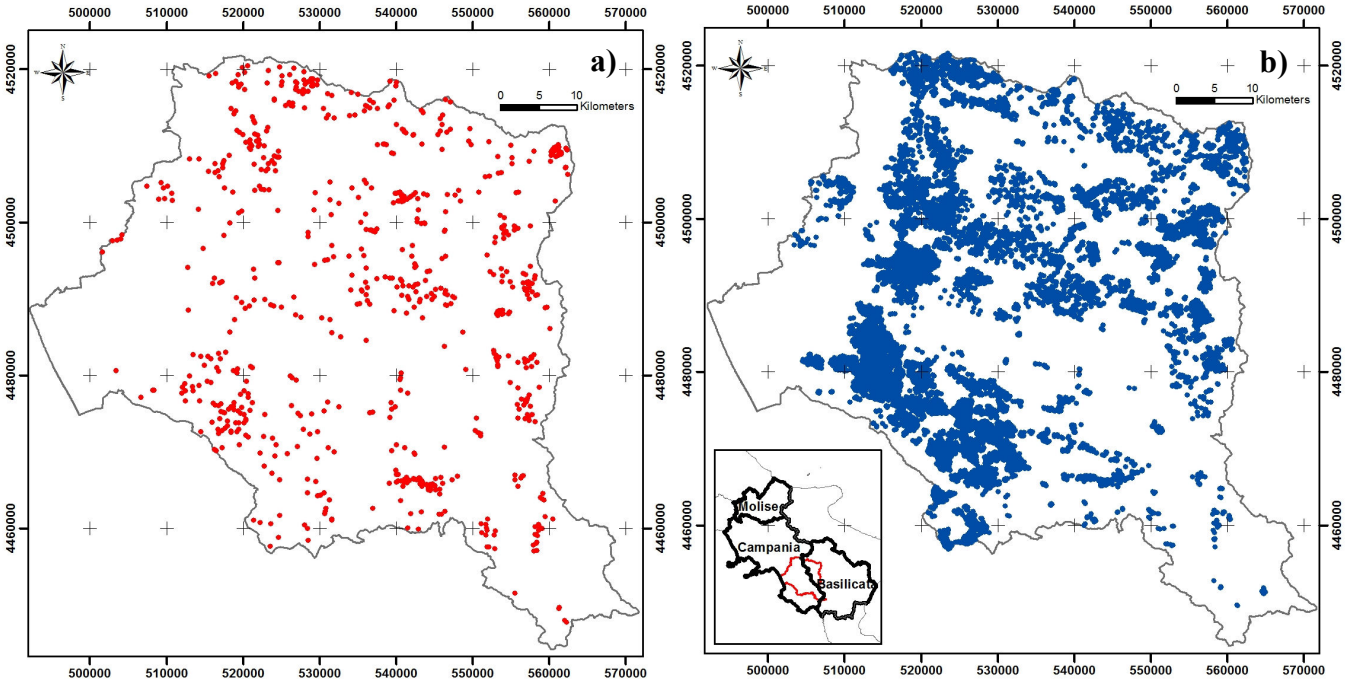

Figure 2.4.10. Comparison between Landslide Inventory map for Basin's Authorities of Sele River: a) 2002, b) 2012.

CHAPTER 3

3 Monitoring

The term “monitoring” refers to control processes, which may display different degrees of complexity, of a given phenomenon or activity.

Knowledge of the environmental components and of the dynamics that rule phenomena evolution is crucial to territory management. For this reason, territory monitoring plays a key-role in the analysis of events which may produce catastrophic effects on the community.

This chapter describes the steps needed to build an effective monitoring system. Ideally, the best monitoring system for a given phenomenon is identified on the basis of the answers to the following questions:

- What has to be monitored?
- Which is the magnitude of the event?
- How to monitor?
- Which scale has to be used?
- What is the monitoring frequency?
- How long does the monitoring campaign have to last?
- What are the costs?
- What are the expected results and advantages?

The working phases can be outlined as follows:

a) Phenomenon description
b) Action planning
c) Monitoring network development

The first phase (phenomenon description) is carried out by archive research of thematic maps, aerial photographs, photographic documentation, historical data, cause and type of event, previous studies, etc.).

In action planning the results obtained in the first phase are critically evaluated, initial on site surveys are carried out, as well as a functional in-depth analysis of the monitoring planning. The final result of this phase is the identification of possible preliminar investigations or peculiar

measures to perform before developing the monitoring network. In this phase some kind of monitoring (i.e. of superficial movements) is frequently activated in order to better understand the real activity of the phenomena and its extension. This allows to determine the extent of possible additional surveys and investigations.

The monitoring network development entails the installation and maintenance of a true monitoring network. To do so, it is required to carry out the investigations (preliminary, deepened), specified in the previous phases. They essentially consist in direct surveys and geological and geotechnical investigations, whose results allow to define:

- Which are the parameters to measure;
- Where and how to measure them.

3.1 Landslide monitoring

Monitoring applied to the phenomena of slope instability corresponds to a source of measures that enable to understand the extension, the magnitude and thus to estimate the associated hazard. More generally, the understanding of the phenomenon must provide for the acquisition of information on:

• the system of sub-superficial displacements, in terms of direction, modulus, and rate of velocity;

• the scheme of deep displacements, with definition of the position of the sliding surface;

• the aquifer system regimen;

• the rainfall regimen;

For each of the above-mentioned items there are several techniques and different types of instruments, which over time have become increasingly sophisticated and refined. In particular, the development of electronics and sensors gave a remarkable acceleration in the evolution of devices, which nowadays have reached accuracy and response times inconceivable a decade ago.

Regarding sub-superficial movements monitoring, various techniques have been developed, which can be synthetically divided into:

- Photogrammetry/Photointerpretation;
- Ground-based and satellite geodetic techniques;
- Geotechnical;
- Remote sensing.

Considering the peculiarities of each of these techniques, it is often desirable to proceed to their simultaneous use, in order to obtain the same information that will be subsequently merged for

a better and more objective interpretation of the data. For this purpose, it is necessary to know the potentials and limitations of each of them.

3.1.1 Photogrammetry/Photointerpretation

Photogrammetric techniques have been extensively used in ground movements studies (Maria et al. 2004; Mills et al. 2005; Hu et al. 2008; Liu and Wang 2008; Smith et al. 2009). The main advantages of using photogrammetry are the reduced time of fieldwork, simultaneous three-dimensional coordinates, and, in theory, an unlimited number of points that can be monitored. The accuracy of photogrammetric point position determination has been much improved in last years, making it attractive for high accuracy deformation measurements.

The interpretation of aerial photographs has proven to be an effective technique for the recognition and delineation of landslides (Soeters and Van Westen 1996). It is an effective technique for recognizing and delineating the three-dimensional overview of the terrain from which the interrelations of photography, drainage, surface cover, geology materials, and human activities on the landscape can be viewed and evaluated.

An overall perspective of a large area and boundaries of existing slides can readily be delineated on aerial photographs. Surface and near-surface drainage channels can be traced. Important relations in drainage, topography and other natural and man-made elements that seldom are correlated properly on the ground become obvious on photographs. Furthermore, soil and rock formations can be seen and evaluated in their undisturbed state. Recent photographs can be compared with old ones to examine the progressive development of slides (Fig. 3.1.1.1) and aerial

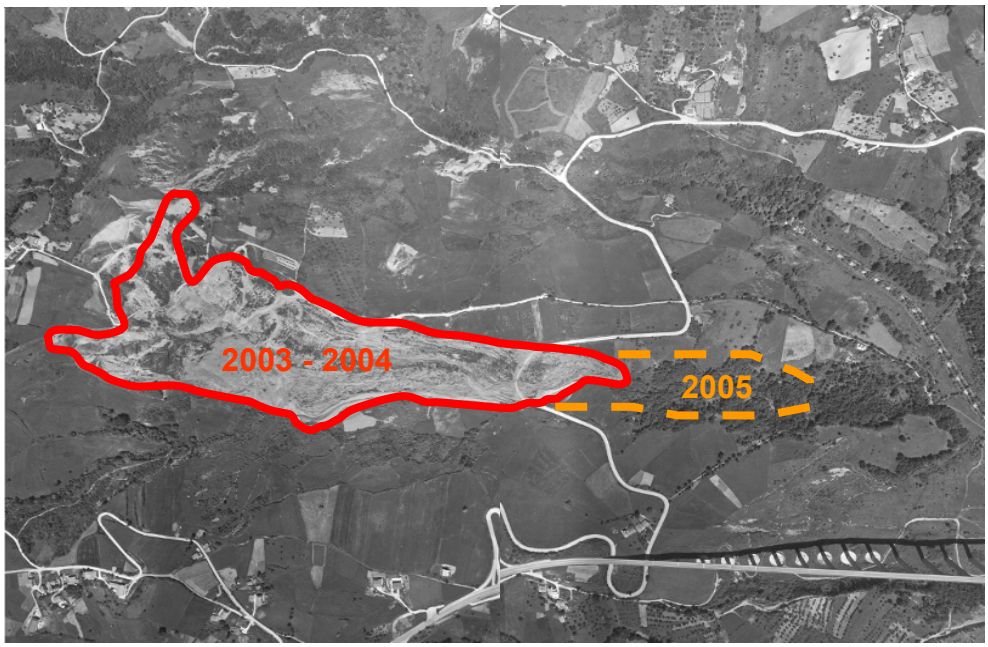

Figure 3.1.1.1: Example of progressive development of a slide by aerial photographs studied.

photographs can be studied at any time, in any place and by any person. Terrestrial photogrammetry and ground-based photography are also being used for local-scale landslide monitoring.

Sites that are too steep or too small to be confidently viewed from the air are fit for ground studies, albeit at distance. Terrestrial photogrammetry can effectively be used for unsafe or inaccessible sites, as road cuttings and landslides.

3.1.2 Ground-based and satellite geodetic techniques

They allow to evaluate the absolute position of the investigated points. In some cases the geodetics sensors can be used for the evaluation of control points by repeated measurements. In others, continuous measurements can be obtained by using automated instruments. In both cases, the objective is to obtain the coordinates (position and height) of control points within areas affected by deformation phenomena. From the comparison of the calculated position in the various readings and throughout statistical evaluations on the reliability of the data, the actual displacement vectors can be traced back, as shown in the Figure 3.1.2.1.

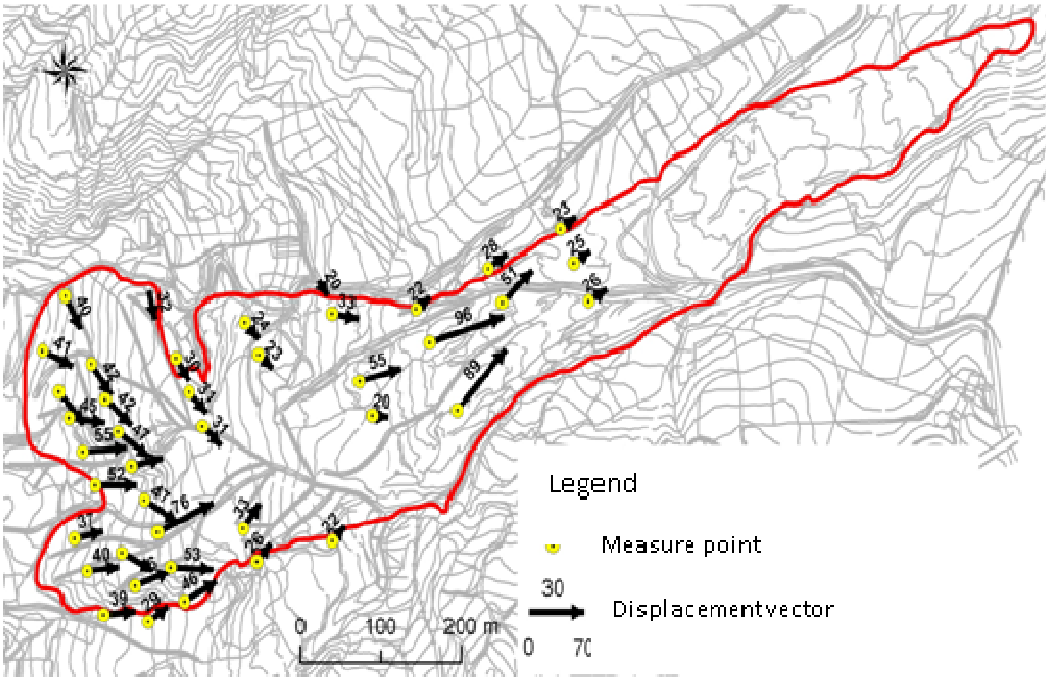

Figure 3.1.2.1: Example of topographic network measurements.

An example of terrestrial geodetic sensor, used for the monitoring of landslide phenomena (Reyes and Fernandez 1996; Walstra et al. 2004; Wasowski et al. 2004; Burghaus et al. 2009) is the total station (Fig. 3.1.2.2a). The latter allows to assess the three positioning parameters, distance,

vertical angle and horizontal direction simultaneously, making it is possible to obtain the absolute position of the monitored points.

Points identification is usually carried out by using targets (denominated prisms), located on specific pillars (Fig. 3.1.2.2b), which allow to detect the position in a very short time. Also in this case, it is possible to identify advantages and constraints of this technique. The main advantage of this instrumentation is the capability to detect the three-dimensional coordinates of the monitored points, thus allowing to reconstruct the real displacement vector. The main constraint is that monitored points are only the ones which are actually visible by the instrumentation.

Figure 3.1.2.2: a) left, the total station , b) right, the topographic stake with prism

As for terrestrial systems, satellite instrumentation, referred to as the Global Positioning System (GPS) (Fig. 3.1.2.3), allows the assessment of the position of points affected by movement by obtaining their three-dimensional coordinates (Bonnard et al 1996; Wasowsky et al.2004; Mills et al.2005; Webster and Dias 2006, Yin et al., 2008; Zhang et al., 2008). The current GPS systems allow to perform both occasional measures, repeated over time, and real-time measurements thus allowing studies in small and large scale. The main advantages, with respect to the terrestrial instrumentation, are the possibility to work in any condition of visibility and weather. It is nevertheless required a certain satellite "visibility" from the monitored points. Several experiments conducted in the field of monitoring of surface deformation estimated an error of about ± 5 mm for ranges of 50 km in diameter in the absolute positioning of the point.

While, as far as the evaluation of displacements is concerned, they are characterized by a standard deviation of about 3 mm for the horizontal component and 1.5 times the horizontal to the vertical.

Figure 3.1.2.3: GPS sensor.

3.1.3 Geotechnical monitoring

This term is commonly used to indicate the set of measures aimed at controlling the behavior of "geotechnical systems". In the study of the behavior of landslides slopes such measures include, among others, the evaluation of surface deformations, with the techniques set out above. In particular, we can measure displacements, absolute or relative, evaluate the deformations among different sectors of the mass in motion and, thus, correlate them to its geometry and to the type of movement expected or observed. It is also possible to collect information and perform measurements.

It can also measure the stress state and the presence or absence of water. Among the main instruments for geotechnical monitoring inclinometers, extensometers and piezometers should be mentioned. It must be pointed out that, in addition to these instruments, weather stations are of fundamental importance. They measure parameters such as rain, humidity, snow, wind, etc.. for the study of landslides phenomena.

3.1.3.1 Inclinometers

In many cases inclinometers are used to determine subsurface movement of landslides (Borgatti et al., 2006; Bonnard et al., 2008; Bressani et al., 2008; Jongmanset al., 2008; Mihalinec

and Ortolan 2008, Yin et al., 2008). They are installed in boreholes located within the landslide (Fig. 3.1.3.1.1).

Inclinometers allow to evaluate the depth of the sliding surfaces, by measuring at the same time the direction of displacement (azimuth) and its vertical component. The accuracy of the measurement is of the order of ± 0.02 mm for every 3 m of depth. The major limitation lies in the fact that for the shape of the instrumentation it is possible to estimate the displacements only in 2D without obtaining three-dimensional repositioning.

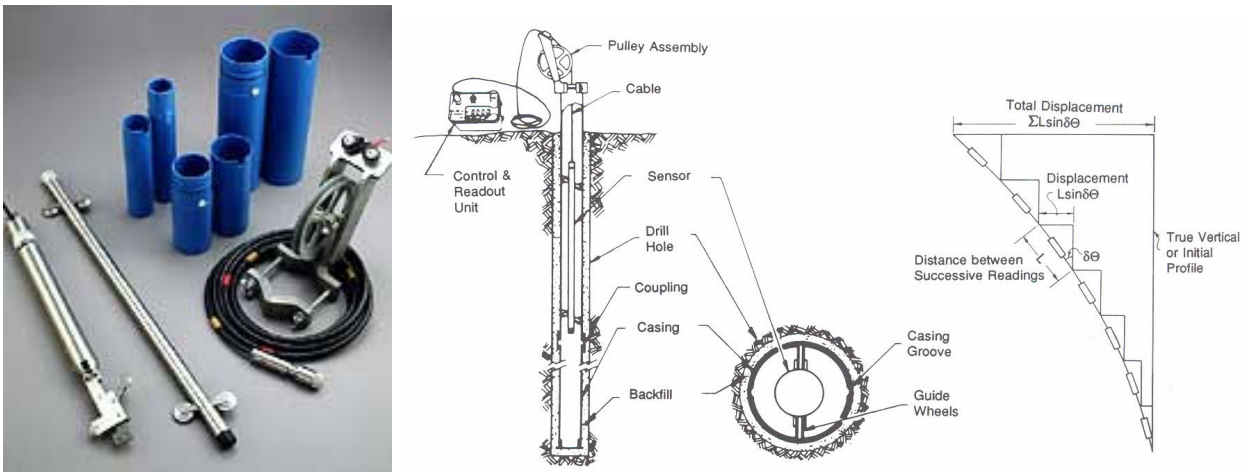

Figure 3.1.3.1.1: scheme of inclinometer installation.

3.1.3.2 Extensometers

They enable the measurement of axial deformation with respect to reference points placed along the same axis. Even in this case they can be installed inside boreholes. The most widespread extensometers are characterized by accuracies of the order of ± 0.3 mm for every 30 m. The main factors influencing the measurement gauge are the temperature and the correct installation of the equipment. Further limitation lies in the fact that the measurement is one-dimensional, so only useful in case the direction of the displacement vector is already known.

One of the main causes triggering landslides phenomena is the change in groundwater level due, in some cases, to high intensity rainfall events that results in the reduction of the resistance of the materials involved in the event. For this reason, piezometers are the most widely used instruments in deformation monitoring; since they measure the change in groundwater level over time (Fig. 3.1.3.2.1), they allow, throughout a careful reading, a first interpretation of the possible causes of triggering event.

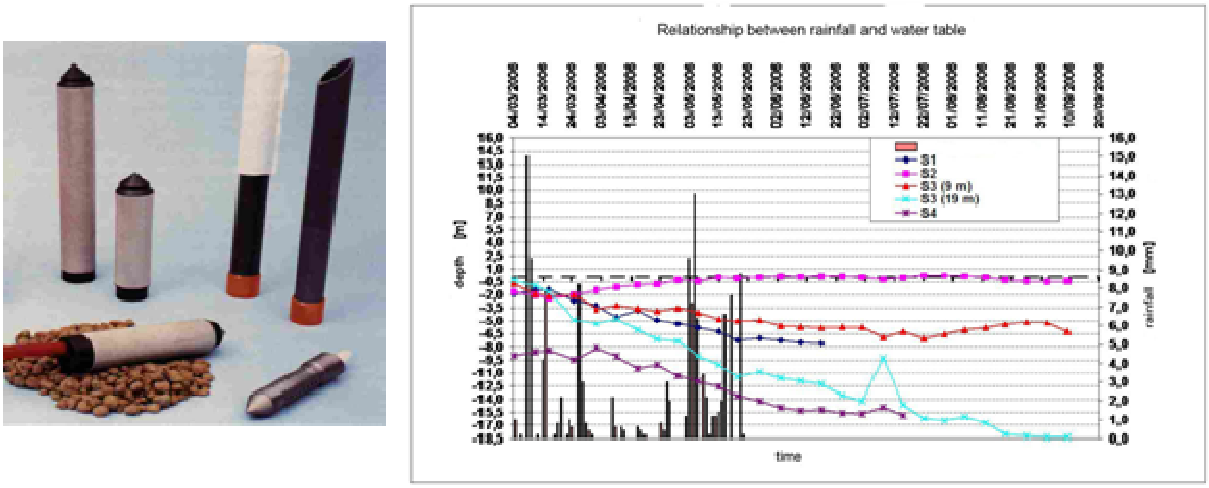

Figure 3.1.3.2.1: Piezometer and graphs of piezometric readings.

They are placed inside conveniently instrumented boreholes. The different types of piezometers (vibrating string, tires, Casagrande, open pipe) are used according to the filtration speed of the water inside the soil, which in turn affects the accuracy and response times of the piezometric measurements.

3.1.4 Remote sensing

This term refers to all the techniques that allow to investigate a phenomenon by means of sensors that work at different wavelengths (Fig. 3.1.4.1) placed at a considerable distance from the studied object.

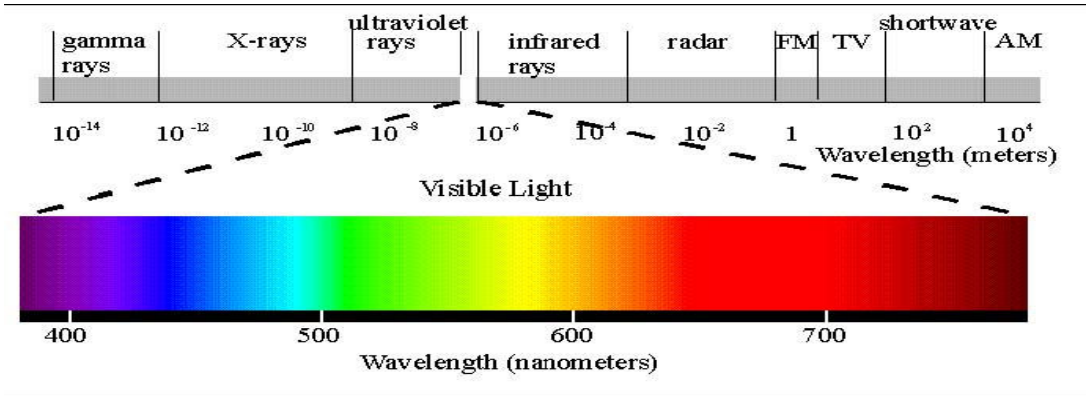

Figure 3.1.4.1: Electromagnetic spectrum

This is done by sensing and recording reflected or emitted energy and processing, analyzing and applying this information. The distance of the observer from the collected information can range from a few meters (Proximal Sensing) to thousands of kilometers (Remote Sensing).

As far as the application of this technique to the monitoring of landslides phenomena is concerned, two approaches can be identified, depending on the source of the electromagnetic

energy: a qualitative one, which only allows to classify the phenomenon (type, extension, etc..) and works primarily with optical data at wavelengths ranging from the visible to the infrared by means of passive sensors which measure the energy reflected when the illumination source is external. The second approach uses active sensors, which illuminate the scene and measure the backscattered signal, at L, C or X-bands, obtaining quantitative information, such as the magnitude (volume and velocity) of the event, such as the case of SAR sensors. Thanks to these sensors, Advanced Differential Interferometry techniques like PSInSAR (Ferretti et al., 2001), SBAS (Berardino et al., 2002), SPN (Arnaud et al., 2003), CPT (Mora et al., 2003), IPTA (Duro et al., 2005), PSP-IFSAR (Constantini et al., 2008), SqueeSAR (Prati et al., 2010) have been implemented. In the last two decades they have achieved encouraging results in various fields of application (glaciers (Goldstein et al., 1993), volcanoes (Massonnet et al., 1995), earthquakes (Massonnet et al., 1993), subsidence phenomena (Cascini et al., 2009), monitoring of infrastructures (Rising et al., 2012) and, in particular, landslides phenomena monitoring (Ferretti et al., 2005; Meisina et al., 2006; Calcaterra et al., 2008).

Finally, two terrestrial active remote sensing techniques that in recent years have achieved good results must be mentioned. They are the use of the Laser Scanner (Oppikofer et al, 2006; Oppikofer, 2008; Travelletti et al, 2008) and the Ground Based SAR as a tool for monitoring buildings or structures (Tarchi et al. 1997), landslides (Tarchi et al., 2003b, Leva et al. 2003), glaciers (Luzi et al. 2007). The first was especially created for the use in architecture, but it has quickly found wide application in engineering, like the monitoring of structures subjected to stress and strains, such as bridges, towers, dams, galleries, etc.

Recently, thanks to the overall performance improvement, especially in range and accuracy in angular relocation of rotating mirrors, the laser scanner has been used for applications in different fields as in the study of geomorphology (e.g. landslide slopes and caves); examples include the monitoring of mining and evolutionary rock quarries and /or loose material.

The ground based radar with synthetic aperture and interferometric technique (GBInSAR) is an innovative type of remote detection that allows a very accurate measurement of the movement of the ground over large areas. It uses a combination of devices and methods that can generate raster maps of two-dimensional deformations (and/or velocity) of a slope irradiated, from a remote location, with electromagnetic waves covering an area of several square kilometers and obtaining a sub-millimetric precision (equivalent or even better than traditional topographic and geotechnical instrumentation). The output maps are made up by thousands or tens of thousands of pixels, each with its own time series of displacement. Various reasons make GBSAR an attractive device: it provides displacement measurements with sub-millimetric precision on areas large up to a few

square kilometers; it acquires images with "high" frequency; it has a ground resolution of a few meters and it is able to monitor also relatively fast movements. This large amount of information and the spatial distribution of data are typically useful for understanding the phenomena, for real time monitoring, and, finally, for the decision-making process. Periodic monitoring of landslides phenomena with GBInSAR represents a promising approach for the long-term evaluation of instability conditions, especially in those areas where property and infrastructure are exposed to risk.

More information on the monitoring methods can be found in the general reviews (Franklin 1984; Keaton and DeGraff 1996; McGuffey et al. 1996; Mikkelsen 1996; Soeters and Van Westen 1996; Turner and McGuffey 1996; Olalla 2004; Van Westen 2007; Liu and Wang 2008).

Ultimately, in order to obtain the best results from a technical/economic point of view in the phase of which monitoring system has to be installed, it must be taken into account the actual capacity (resolution, precision, error, processing time, etc.) of the individual systems, in order to choose the most suitable technique for the phenomenon to be studied. An example of this preliminary evaluation can be easily done with a scheme like the one shown in the following figure (Fig. 3.1.4.2).

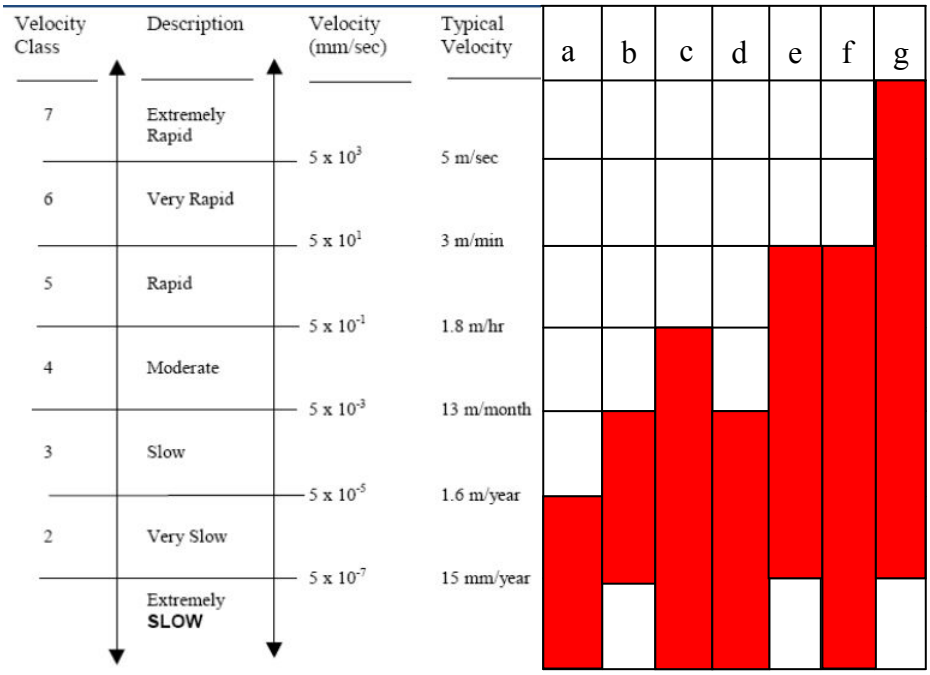

Figure 3.1.4.2: a) PSInSAR; b) Traditional DInSAR; c) GBInSAR; d) Inclinometers; e) GPS; f) Total station; g) Field survey.

CHAPTER 4

4. Radar remote sensing: technique and applications

4.1 Radar

Radar is the acronym for Radio Detection And Ranging. It refers to a technique as well as an instrument. The radar instrument generates electromagnetic waves in the radio wavelengths and detects the echo of these waves from objects. The radar technique uses the two-way travel time of the pulse to determine the range to the detected object and its backscatter intensity to infer physical quantities. Although the technology mainly gained momentum through military applications in those early years, civil and scientific applications arose quickly afterward (Hanssen, 2001). There are some advantages coming from the use of these sensors, such as:

- the opportunity to acquire data whenever you want day and night, and whatever are the weather conditions;

- the full control of the signal features (such as the wavelength, the angle of incidence, the phase).

The microwave beam enlightens the earth surface, called swath, with a certain obliquity compared with the direction of the nadir (Figure 4.1.1). The SAR image will be a projection in the

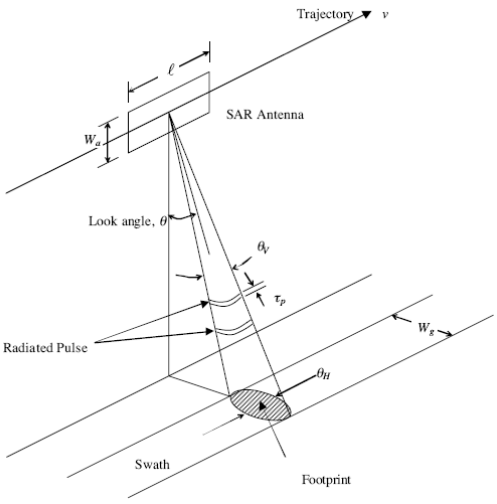

Figure 4.1.1: The imaging radar geometry (Chan and Koo, 2008).

sensor's acquisition plane, slant-range plane, of the targets placed on the Earth surface, the ground-range plane. The direction along the trajectory is called *along-track or azimuth range*, while the perpendicular direction is called *across-track* or *ground range*. Differently from the optical survey instruments which can distinguish among targets according to their angular distance from the nadir of the sensor, a radar can generally distinguish the reflected signals coming from different targets only according to the return time of the signal. That is why the radars use a *side-looking* shape, that is to say, they enlighten just a side of ground range. It is also important to make a distinction between the angle of incidence of the sensor and the angle of local incidence (Figure 4.1.2), that is the one formed of the radar beam and the local normal to the surface which is subject to some changes according to the ground slope. The direction between the antenna and the object along the *Line Of Sight (LOS)* is called *slant range*.

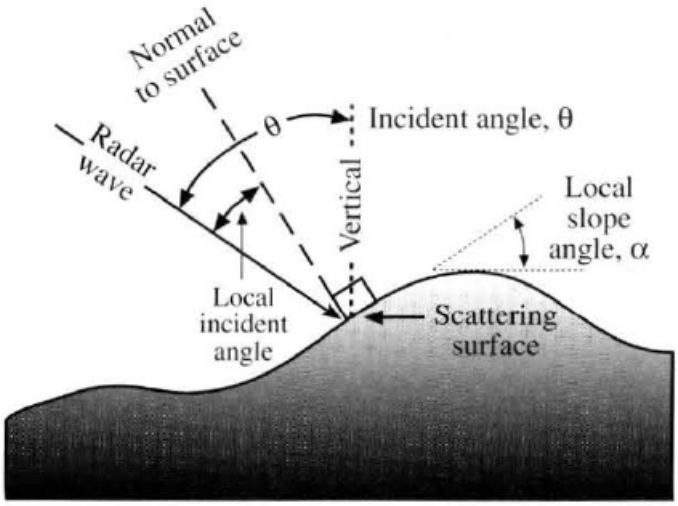

Figure 4.1.2: The relationship between radar incident angle (θ) true vertical, and local slope angle (α) (after Henderson and Lewis, 1998).

This kind of sensor is defined Real Aperture Radar (RAR). Ground resolution is defined as the capability of the sensor to detect two targets on the ground and is given by:

$$\rho_g = \frac{c\lambda}{2\sin\vartheta} \qquad (1)$$

where λ is the wavelength, c is the speed of light and θ is the look angle. The range resolution is function of wave width and look angle but independent of height.

While the azimuth resolution (Fig. 4.1.3) is the minimum distance on the ground in the direction parallel to the flight path of the platform at which two targets can be separately imaged, and is equal to:

$$\rho_a = \frac{R\lambda}{l} \qquad (2)$$

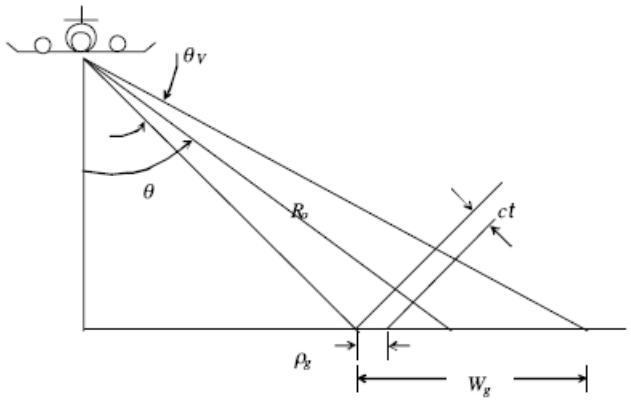

Figure 4.1.3. Range resolution of areal aperture radar (Chan and Koo, 2008).

Through the just said equation we can immediately see how, as for the RAR system the azimuth resolution is highly limited by the antenna length. For example, if we consider the following values:

$\lambda = 3{,}1$ cm

D = 10 m

h = 700 km

$\gamma = 23°$

The dimension of the pixel on earth will be about 3 km along the satellite orbit direction. That is the reason why the RAR system on satellite platform cannot be used in order to assessing the displacements.

4.2 Synthetic Aperture Radar (SAR)

SAR is a technique which uses signal processing to improve the resolution beyond the limitation of physical antenna aperture (Curlander et. al., 1991). In SAR, forward motion of actual antenna is used to 'synthesize' a very long antenna (Fig. 4.2.1) allowing to reach a good resolution with antenna structures of reasonable size.

In an instant t_0 the radar beam starts "enlightnening" a point P. The transmitter sends a series of waves that, from t_0 to an instant t_i, beat P. The real antenna D occupies, then, a series of 2N+1 equispatial positions, and for each of them it will send a pulse to the target. Therefore the real length antenna D defines a synthetic length L_s, along the direction of the azimuth, expressed as:

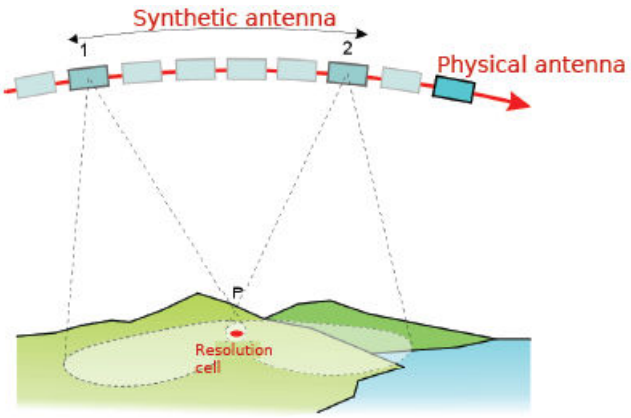

Figure 4.2.1: Synthetic Aperture Radar.

$$L_s = v \cdot T = \frac{\lambda}{D} h \qquad (3)$$

obtained in the range $T = t_0 - t_1$. Moreover we can notice that, by using all the synthetic aperture L_s, we can determine an angular resolution of:

$$\beta_s = \frac{\lambda}{2L_s}, \qquad (4)$$

twice higher than the one of a real aperture radar at the same length (synthetic). Combining the two equations we can obtain:

$$\Delta L_s = \beta_s h = \frac{D}{2} \qquad (5)$$

thus obtaining a spatial resolution in azimuth direction useful in order to monitorate and equal to the half length of the real antenna.

4.3 Spectral bands

The SAR sensors operate on different bands of the electromagnetic spectrum. Penetration is the key factor for the selection of the frequency: the longer the wavelength (shorter the frequency), the stronger the penetration into vegetation and soil. We show below (Table 4.3.1) the wavelengths usually adopted:

Table 4.3.1: Band, frequency and wavelength for SAR sensors.

Band	Frequency (GHz)	Wavelenght (cm)	Satellite
P-band	0,225 – 0,39	140 – 76,90	AIRSAR
L-band	0,39 – 1,55	76,90 – 19,30	JERS-1, SAR, ALOS PALSAR
S-band	1,55 – 4,00	19,30 – 7,50	Almaz-1
C-band	4,00 – 8,00	7,50 – 3,75	ERS-1/2 SAR, RADARSAT-1/2, ENVISAT ASAR,RISAT-1
X-band	8,00 – 10,90	3,75 – 2,75	TerraSAR-X-1, COSMO-Skymed
K-band	10,90 – 36,00	2,75 – 0,83	Military domain/GBSAR

It is worth pointing out that in the last years the K-band is also used for civil application (landslide monitoring) by means of Ground Based SAR.

4.4 Radar images characteristics

4.4.1 SAR acquisition mode

Depending upon the system configuration, SAR sensors can acquire data in different modes (Figure 4.4.1.1).

- **Stripmap**: antenna pointing is fixed relative to the flight line (usually normal to the flight line). The result is a moving antenna footprint that sweeps along a strip of terrain parallel to the path motion. The stripmap mode is normally used for the mapping of large areas (usually with coarse-resolution data)
- **ScanSAR**: The sensor steers the antenna beam to illuminate a strip of terrain at any angle to path of platform motion. The principle of the ScanSAR is to share the radar operation time between two or more separate sub-swaths in such a way as to obtain full image coverage of each.
- **Spotlight**: The sensor steers its antenna beam to continuously illuminate a specific (predeterminated) spot or terrain patch being imaged while the platform flies by in a straight line. The spotlight mode is a practical choice when the mission objective is to collect fine-resolution data from one or more localized areas. The advantages are: 1) the spotlight mode offers finer azimuth resolution than that achievable in stripmap mode using the same physical antenna, 2) spotlight imagery provides the possibility of imaging a scene at multiple viewing angles during a single pass.

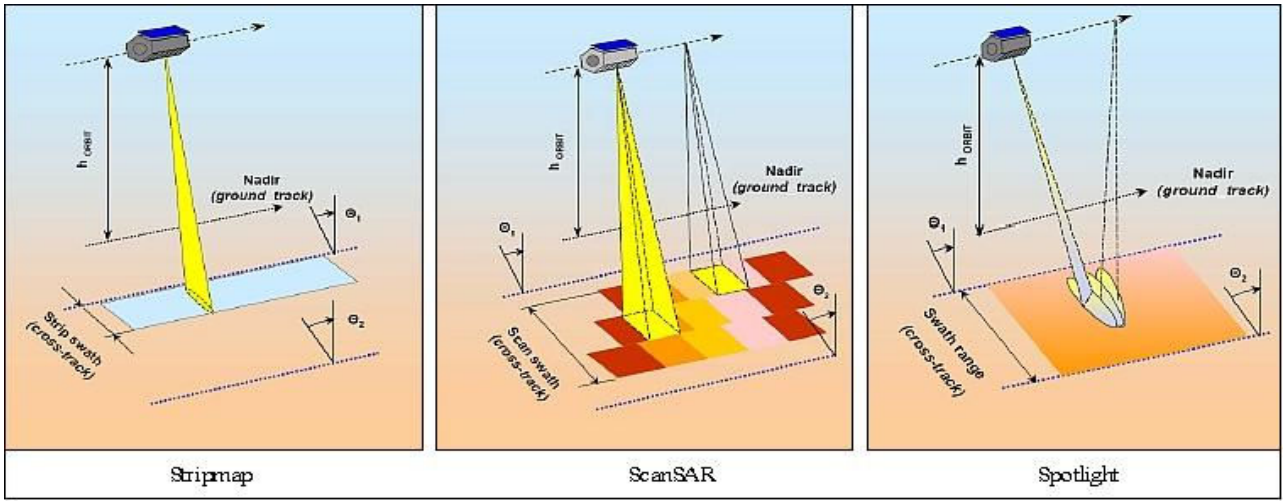

Figure 4.4.1.1: Acquisition mode

4.4.2 Distorsions

The reference frame of a focused SAR image is spanned by the range-azimuth coordinates. Because of the radar is side-looking, ground elevation will result in geometric distortions in the SAR image. Figure 4.4.2.1 shows the effects of foreshortening, layover, and shadowing, caused by the oblique viewing geometry.

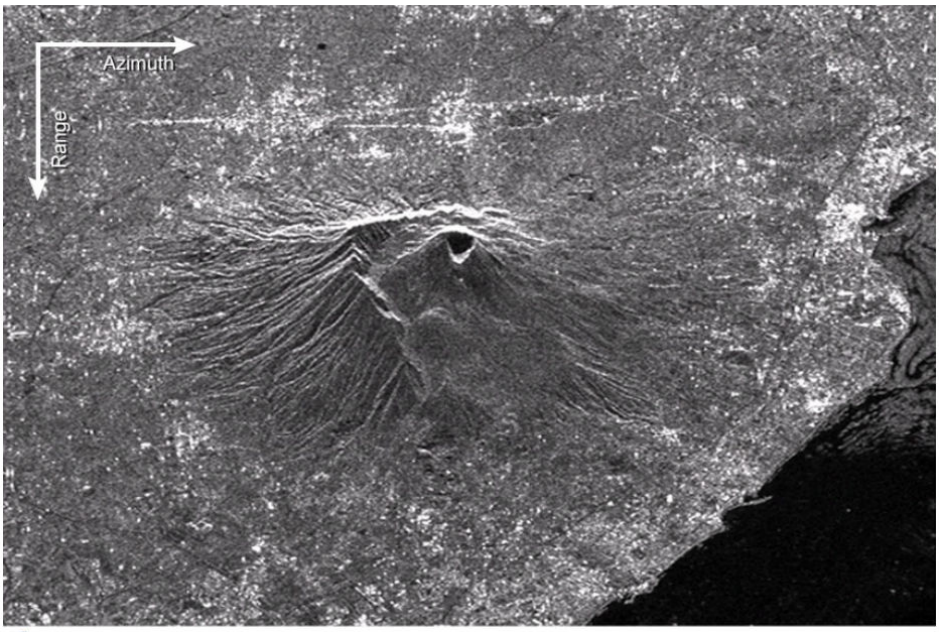

Figure 4.4.2.1: Example of SAR image affected by geometric distorsions (Tele-Rilevamento Europa, 2011).

The geometric distorsions: it is ready to notice that, since the sensor is located in every moment along a certain flying line, and since it gathers data even at a certain distance from it, the image given will show different scales moving from the area underlying the flying line to farther and farther areas. Actually the objects of the image near to the flying area (*near range*) will appear

compressed towards ground range, if we compare them to the farther objects (*far range*). Knowing the height of the sensor and assuming a flat area, it is possible to approximate the real positions of the radar returns. This operation is called *slant-to-ground projection*.

Foreshortening (Fig. 4.4.2.2a) occurs when the radar beam reaches the base of a tall feature tilted towards the radar (e.g. a mountain) before it reaches the top. Because the radar measures distance in slant-range, the slope (from point *a* to point *b*) will appear compressed and the length of the slope will be represented incorrectly (*a′* to *b′*) at the image plane.

Layover (Fig. 4.4.2.2b) occurs when the radar beam reaches the top of a tall feature (*b*) before it reaches the base (*a*). The return signal from the top of the feature will be received before the signal from the bottom. As a result, the top of the feature is displaced towards the radar from its true position on the ground, and ”lays over” the base of the feature (*b′* to *a′*).

The shadowing effect (Fig. 4.4.2.2c) increases with greater incident angle θ, just as our shadows lengthen as the sun sets.

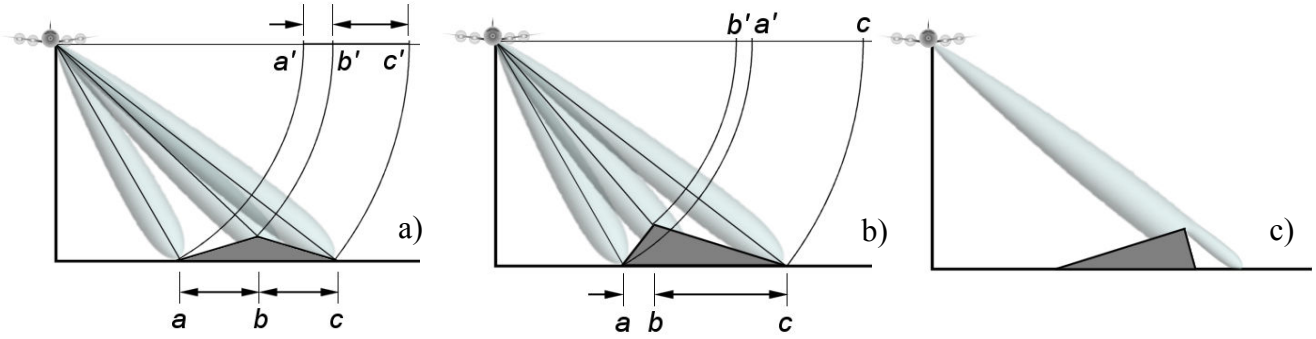

Figure 4.4.2.2: Geometric distorsion effects: foreshortening (a), layover (b) and shadowing (c).

In order to restrict these effects, various techniques have been developed which are based on the use of several images in order to have different view angles and digital elevation models (DEM).

Radiometric distorsions, have, however, an influence on the energy received by the sensor. They are often associated to the geometric ones, for example, since the backscattered energy is collected in slant range direction, the energy received from a foreshortening slope will be stored in a smaller area than the real one, then will be pressed in fewer pixels than it wouldn’t be if we were in geometry ground range. This will lead to have brightness points, because the energy coming from several objects will be combined together. Unfortunately, this effect can’t be adjusted unless with information coming from other sources, essential to validate the results and to understand the topography of the area.

To fully understand this phenomenon we have to understand in which way the SAR data is recorded. When an electromagnetic wave is scattered from a point on the ground *(x,y)*, the features

of the ground cause changes both in the angular phase φ*(x,y)*, and in the amplitude *A(x,y)* of the electromagnetic wave. After the focusing process, the SAR image is complex. The amplitude, which represents the modulus, depends on the scene reflectivity while its phase is proportional to the two-way distance from satellite to ground and therefore to the geometry of the scene. The amplitude image usually allows to distinguish the structures (houses, rivers, rock formation, …) which are in the picture, but they are extremely speckling all the same. The phase image is, on the contrary, always speckling and it doesn't show any kind of structure (but it is essential to the interferometric analysis), while the amplitude, although they are speckling, can be interpreted more easily. Referring to the phase images, the speckle is the cause of the radiometric distorsion. It is the product of the interference among waves coming from the different objects inside the pixel. If we consider k discrete scatterers inside the pixel, we can notice that the wave coming from the satellite interacts with each one of these targets, creating a backscattered wave equal to:

$$Ae^{i\phi}=\sum_{k=1}^{N} A_k^{i\varphi_k} \quad (6)$$

The interference let the return signals to be amplified or weakened according to the related phase. Moreover we need to consider that the intensity of the backscattered signal isn't always the same, but it is function of the frequency band adopted by the satellite, as shown in picture 4.4.2.2, and the typical scattering workings of the single targets, as well as the pulse incidence angle (Figure 4.4.2.3). It is possible to reduce the *speckle* through *multilook* processing and spatial filtering. As for *multilook* processing, the observation period of the returns is divided in shorter sub-periods. During every sub-period the instrument gets "a look" on the object. Using the average of these intervals we obtain the final image. This operation, however, reduces the spatial resolution.

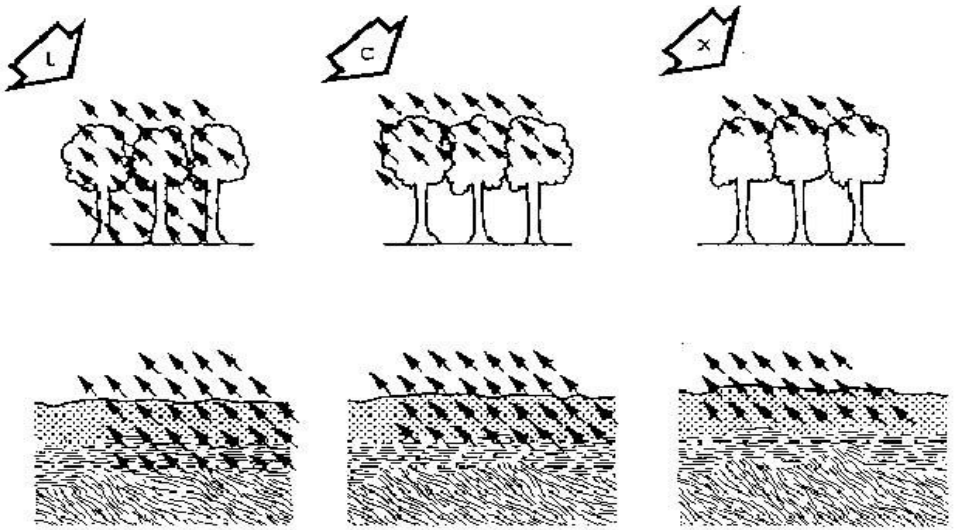

Figure 4.4.2.2: Penetration capacity for the electromagnetic wave for L, C and X band: trees (above), soil (below).

Another way to reduce the *speckle* is by applying spatial filters to the image, among which there is the Lee filter, the improved Lee filter, Frost filter, the improved Frost filter, the Gamma filter and the Kuan filter as better shown in Hanssen, 2001.

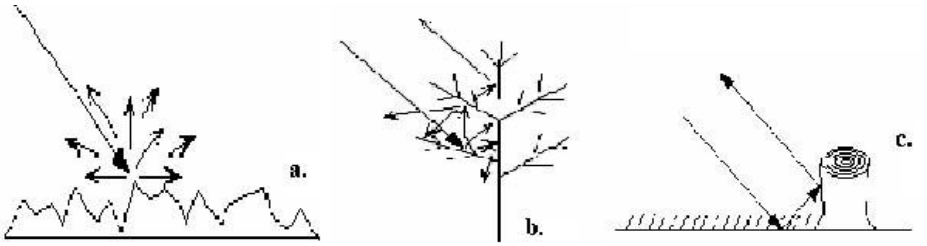

Figure 4.4.2.3: Backscattering mechanism: a) superficial, b) volume and c) double bounce.

4.5 Spaceborne SAR Sensors

The main features of satellites on which SAR sensors are built are outlined below:

ERS-1 and ERS-2 SAR
Agency: European Space Agency (ESA)
Frequency: Band C
Ground resolution: 25 m
Acquisition mode: Stripmap
Swath: 100 km
Repeat cycle: 35 giorni
Lauched: 1991-2000 (ERS-1) e 1995 (ERS2)

JERS-1 SAR
Agency: Japanese Aerospace Exploration Agency
Frequency: Band L
Ground resolution: 20 m
Acquisition mode: Stripmap
Swath: 70 km
Repeat cycle:44 giorni
Lauched: 1993

RADARSAT-1/2
Agency: Canadian Space Agency
Frequency: Band C
Ground resolution: 10–100 m (Radarsat-1) 3100 m (Radarsat-2)
Acquisition mode: Stripmap e ScanSAR
Swath: 50-500 km
Repeat cycle : 24 giorni
Lauched : 1995 (Radarsat-1) e 2007 (Radarsat-2)

ENVISAT ASAR
Agency: European Space Agency (ESA)
Frequency: Band C
Ground resolution: 15–1000 m
Acquisition mode: Stripmap e ScanSAR
Swath: 100-405 km
Repeat cycle: 35 giorni
Lauched: 2001

Alos-Palsar
Agency: Japanese Aerospace Exploration Agency
Frequency: Band L
Ground resolution: 7-100 m
Acquisition mode: Stripmap, ScanSAR
Swath: 20-350 km
Repeat cycle: 44 giorni
Lauched: 2006

TerraSAR-X-1
Agency: Infoterra (Germany)
Frequency: Band X
Ground resolution: 1-16 m
Acquisition mode: Stripmap, ScanSAR e Spotlight
Swath: 15-60 km
Repeat cycle: 11 giorni
Lauched: 2007

COSMO-SKYMed
Agency: Italian Spatial Agency (ASI)
Frequency: Band X
Ground resolution: 1-100 m
Acquisition mode: Stripmap, ScanSAR e Spotlight
Swath: 20-400 km
Repeat cycle: 4 giorni
Lauched: 2007-2010 (4 satelliti)

Sentinel-1
Agency : European Spatial Agency (ESA)
Frequency : Band C
Ground resolution : 15-1000 m
Acquisition mode : Stripmap, ScanSAR e Spotlight
Swath: 100-405 km
Repeat cycle : 6 giorni
Lauched : 2013 (2 satelliti)

ERS 1/2: the two European Remote Sensing satellites, ERS-1 and ERS-2, were ESA's first real Earth observation missions, carrying an imaging Synthetic Aperture Radar (SAR), a radar altimeter and ocean surface temperature and sea winds instruments. ERS-1 was launched in 1991 and deactivated in March 2000. ERS-2, carrying an additional ozone sensor, then it was launched in 1995 and deactivated in 2011.

JERS-1: is an Earth Observation Satellite to cover the global land area for national land survey, agriculture, forestry, and fishery, environmental protection, disaster protection, and coastal monitoring, etc. focusing on observation around the world and resource exploitation. It was launched into a solar-synchronous sub-recurrent orbit at an altitude of 568 km with a recurrent period of 44 days by the H-I launch vehicle on February 11, 1992 from National Space Development Agency of Japan (NASDA) Tanegashima Space Center, and has been continuing to observe and collect data with a mission data recorder by the high performance Synthetic Aperture Radar (SAR).

RADARSAT-1/2: Radarsat1 was launched on November 4th, 1995 and is Canada's first commercial Earth observation satellite developed to monitor the planet's natural resources and environmental changes. It is equipped with a state-of-the-art synthetic aperture radar (SAR) instrument that can be steered to collect data over a 1,175 km wide area using 7 beam modes. This provides users with superb flexibility in acquiring images with a range of resolutions, incidence angles and coverage areas. RADARSAT-2 is Canada's next-generation commercial SAR satellite. The satellite was launched on December 14th, 2007. RADARSAT-2 provides powerful new capabilities which include high resolution imaging, flexibility in selection of polarization, left and right-looking imaging options, shortened programming, processing and delivery timelines, superior data storage and more precise measurements of spacecraft position and attitude.

ENVISAT: Envisat was ESA's successor to ERS. Envisat was launched in 2002 with 10 instruments aboard and at eight tons is the largest civilian Earth observation mission. More advanced imaging radar, radar altimeter and temperature-measuring radiometer instruments extend ERS data sets. This was supplemented by new instruments including a medium-resolution spectrometer sensitive to both land features and ocean colour. Envisat also carried two atmospheric sensors monitoring trace gases. The Envisat mission ended on 8th April 2012, following the unexpected loss of contact with the satellite.

ALOS: The Advanced Land Observing Satellite (ALOS) is the satellite that follows JERS-1 and ADEOS and enhances their land observing technology. ALOS will be used for cartography, regional observation, disaster monitoring, and resource surveying. was launched on January .24th 2006.

Terrasar-X: TerraSAR-X was launched on June 15th, 2007 and has been in operational service since January 2008. Following the launch of a second sister satellite, TanDEM-X in early 2010, the two satellites act as a pair. Applications of the high-resolution TerraSAR-X radar imagery include: Topographic Mapping, Surface Movement, Change Detection, Land Cover and Land Use Mapping, Defence and Security Applications, Rapid Emergency Response, Environmental applications.

Cosmo-SkyMed: is a Space-Earth Observation Dual Use System devoted to provide products/services for the following purposes: a) environmental monitoring and surveillance applications for the management of exogenous, endogenous and anthropogenic risks; b) provision of commercial products and services. The constellation consists of 4 satellites, each one equipped with a microwave high-resolution synthetic aperture radar (SAR) operating in X-band.

Finally, **Sentinel satellites** belong to the field of GMES (Global Monitoring for Environment and Security) Program is to provide data, information, services and knowledge that support Europe's goals regarding sustainable development and global governance of the environment.
GMES features several components, including in-situ measurement, Data Infrastructure, Service Provision and a Space Segment; this latter is responsible for the operational provision of Earth observation (EO) data, delivered by a series of 'Sentinel' spacecraft.

The ESA Sentinels constitute the first series of operational satellites for GMES; the GMES space component will use new as well as existing space assets. ESA is currently undertaking the development of three Sentinels mission families:

1. Sentinel-1: Focusing on synthetic aperture radar (SAR) applications
2. Sentinel-2: Providing high-resolution optical observation for GMES land and emergency services
3. Sentinel-3: Providing optical and microwave observation for GMES operational marine and land services

Furthermore, the Sentinel-4, Sentinel-5 Precursor and Sentinel-5 missions are foreseen for later deployment to cover the atmospheric chemistry monitoring requirements.

The Sentinel-1, -2 and -3 missions are based on a constellation of two satellites in the same orbital plane, a configuration that fulfils GMES' revisit and coverage requirements and provides a robust and affordable operational service. Individual satellite lifetimes are specified as seven years, with consumables allowing mission extension up to 12 years. The life-cycle of the space segment is planned to be in the order of 15-20 years.

4.6 SAR interferometry

Interferometry SAR (InSAR), first described by Gabriel et al., 1989 had its first applications (Massonnet et al.,1993), essentially based upon the analysis of single or, at most, few interferences which allow to supply information about deformations of the earth surface. Moreover the development of multipass interferometric techniques (Ferretti et al., 2001; Berardino et al., 2002) enabled to reach excellent results for the quantitative monitoring of deformations along the LOS. The InSAR is based upon the analysis of phase differences between two SAR images acquired in different spatial positions. This phase difference conveniently processed, is compared to the ground topography, determining two kinds of results:

- Digital Elevation Model with high resolution (DEMs);
- Deformation maps characterized by millimeters resolution.

SAR interferometric data have a different content from the simple optical data: the connection extent between two SAR images is, actually, very susceptible to the changes in the nature of the scatters inside the resolution cells (ground pixel). A satellite can observe the same area from slightly different look angles. This operation can be made with the help of two sensors applied on the same platform (for instance the Shuttle NASA missions), or in different periods with the aid of images captured on different satellite orbits. Satellites cover ascending and descending orbits: due to Earth rotation and to the fact that SAR antenna is pointed on the same side with respect to the velocity vector in the orbit trajectory, an area can be enlightened from East during descending orbits (from North to South) or from West during ascending ones. The perpendicular line to the trajectory orbit and the look line form an angle called *look angle*.

If we succeed in combining two acquisitions coming from East and West, we are able to eliminate the many spatial distortions previously described. However it is difficult to acquire two SAR images from ascending and descending orbits at the same time identifying the same targets. When this happens it is possible to decompose the velocity vector. This operation can be better understood by considering a x, y, z Cartesian coordinate system, in which the three directions coincide with the horizontal E-W and N-S and vertical, respectively.

In such reference system the velocity vector V can be calculated as:

$$\bar{V} = V_x \cdot \bar{s_x} + V_y \cdot \bar{s_y} + V_z \cdot \bar{s_z} \quad (7)$$

where V_x, V_y e V_z are the velocity vector components along the horizontal (E-W and N-S) and vertical directions, and s_x, s_y, s_z the unit vectors of the three coordinate axes of the Cartesian system.

Thus, using mean velocity values V_a and V_d, obtained from the PS database, the following system is obtained:

$$\begin{cases} V_a = Vx \cdot s_{xasce} + Vy \cdot s_{yasce} + Vz \cdot s_{zasce} \\ V_d = Vx \cdot s_{xdesce} + Vy \cdot s_{ydesce} + Vz \cdot s_{zdesce} \end{cases} \quad (8)$$

where s_{xasce}, s_{yasce}, s_{zasce}, s_{xdesce}, s_{ydesce}, and s_{zdesce} represent the direction cosines of the respective velocity vectors V_a and V_d.

In this reference system the number of unknown variables (V_x, V_y and V_z) is higher than that of the equations and therefore it cannot be solved. However, due to the geometrical characteristics of the acquisition, the component on N-S direction appears to be negligible.

Velocity in this direction is acceptably approximated to zero, thus allowing to solve the previous system and to assess motion components in E-W and vertical directions (corresponding to x and z directions):

$$\begin{cases} V_a = V_V \cos\theta_{asce} + V_E \sin\theta_{asce} \\ V_d = V_V \cos\theta_{desce} + V_E \sin\theta_{desce} \end{cases} \quad (9)$$

where V_a and V_d are respectively the velocity values in ascending and descending geometry and θ_{asce} and θ_{desce} are the incidence angles in the two geometries.

Actually this technique employs the phase measures to infer the *differential range* (difference between distances perceived by the radar sensor to the same target on two different points of view) and the *range change* (difference between two couples of images, proving that a target transfer took place between the two acquisitions) in the SAR acquisitions concerning the earth surface, while the amplitude is crucial for the co-registration of the images. At computational level, the interferogram is obtained by multiplying one image by the complex conjugate of the other and contains, on a pixel by pixel basis, the phase difference between the two acquisitions. One of the images is taken as a reference (usually the first according to a chronological order), will be called *master*, while the other will be called *slave*. This product is performed on the complex value typical of the single pixel $A_1 e^{i\phi 1}$ for the complex combined of the second $A_2 e^{i\phi 2}$:

$$\Delta A e^{i\Delta\phi} = A_1 e^{i\Delta\phi_1} \cdot A_2 e^{i\Delta\phi_2} = A_1 A_2 e^{i(\phi_1 - \phi_2)} \quad (10)$$

The deriving result will have amplitude ΔA equal to the one of the first image multiplied for the second, while the phase will be the difference between the two.

4.7 Baseline

The geometrical parameters of acquisition are very important in the interferometric analysis. The distance between the two satellites at the time of the evaluation, on the perpendicular plane to the orbit direction, is called *interferometer baseline (B_r)*, while the latter one component projected on the normal direction to the image slave line of slant range is called *perpendicular baseline (B_n)* (Figure 4.7.1). Presuming that initially we have, for each portion of ground enlightened by the radar, just one

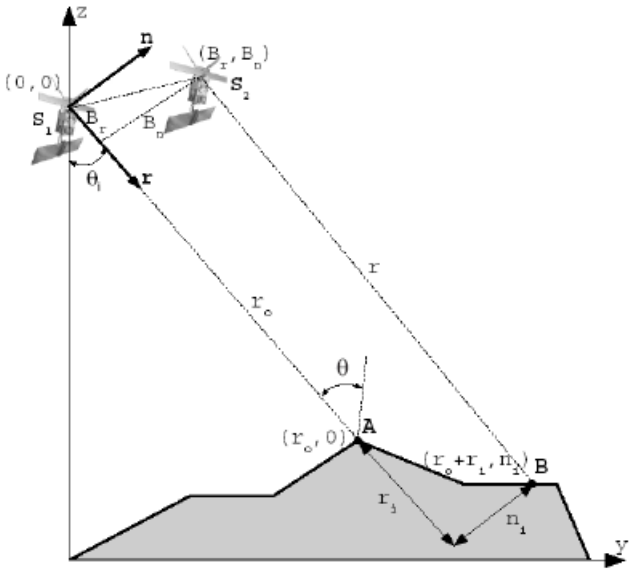

Figure 4.7.1: Interferogram acquisition geometry (Blanco, 2008).

dominant scatter, which remains constant in the time interval of the acquisition. This punctual scatter is observed from two different look angles. Once a reference earth point with given coordinates has been identified, the path difference between the two satellites in the direction of slant range, which is given going from the reference cell on the ground to another, defined as Δr (in the case of small baselines compared to the flying height and compared to not very far earth cells) can be given by the following expression:

$$\Delta r = -2 \frac{B_n q_s}{R} \quad [\text{m}] \quad (11)$$

where: B_n = perpendicular baseline, R = distance in slant range between target and sensor and q_s = distance between two points on earth in perpendicular direction to the slant range.

The phase interferometric difference $\Delta\varphi$ corresponding to a path difference Δr between the two satellites, is proportional to the relationship between a complete phase cycle in radians (equal to 2π) and the wavelength λ, that is the distance between the two following peaks, all multiplied for

Δr:

$$\Delta\varphi = \frac{2\pi\Delta r}{\lambda} = \frac{4\pi}{\lambda} \cdot \frac{B_n q_s}{R} \qquad \text{[rad]} \quad (12)$$

This phase can be then divided in two contributions:

– a component that is proportional to the height difference q (Figure 4.7.2) between the reference and the recorded point;

– the other component that is proportional to the distance *s* along the slant range direction, between the two points.

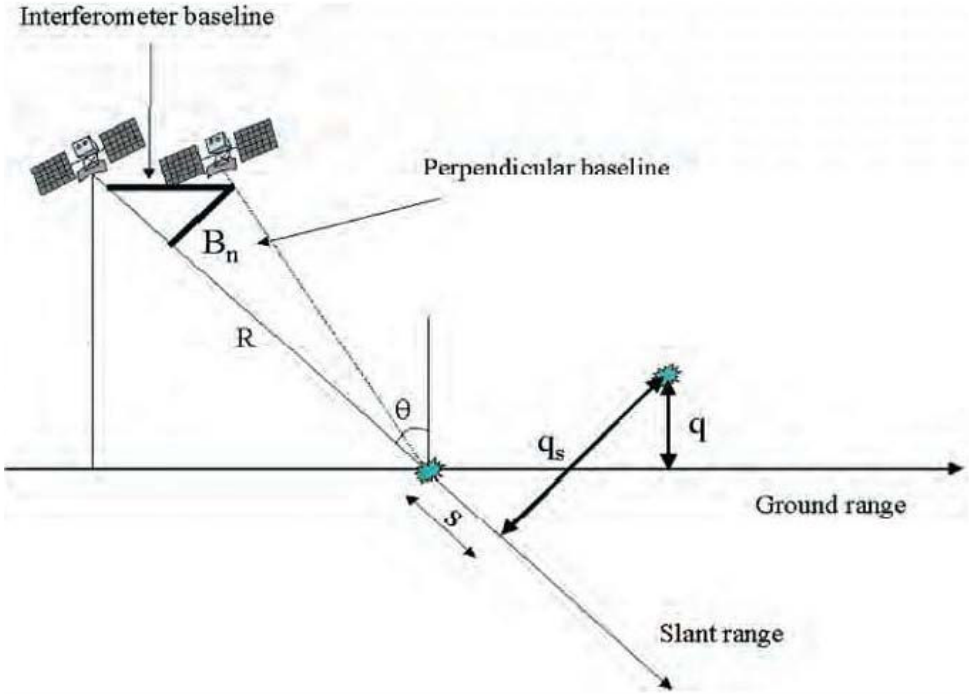

Figure 4.7.2: Geometry for interferometric acquisition.

$$\Delta\varphi = = -\frac{4\pi}{\lambda} \cdot \frac{B_n q_s}{R \sin\theta} - \frac{4\pi}{\lambda} \cdot \frac{B_n s}{R \tan\theta} \qquad \text{[rad]} \quad (13)$$

where:

θ = local incidence angle on the slant range direction which *s* e q_s are referred to.

We consider B_n known from orbital data. The second term can be calculated or eliminated starting from equation (9), once we know the morphology of the analysed territory. If the DEM used has a very low precision, or it is even a reference ellipsoid, such a procedure (called *interferogram flattening*) creates, as a result, a proportional phase map to the residual ground height. However, in case the DEM is accurate, the procedure leads to a repositioning map.

The phase discontinuities we can notice in the interferogram flattened in Figure 4.7.3, which

look like level bend, represent the phase differences depending either on discontinuity (and displacements) in the ground morphology, or simply due to incongruities between a cyclical phase ± 2π and a linear colour scale (black=1°, white= 360°, or viceversa).

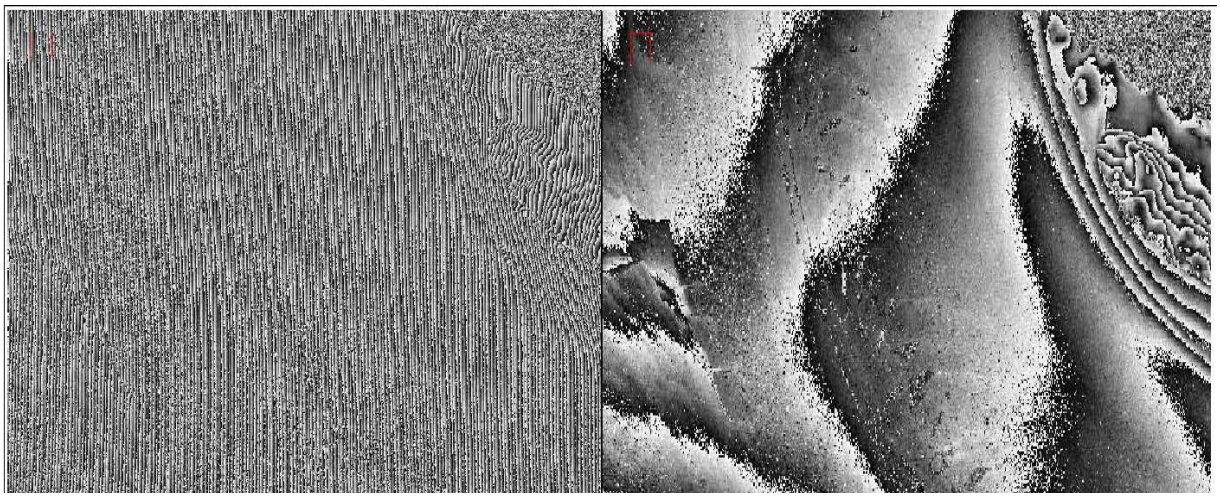

Figure 4.7.3: Comparison between interferogram (left) and interferogram flattened (right).

Actually in the latter instance, the increasing of quote corresponding to 1° which takes place between a phase 360° and the phase 1° involves indeed the creation of an interferometric fringe. We can notice that without further information, it isn't possible to evaluate the ambiguity of ± 2π*k*, with *k* whole number, which can be found between two consecutive fringes, and therefore it isn't possible to know beforehand if there is or not a topographic residual between two points which are enclosed by an interferometric fringe.

The height difference module corresponding to a gap between two fringes will be equal or multiple of h_a (*altitude of ambiguity*) defined, therefore, as the difference of height which generates a change in the interferometric phase of 2π after the interferogram flattened:

$$h_a = \frac{\lambda R \sin\theta}{2B_n} \text{ [m]} \quad (14)$$

as noticed, such a value is inversely proportional to the baseline perpendicular B_n. In general, the larger is the perpendicular baseline, the more accurate is the computation of the height; therefore a high presence of fringes can determine a more accurate map of the ground elevation, but even with more ambiguity. An interferogram with high baseline will be indeed more sensible to slope variations, compared to a shorter baseline one.

However the baseline has a high-ranking limit, represented by the so called critic baseline, beyond which the phase signal is just noise.

Therefore the flattened interferogram produces a measure of quote affected by ambiguity, due to the periodicity (2π) of the interferometric phase. Yet the variation of phase between two points,

can represent a measure of the real variation of height, if we eliminate all the cycle slips corresponding to the fringes that are on the image. The addition process of whole multiples of 2π to the interferometric phase is called Phase Unwrapping. There are many techniques which contribute to the creation of this procedure, but none of them represents a univocal method. Once unwrapped the image, we can directly go from the phase to the altimetric information, obtaining a SAR elevation map, and once it is georeferenced on a suitable ellipsoid (e.g.WGS84) and sampled again on a suitable reference grid (e.g. UTM), it represents, in effect, a DEM, that can be used in various applications in local and environmental field (from the city planning to the control of natural risk management).

4.8 Differential Interferometry

The interferometric processing of the image, besides supplying elevation maps, can, as we said before, also provide to notice slight position relative changes among different points on the same one. These deformations take place on the survey ground because of sudden events (e. g. an earthquake), or slow natural events (consider the glacier melting), or caused, even partially, from the anthropogenic activity (as in the case of fluid extraction which generates subsidence phenomena). In such cases, we can add the expression of the interferometric phase $\Delta\varphi$ an additional term independent from the baseline:

$$\Delta\varphi = \frac{4\pi}{\lambda} d \quad (15)$$

where:

d = distance covered because of a displacement of the scatter, projected on slant range. In this way, after the interferometric flattened, the residual phase will include few height factors (topographical residual), and many deformation factors (distortion components):

$$\Delta\varphi = \frac{-4\pi}{\lambda} \cdot \frac{B_n q}{R \sin\theta} + \frac{4\pi}{\lambda} d \quad (16)$$

Therefore, if a DEM with an adequate precision is available, the contribution of known topography can be almost completely removed from the interferometric phase, $\Delta\varphi$, so as to measure the ground motions in the so called differential interferogram. Finally we have to consider that the precision of the SAR concerning the motions of the grounds is far greater compared to the altimetric measure of the date: a $\lambda/2$ deformation to the slant range direction generates a 2π phase variation. Therefore, the precision both of the elevation maps and the motion ones depends on a

wide quantity of parameters both structural and geometric which vary according to the single acquisition, since it isn't beforehand definable.

4.9 Error sources

As we have seen so far, the interferometric phase, outcoming from the path difference of the slant range signal between two acquisitions, in theory would only depend on the elevation differences between the two images and the deformation related to them. Basically, however, such a signal will see the contribution of other different factors, which can be summed up to form the interferometric phase. The different contributions to the interferometric phase can be described as it follows:

$$\Delta\varphi = 4\pi \frac{R_1 - R_2}{\lambda} = \Delta\varphi_{topo} + \Delta\varphi_{mov} + \Delta\varphi_{flat} + \Delta\varphi_{atm} + \Delta\varphi_{noise} \qquad (17)$$

Besides the topographic contribution $\Delta\varphi_{topo}$ and the one deriving from the earth surface motion $\Delta\varphi_{mov}$, other three factors contribute to the definition of the interferometric phase for a given diffusor inserted in an earth cell:

A) $\Delta\varphi_{flat}$

The parameters which identify the satellite position during the acquisition of the image on the ground are called orbital parameters, and they are made up of a series of points on the satellite orbit path, whose position and speed are known. This information is usually given by the service supplier. In order to minimize the error more accurates state vectors (position and speed) are needed. This data was obtained from the European Space Agency and from other institutions and universities several months after the satellite acquisition.

B) $\Delta\varphi_{atm}$

When two SAR images are acquired in different dates, the travelling speeds of the electromagnetic waves are different due to the atmosphere variations. This signal disturbance can take place due to variations in humidity, temperature and pressure in the air. This effect usually arouses a phase shift included inside a single cycle 2π, with a gradual variation inside the image. That is why, having at your disposal a wide range of images of the same area, which have very different conditions of acquisition, it is possible, relating every one of them to only one master image, to eliminate a part of this disturbance, following the APS pattern (Atmospheric Phase Screen) for the spreading in atmosphere. Another possibility can be to use atmosphere patterns

specifically realized for the area of interest, which are also able to determine a phase shift contribution due to the tropospheric refractivity when the signal passes through.

C) $\Delta\varphi_{noise}$

Atmospheric effect is not usually predominant in the phase noise, but the latter is the sum of several distributed factors, which can vary considerably through time between two acquisitions. As we said before, the elements which create a phase interference of phase speckle are mainly:

- *Variation of the scatters*, mainly for densely lush reservoirs and areas densely lush, which change in few milliseconds, the response on earth of the signal will hardly supply comparable values, even if it is acquired in a short time. This factor can be defined *temporal decorrelation*.
- *Variation of the incidence angle,* which has as a main consequence the variation of the critic baseline, beyond which the response is only noise. This factor depends on the dimensions of the pixel on earth, and the ground formation, on the radar frequency and the distance from the sensor – target. In order to reveal this special contribution to the noise we can use the term *spatial decorrelation*.
- *Volume scattering,* when there is a volumetric distribution of scatters on the resolution cell, the incident signal can carry out different paths inside it, with a different number of rebounds, return time, and so on. As the previous, this decorrelation source depends on the critical baseline too.

4.10 Applications

In the last twenty years many DInSAR applications have been developed, and the capability of the DInSAR has been extensively documented. A great contribution to this success certainly comes from different fields of geosciences. Some of the most relevant DInSAR application fields are discussed below:

- Seismology: probably represents the field where the major number of scientific achievements have been obtained, including different types of coseismic studies, see e.g. (Massonnet et al., 1993; Peltzer and Rosen, 1995; Peltzer et al., 1999; Reilinger et al., 2000; Pedersen et al., 2001); post-seismic deformation studies (Peltzer et al., 1996; Massonnet et al., 1996), and inter-seismic tectonic events (Wright et al., 2001; Colesanti et al., 2003). As it is described later in this paper, such types of deformations can only be achieved by using advanced DInSAR processing and analysis tools.

- Volcanology: represents another relevant application field, with several studies of volcanic deflation and uplift, e.g. see (Massonnet et al., 1995; Lu et al., 2000; Salvi et al., 2004). Several examples of DInSAR applications to volcanology are described in Massonnet and Sigmundsson 2000.

- Glaciology: different researches have been led in this domain. They included InSAR ice topography measurements (Kwok and Fahnestock, 1996); ice velocity measurements (Goldstein et al., 1993; Joughin et al., 1996; Mohr et al., 1998); and other glaciological applications, like the determination of the discharge of glaciers (Rignot et al., 1997; Joughin et al., 1999).

- Landslides. In this important application several results have been achieved. However, with the A-DInSAR techniques for some types of landslide phenomena (slow and extremely slow movement) it has been possible to perform DInSAR deformation measurements. The most relevant results are described in Fruneau et al. 1996; Hilley et al. 2004; Delacourt et al. 2004; Colesanti & Wasowky 2006; Meisina et al., 2008; Herrera et al., 2009, Cascini et al., 2010.

- Ground subsidences and uplifts due to fluid pumping, construction works, geothermal activity, etc. have been described in several papers, see e.g. Massonnet et al. 1997; Galloway et al. 1998; Amelung et al. 1999; Wicks et al. 2001; Crosetto et al. 2003; Lanari et al. 2004; Cascini et al., 2009**.** Most of the published results concern urban areas, over which DInSAR data remains coherent even with large observation periods.

- Infrastructures: deformations monitoring of man-made structures, such as dams, buildings and transport infrastructures, see e.g. Perissin et al., 2009; Proto et al., 2010; Stabile et al., 2012.

4.11 Interferometric algorithms

A first attempt to develop advanced DInSAR techniques is represented by the algorithms referred to as stacking approaches (Peltzer et al*.,* 2001); these techniques are focused on reducing the effects of the phase artifacts due to changes in the atmospheric conditions between the acquisition SAR pairs (atmospheric artifacts) and/or those due to the uncertainties in the sensor orbit information (orbital artifacts). The stacking techniques essentially calculate a weighted average of all the deformation velocities computed from single interferograms (the weights being the corresponding time spans) and allow providing an improved estimate of the mean deformation rate of the investigated area.

However, it was with the development of techniques aimed at computing deformation time series from sequences of SAR images that the DInSAR techniques made a major step forward. These advanced DInSAR approaches typically require few tens of images (typically at least 20–30) to be reliably exploited and can be roughly grouped in two main categories: techniques that work on

localized targets, referred to as Persistent Scatterers (PS) methods (Ferretti et al., 2000; Werner et al., 2003; Arnaud et al., 2003, Hooper et al., 2004, Duro et al., 2005, Costantini et al., 2008, Iglesias et al., 2012), and those that also use distributed targets, referred to as Small BAselines Subset (SBAS) methods (Berardino et al., 2002; Mora et al., 2003; Lanari et al., 2004; Prati et al., 2010), although a solution that incorporates both the PS and SBAS approaches has been also recently proposed (Hooper, 2008).

4.12 Coherent Pixels Technique

Among the different algorithms previously mentioned, in this work we have focused on the application of the algorithm implemented by Mora et al., 2003 - Coherent Pixels Technique (CPT) at the Remote Sensing Laboratory (RSLab) of the Universitat Politecnica de Catalunya (UPC)

CPT is able to extract from a stack of differential interferograms the deformation evolution over wide areas during large time spans. The former is achieved thanks to the coverage provided by current SAR satellites, like ESA's ERS or ENVISAT, Terrasar-X and Cosmo-SkyMed, while the latter due to the large archive of images acquired since 1992.

The processing scheme is composed of three main steps: a) the generation of the best interferogram set among all the available images of the zone under study; b) the selection of the pixels with reliable phase within the employed interferograms and, c) their phase analysis to calculate, as the main result, their deformation time series within the observation period. Following will be described the steps above mentioned.

Before to explain in detail the different steps is worth to pointing out that the first pass in the interferometric processing is the co-registering. When multiple images cover the same region and, in particular, a speckle filtering based on time-series will be performed, or image rationg (or similar operations) are required in the original slant range geometry, SAR images must be co-registered. This requires spatial registration and potentially resampling (in cases where pixel sizes differ) to correct for relative translational shift, rotational and scale differences. Note that co-registration is simply the process of superimposing, in the slant range geometry, two or more SAR images that have the same orbit and acquisition mode. In detail the registration process made by CPT algorithm consists in:

Coarse registration: Align the cropped images with an accuracy of a pixel for the whole image. This step is performed doing the amplitude correlation of a portion of both images;

Fine registration: Align the cropped images with an accuracy of a fraction of pixel, processing each pixel separately. This step can be done also with amplitude correlation of block divided images or with geocoding techniques that require an external DEM and the orbital

information.

a) The aim of the generation of best interferogram set is to identify the minimum number of interferograms in the stack which have the maximum quality overall. In order to do the selection, from all the available images, the spatial baseline, the temporal baseline (B_t) and the Doppler frequency (D_f) are considered. In order to estimate the perpendicular baseline values (B_n) a reference image is selected. Generally, that image is the one that has been used as the reference one in the co-registering process. After that, interferograms selection is done by means of Delaunay triangulation of the available images in the $\{B_n,B_t,D_f\}$ space, so every arc connecting a pair of images represent an interferogram.

b) Terrain deformation cannot be always detected from all the pixels within the area under investigation since, due to decorrelation, only part of them would have enough phase quality along acquisition. There are different criteria in order to do the pixel selection based on the coherence stability (Berardino et al., 2002) and the amplitude dispersion (Ferretti et al., 2001). Here will be briefly described only the pixel selection criterion based on the coherence stability. Such criterion is based on the spatial coherence estimator (Seymour et al., 1994). Such estimator is defined as:

$$\gamma = \frac{\sum_{n=1}^{ML} y_1^{(n)} y_2^{*(n)}}{\sum_{n=1}^{ML} y_1^{(n)2} \sum_{n=1}^{ML} y_2^{(n)2}} \qquad (18)$$

where y1 and y2 are the master and slave complex images, respectively. The phase of this complex coherence is in fact the multi-looked (or averaged, ML) interferometric phase while its magnitude is the phase quality estimator. The size of the required coherence estimation window worsens the spatial resolution. Typical ML are 3*15 or 4*20 pixels (range and azimuth, respectively) which represent 60*60 meters and 80*80 meters ground spatial resolution. The standard deviation of the interferometric phase, σ_φ, can be calculated from the estimated coherence, γ, and the multilook (Hanssen,2001) as shown in Figure 4.12.1 A pixel will be selected if it shows a coherence higher than the threshold in a certain percentage of interferograms.

c) The last step consists in phase analysis to calculate their linear deformation time series within the observation period.

The phase of each pixel is difficult to evaluate due to the occurrence of an offset among the different interferograms. In order to overcome this constraints, CPT relates the neighboring selected pixels by means of a Delaunay triangulation. This kind of triangulation allows to connect neighboring pixels with non-overlapped triangles. The selected pixels are the nodes of the mesh and the connections among the pixels represent the links. In order to reduce the atmospheric effects the

length of this links are set up. After the triangulation is possible to evaluate the phase increment between two neighbouring pixels. If the maximum connecting distance between pixels has been properly fixed, then the atmospheric term can be considered negligible. Since the linear velocity term and DEM error are constants for each node in the whole set of differential interferograms, it is possible to retrieve a good estimation of them adjusting the phase model, to the available data.

Finally, an integration process is necessary to obtain the velocity values for each pixel. It is necessary to identify a control point (named seed) characterized by linear velocity and height well-known. In practice, many stable points not affected by deformation are used, depending on the extent of the area and the infield information available. A good distribution of control points helps to reduce the offsets that could appear among zones badly connected. Depending on the chosen threshold, selected pixels may vary in a wide quality range, and consequently so it will the quality of the estimations on the increments of the linear parameters. Furthermore, bad links will lead to wrong velocity values after the integration process. In order to obtain larger pixel density but preserving the suitability of the result quality multi-layer processing has been implemented (Blanco et al., 2006). Selected pixels are divided into different layers according to their quality. After that, beginning with the top layer, the linear block is iteratively executed by adding successive layers, so the obtained absolute values of each layer act as the seed values to the following integration process. By doing this, the results obtained with the high quality layers are preserved and the estimation of the low quality layers improves. Consequently, multi-layer processing improves linear results and rises pixel density while providing a quality label for each one.

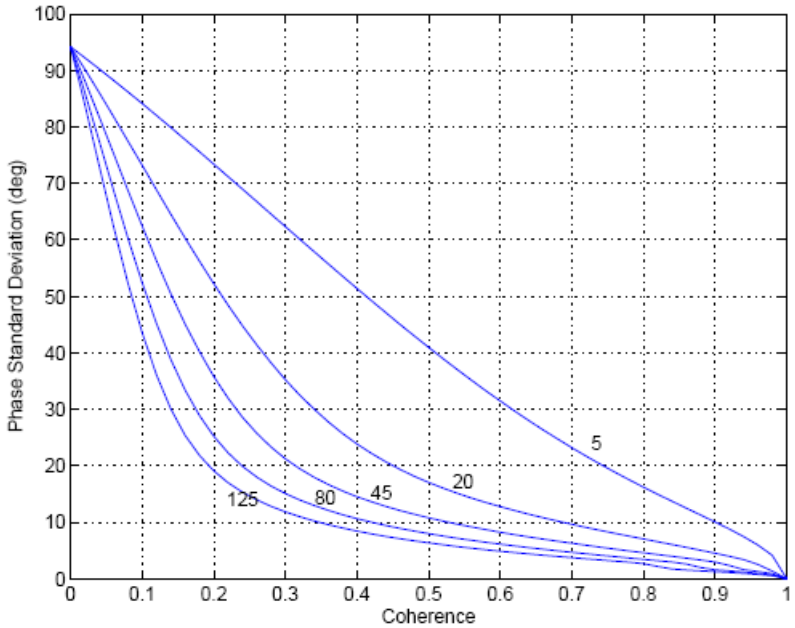

Figure 4.12.1. Phase standard deviation vs coherence for different number of multilook (Blanco, 2009).

After calculating the contribute of linear deformation, it is possible to calculate the non-linear component in order to obtain the complete evolution of deformation. The first step of the non-linear model consists in the calculation of the phase residues $\varphi_{residue}$, obtained by subtracting the absolute linear phase model φ_{model} from the original interferometric phases φ for the selected pixels:

$$\varphi_{residue} = \varphi - \varphi_{model} \quad (19)$$

The residual phases are calculated only in correspondence of reliable pixels. The phase residues consists in 2 terms:

- Atmospheric perturbations. This term can be considered as a low spatial frequency signal in each image due to its approximately 1 km correlation distance. However for each acquisition date atmospheric conditions can be considered random.
- Non Linear deformation. This term can be assumed to present a narrower correlation window in space (or at least much narrower than atmospheric artefacts) and a low pass behaviour in time.

Starting from these considerations is possible to separate the atmospheric artefacts from the non-linear deformation applying a filtering process in both spatial and temporal domains in order to obtain the time-series of the deformation, as in detail described in Blanco et al., 2008.

CHAPTER 5

5. Application of DInSAR technique: case studies

This chapter illustrates the results of the interferometric analyses on the four test sites (Agnone (IS), Costa della Gaveta (PZ), Moio della Civitella (SA), Calitri (AV)). ENVISAT ASAR images over the 2002-2010 period were processed for all sites by the application of CPT technique. Both acquisition geometries (ascending e descending) were available for some sites, while for others the analysis was carried out on PS processed by T.R.E. (spin-off of Politecnico di Milano). All the above mentioned data were available thanks to a specific agreement between the Department of Hydraulic, Geothecnical and Environmental Engineering of the University of Naples and the Italian Ministry of Environment (MATTM) for the acquisition of PS interferometry data and of the related SAR images within the Italian Extraordinary Plan for Environmental Remote Sensing.

Finally, last generation images (VHR-Very High Resolution) acquired from ASI satellite constellation were processed only for the Agnone site thanks to the project "*Application of DInSAR technique for the slow moving landslides monitoring*", proposed by the Department of Hydraulic, Geotechnical and Environmental Engineering and Department of Biomedical, Electronics and Telecommunications Engineering of the University of Naples *Federico II* in the First Announcement of Opportunity Cosmo-SkyMed.

5.1 Agnone (Isernia)

5.1.1 Geological settings and landslides

The geological setting (Fig. 5.1.1.1) of the Agnone "Colle Lapponi" landslide is characterized by the presence of Agnone Flysch, a structurally complex formation dated to Upper Miocene (Vezzani et al., 2004). In the study area, the lower member of the Agnone Formation is present, made up of marly clays, clayey marls, silty-sandy clays and subordinate sandy levels, with intercalated carbonate beds. The clayey-marly terms show features typical of a weak rock and a scaly structure; along the scales, weathering evidences can be found, represented by reddish coatings. The formation is overlain by a weathered mantel, constituted by brownish-yellowish clays, silty clays, often iron-oxidated, rich in organic matter and including heterometric carbonate fragmants (Calcaterra et al., 2008).

The landslide is a complex slope movement (Fig. 5.1.1.2), consisting of a roto-traslational slide which evolves in an earth-flow. The landslide took place in the catchment of Vallone S. Nicola, a tributary to the Verrino Torrent, which runs west of Agnone. It was the consequence of the intense pluviometric event that occurred in January 2003 in southern Italy. The landslide caused serious damage to rural buildings and the local road network (Fig.5.1.1.3). The main social consequence was the cautional evacuation of 15 families from their house, located in the areas directly affected by the slope movement or in its immediate surroundings (Calcaterra et al., 2008).

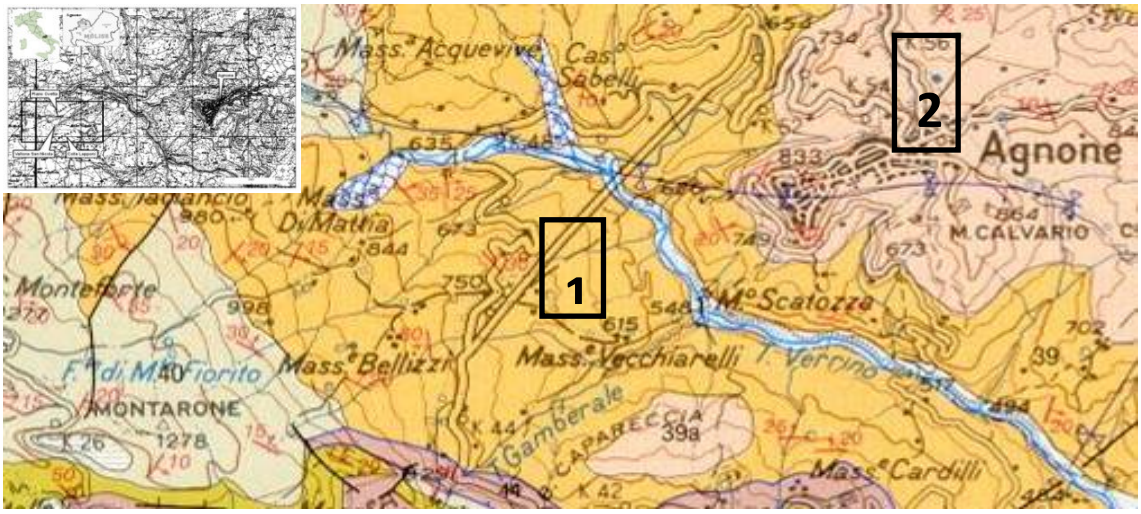

Figure 5.1.1.1. Excerpt from Geological map of Molise region (Vezzani et al., 2004): 1) Agnone Flysch: alternating clays and sandstones, with levels of sandstone turbidites; 2) Agnone Flysch: alternating clays and sandstones, interbedded with limestones.

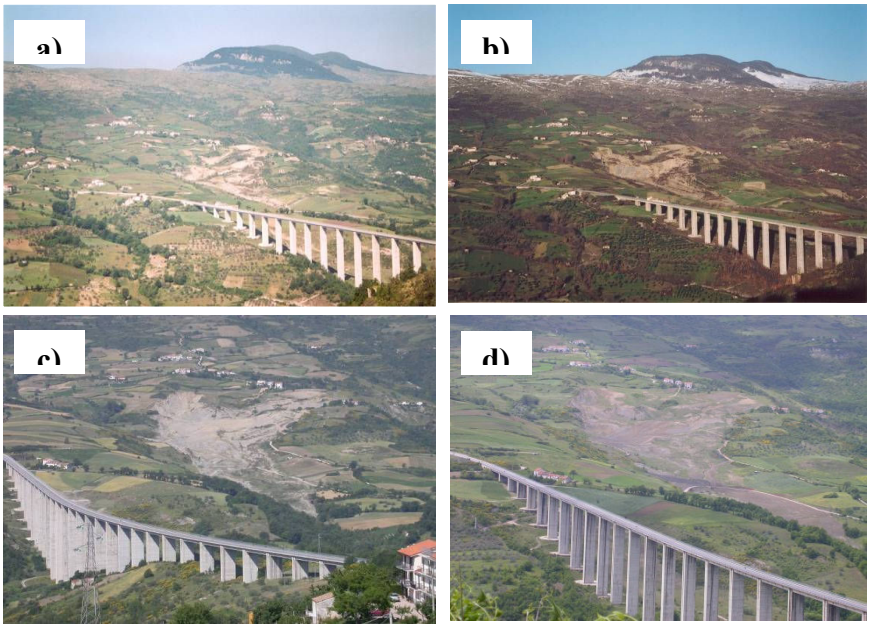

Figure 5.1.1.2. Agnone landslide: a) 2003; b) 2004; c) 2005; d) 2007.

Figure 5.1.1.3. Damages to rural buildings and the local road network

As evident from Figure 5.1.1.4, and confirmed by different geomorphological surveys (the last one dating July 2011), the landslide has shown both an advancing (2004-2006) and a retrogressive (2006-2011) tendency, which resulted in an overall increase in the unstable area, evaluated in about 80,000 m2 from 2004 to 2006, and 40,000 m2 from 2006-2011, reaching a global value of about 280,000 m2. From 2004 to 2011 the foot has progressed of about 350 m and the toe has retrogressed of about 270 m; consequently, the landslide has reached a total length of about 1500 m.

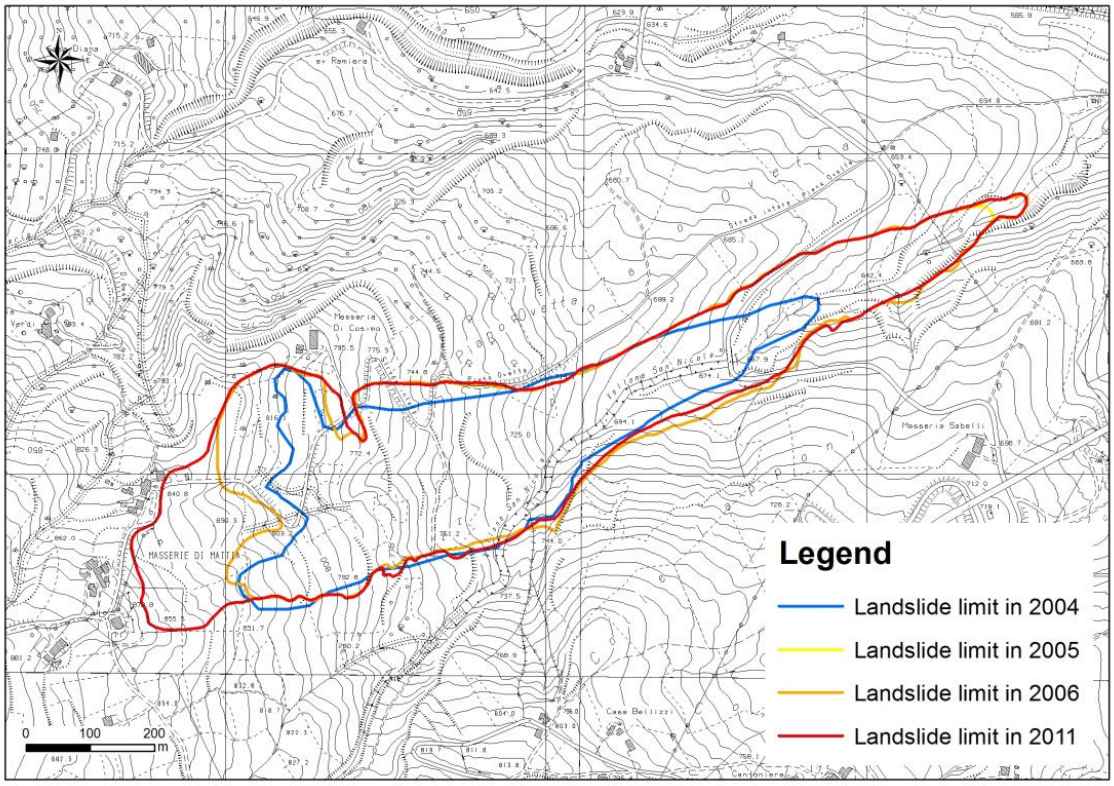

Figure 5.1.1.4. Plan view of the Colle Lapponi landslide and its evolution in the time-span June 2004-July 2011.

A site investigation, carried out in 2006, allowed an in-depth analysis of the lithostratigraphical features of the terrains, explored down to 40m from the ground surface. Four homogenous horizons have been recognized, of which their characters are as follows (Fig. 5.1.1.5):

– Complex A: chaotic, plastic, remoulded greyish to brown clay deposits, directly involved in the reactivations. Thickness: 6.70−11.20 m;

– Complex B: light- to dark grey clays, silty clays, sandy clays, silty sands. Thickness: 4−12 m;

– Complex C: calcareous levels. Thickness variable from dm to m;

– Complex D: dark grey, scaly marly clays, clayey marls and marls, which minimum depth is at between 15.30 and 20m from ground surface.

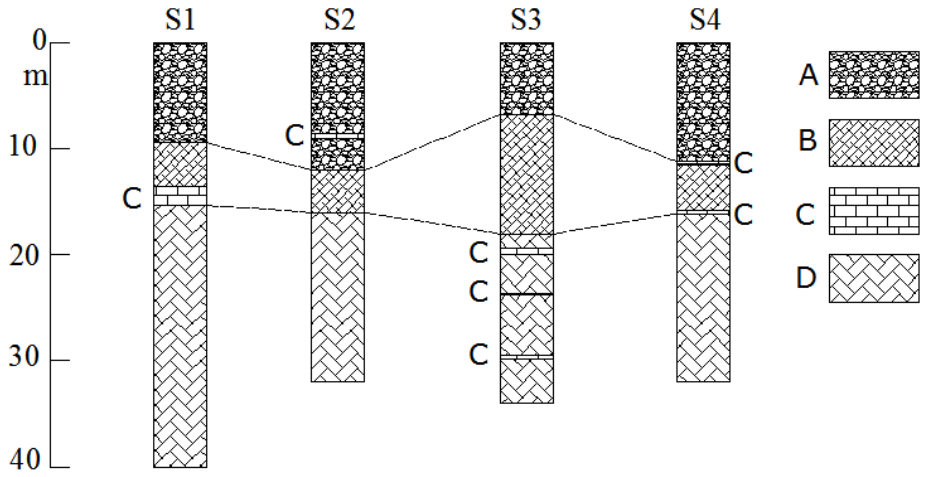

Figure 5.1.1.5. Lithological complexes recognized in the boreholes (Calcaterra et al., 2008).

As regards the relative position of the various complexes, A, B and D are usually found in such sequence from the ground surface downward, while C can be found interbedded with A, B and D. Complex C is represented by lithoid, highly permeable beds, and assumes a fundamental role with respect to groundwater circulation. Following the above litostratigraphical scheme, a cross section has been reconstructed (Fig. 5.1.1.6) where layers belonging to complex C are not visible due to the scale adopted.

The rotational character is shown in the source area by the steeply inclined main scarp and by the overall spoon-like shape. Due to strata attitude (which, even though with several folds and irregularities, mostly dips toward the east and the north-east) the slope movement evolves from rotational to translational slide and successively into an earth flow.

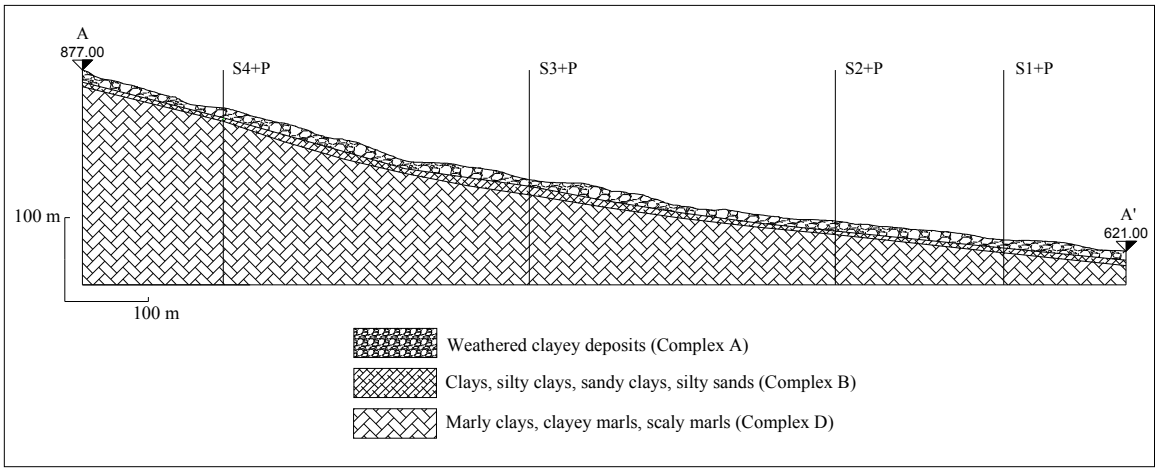

Figure 5.1.1.5. Geological cross-section (Calcaterra et al., 2008).

5.1.2 Processing results

5.1.2.1 ENVISAT images

Results of the interferometric processing of ENVISAT ASAR and last generation Cosmo-SkyMed images were compared. In particular for this site, thirty-five images (track 36 – frame 2763) acquired over descending orbits of the ENVISAT satellite systems, spanning the time interval from November 2002 until November 2008, have been processed. In order to apply the DInSAR technique, pairs of images characterized by small spatial and temporal baseline have been selected from the available dataset. Twenty-four interferograms (Figure 5.1.2.1.1) characterized by perpendicular baseline varying between 17 and 573 m have been processed. Temporal baseline varies between 35 and 210 days. The threshold for temporal baseline values allowed to minimize the error induced by temporal decorrelation, while for spatial baseline to reduce spatial decorrelation.

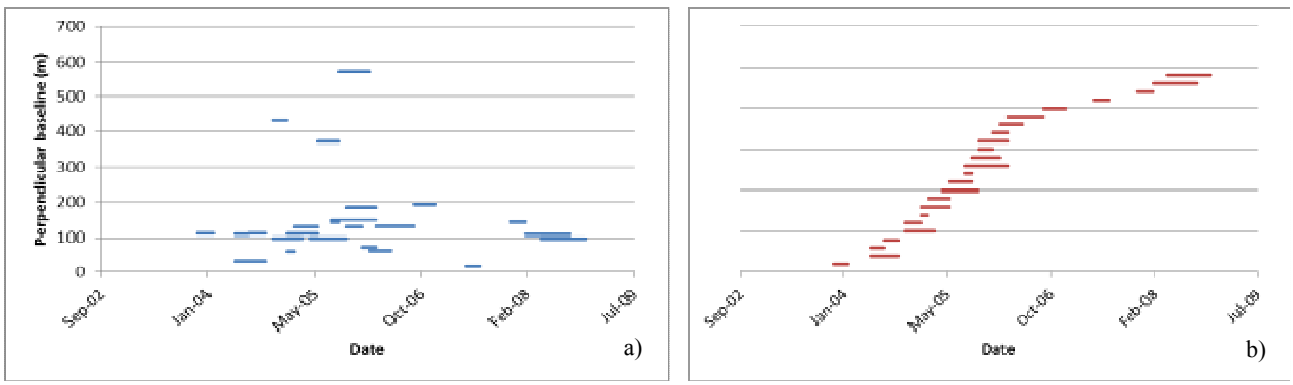

Figure 5.1.2.1.1 a) Interferograms' baseline (temporal and spatial), b) temporal distribution of the interferometric pairs.

The Figure 5.1.2.1.2 shows the mean coherence map of the landslide area. Four points (S1, S2, S3 e S4), corresponding to inclinometers positioned during a previous monitoring campaign, were identified inside the landslide area for subsequent comparison with last generation images.

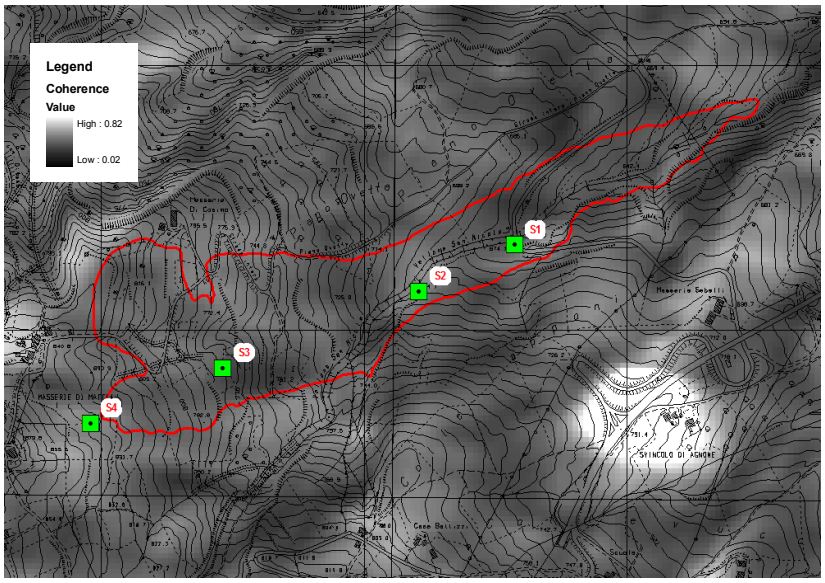

Figure 5.1.2.1.2. Coherence map from Envisat images with inclinometer location.

Coherence values inside the landslide (red line) are very low (Tab. 5.1.2.1.1), as the area is completely rural. Starting from mean coherence values calculated by means of an estimator, it was possible to evaluate the phase standard deviation ($\Delta\varphi$) which varies between 48° and 55° and corresponds to a displacement standard deviation of 0.5 cm. The next step would have been the elaboration of the velocity map. This was not achieved owing to the absence of points with significative coherence values.

Table 5.1.2.1.1. Mean coherence, phase ($\Delta\varphi$) and displacement (Δs_d) standard deviation.

Inclinometer	Mean coherence	$\Delta\varphi$[°]	Δs_d [cm]
S1	0.12	55	0.43
S2	0.14	48	0.38
S3	0.11	59	0.46
S4	0.14	48	0.38

5.1.2.2 Cosmo-SkyMed images

Cosmo images, as previously described, were acquired within the project related to the First Announcement of Opportunity Cosmo-SkyMed. The aim of the project was to verify the suitability of DInSAR technique using SAR Cosmo-SkyMed imaging in order to study the terrain deformation

due to landslides characterized by slow and intermittent movements. For this purpose 8 Trihedral Corners Reflector (TCR) with GPS antenna have been manufactured and installed (Figure 5.1.2.2.1), and a mobile GPS network has been set up in order to study the landslide activity and compare movements identified by means of interferometric technique (Figure 5.1.2.2.2). This kind of artificial reflector was chosen on the basis of scientific studies (Sarabandi et al., 1995, Xia et al., 2004, Ferretti et al, 2007, Doerry, 2008). TCRs were actually identified on the basis of evaluations of the Radar Cross Section (RCS), which is the parameter that mostly affects the visibility of such devices. As shown in Figure 5.1.2.2.3, their shape allows the optimization of such parameter and an easier installation, which, in turn, significantly affects the results in terms of visibility. Installation considered both geometry of images acquisition (incidence angle) and slope geometry (local slope), that play a relevant role in SAR acquisitions, as previously described in Chapter 4.

Eleven images were acquired over the February 2011 - January 2012 period (Table 5.1.2.2.1).

Figure 5.1.2.2.1. Corner reflector and GPS antenna.

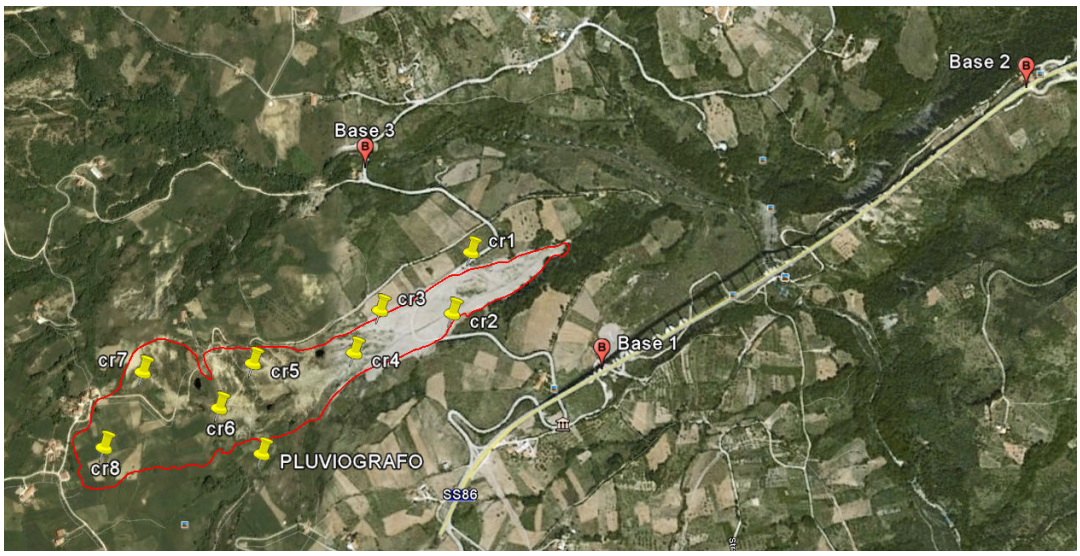

Figure 5.1.2.2.2. GPS network installed and corners reflector.

Table 5.1.2.2.1. List of Cosmo-SkyMed images for Agnone site.

BEAM	DATE	ACQUISITION ORBIT/LOOKSIDE
HI-01	24/02/2011	R/D
HI-01	29/04/2011	R/D
HI-01	31/05/2011	R/D
HI-01	18/07/2011	R/D
HI-01	19/08/2011	R/D
HI-01	22/10/2011	R/D
HI-01	07/11/2011	R/D
HI-01	25/12/2011	R/D
HI-01	10/01/2012	R/D
HI-01	26/01/2012	R/D
HI-01	11/02/2012	R/D

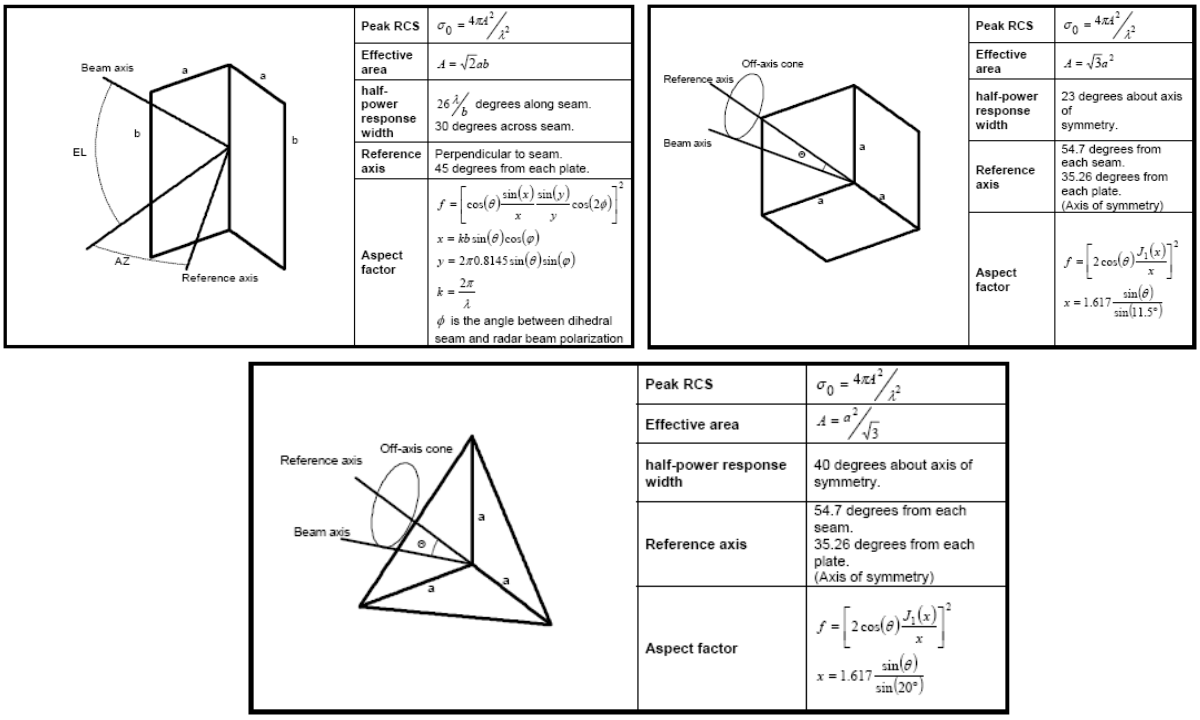

Figure 5.1.2.2.3. Formulas for RCS of Basic Elements.

Three GPS readings, respectively in February 2010, June 2011, and March 2012, were recorded during the interferometric images availability period. Processing demonstrated that the landslide is still active and shows different moving rates: 15 cm/year in the upper part, 2 cm/year in the middle part and 5 cm/year in the lower part (Fig. 5.1.2.2.5).

Ten out of eleven images in descending orbit have been used for the time interval February 2011 - January 2012; the last image was not considered as it showed low reflectivity values due to the presence of the snow during the acquisition (Fig. 5.1.2.2.6a and b).

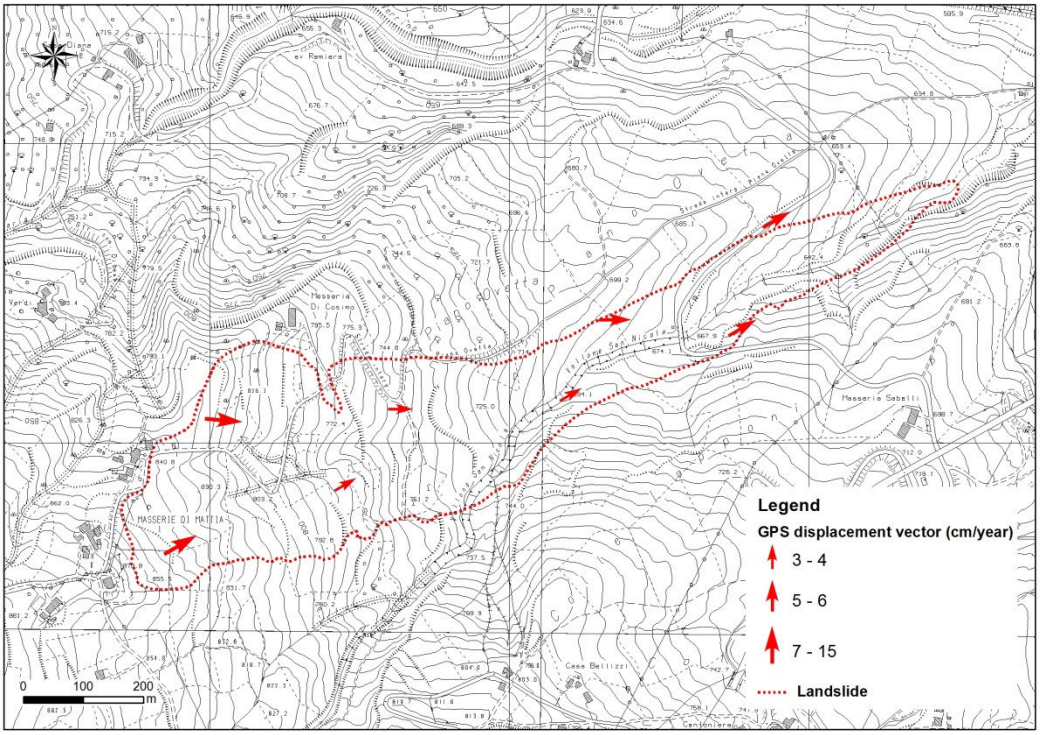

Figure 5.1.2.2.5. GPS network measures.

Co-registered images have been processed (Fig. 5.1.2.2.7), and all possible interferogram pairs (41) with spatial baseline lower than 1000 m have been individuated (Fig. 5.1.2.2.8). This threshold for spatial baseline values allowed to minimize the error induced by spatial decorrelation.

Figure 5.1.2.2.9 represents the mean coherence map; coherence values of the corner

installations appear to be quite high. Mean coherence values have then been calculated, showing lower displacement standard deviation values than those obtained from ENVISAT processing (Table 5.1.2.2.2).

The last step to complete the entire DInSAR processing would have been the elaboration of the deformation map, in terms of mean velocity map and time series of deformation. Due to the limited number of available images, the velocity map showed few unconnected points which gave rise to a considerable amount of noise.

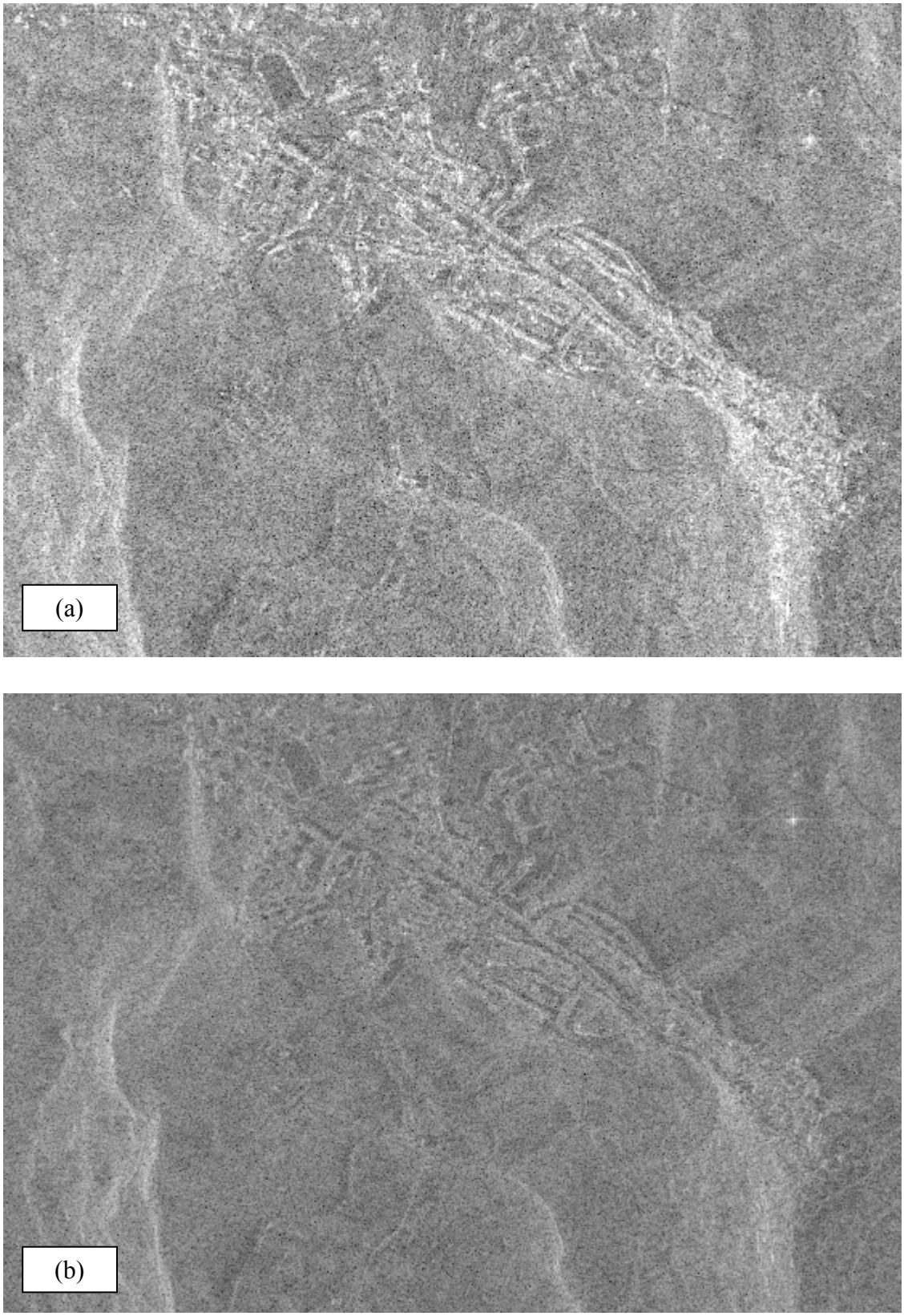

Figure 5.1.2.2.6. Comparison between two different acquisition 24/2/2011 (a) and 11/2/2012 (b) in which is shown the different reflectivity caused by the presence of the snow.

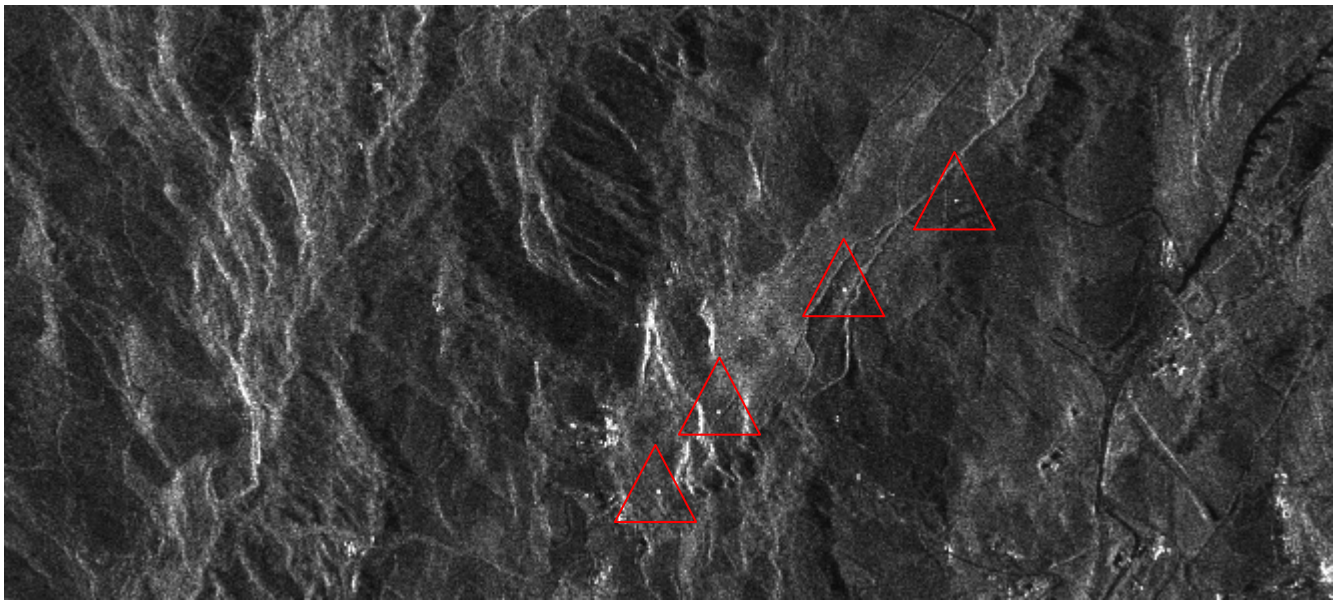

Figure 5.1.2.2.7. Co-registered image and corners reflector.

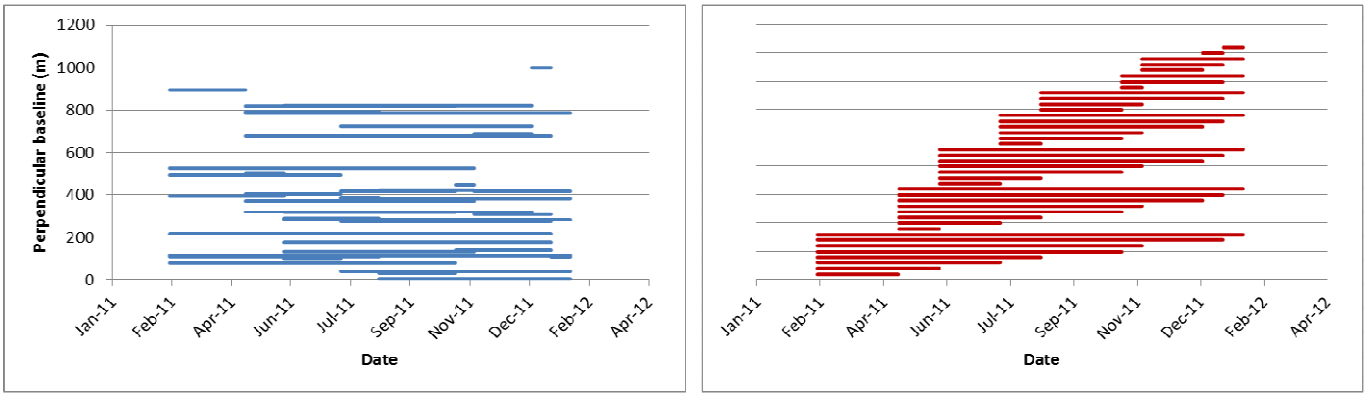

Figure 5.1.2.2.8. Interferograms with Cosmo-SkyMed images.

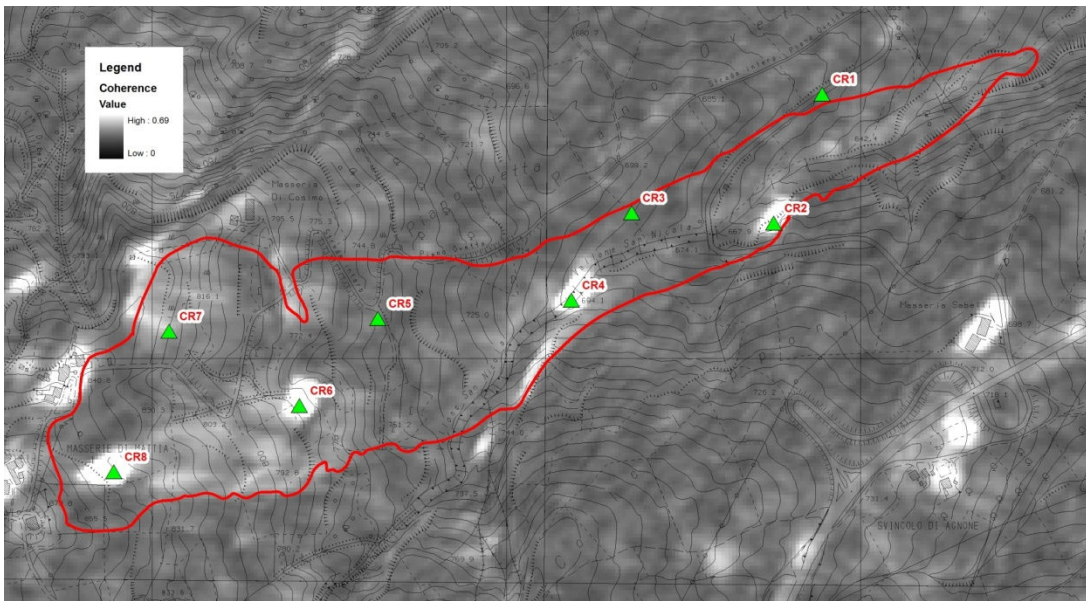

Figure 5.1.2.2.9. Mean Coherence map and corner position.

Table 5.1.2.2.2 Mean coherence, phase ($\Delta\varphi$) and displacement (Δs_d) standard deviation for Cosmo SkyMed images processing and ENVISAT images processing.

Corner reflector	Envisat (ML 20x4)	Cosmo SKy-Med (ML 4x4)
CR2	0.14	0.88
CR4	0.14	0.85
CR6	0.12	0.88
CR8	0.15	0.87
$\Delta\varphi$	**50°**	**10°**
$\Delta\sigma$	**± 4.0 mm**	**± 0.5 mm**

5.2 Costa della Gaveta (Potenza)

5.2.1 Geological settings and landslides

In this test site two landslides (Costa della Gaveta and Varco d'Izzo) occurred on the slope of a hill facing the valley of the Basento river (Fig. 5.2.1.1), East of the town of Potenza, in Southern Italy (Fig. 5.2.1.2) have been investigated. Several geological and geomorphological studies have been carried out in the last 30 years (Guida et al. 1988; Perrone et al. 2004; Del Prete and Del Prete 2009; Di Maio et al. 2010).

Figure 5.2.1.1. Costa della Gaveta hill.

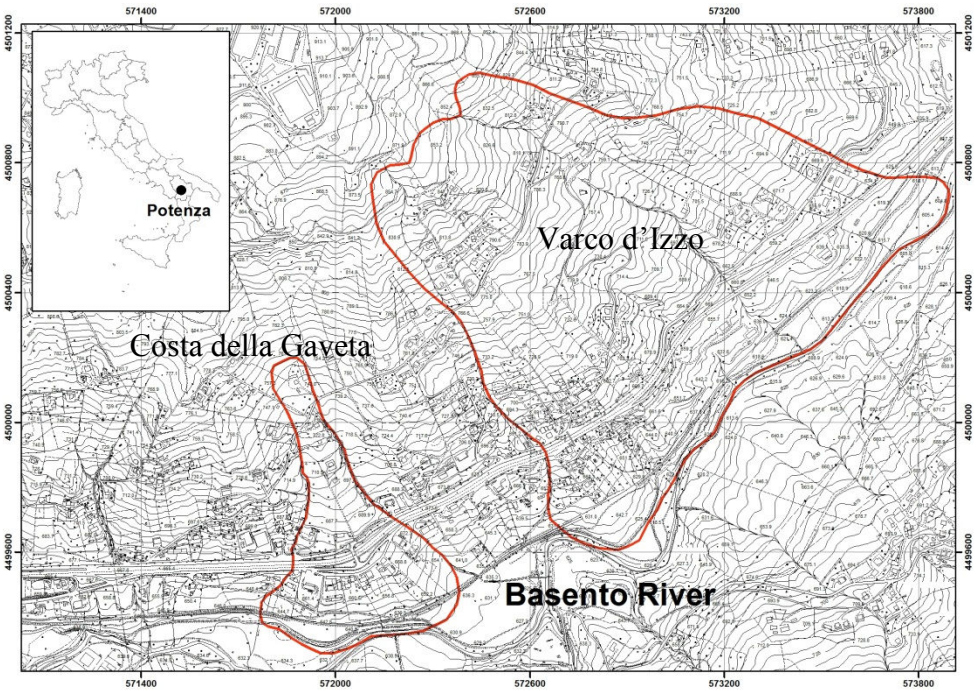

Figure 5.2.1.2. Study area

The landslides, as described by Di Maio et al., 2010 (Fig. 5.2.1.3), which exhibit similar geometric and kinematic features, occur in the geological formation of the Varicoloured Clays (Middle Cretaceous–Oligocene), constituted by tectonized, fissured and heterogeneous clay shales, clay and mudstones, including blocks and layers of marls, calcarenites and limestones (Pescatore et al. 1999). They can be described as ancient and complex roto-translational slides evolving into earth

slides according to the classification of Cruden and Varnes, 1996. The slow movements of the landslides cause severe damage to houses and infrastructures. In particular, the highway and the railway, whose tunnel crosses one of the accumulation zones, need frequent maintenance and strengthening, besides continuous monitoring (by extensometers, inclinometers and topographic measurements), with notice able social cost.

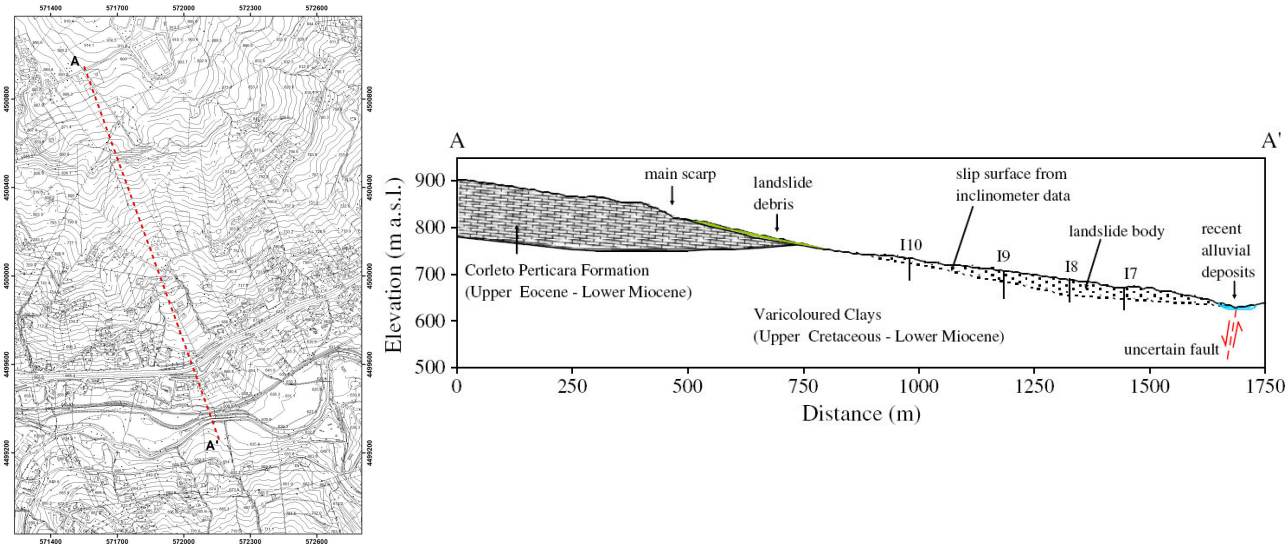

Figure 5.2.1.3. Geomorphological section (Di Maio et al., 2010)

In order to study and to monitor the landslides, an integrated monitoring system composed by measuring devices of rain, pore pressures (Casagrande piezometers, electrical piezometers), deep (inclinometers) and surface (GPS) displacements has been installed. So as to understand the phenomena and eventually to give warnings to the population for disaster prevision (Calcaterra S. et al. 2008). From the experimental data, some important features of the landslides have been understood. Costa della Gaveta landslide has been studied by Di Maio et al. (2010). It was understood to be an earth slide, whose displacements can be considered uniform (Calcaterra S. et al., 2010). The displacement rate (Fig. 5.2.1.4) decreases from upslope to downslope, probably

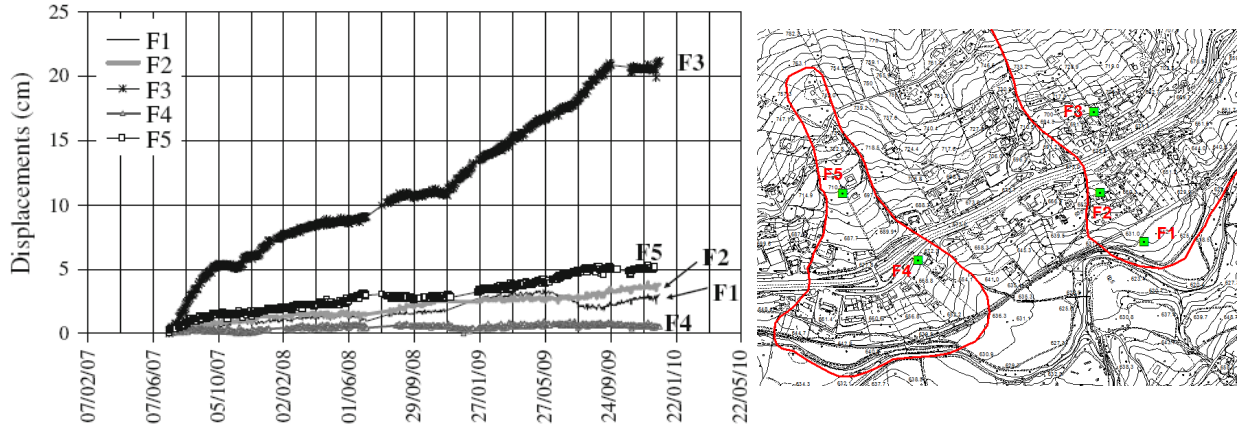

Figure 5.2.1.3. GPS displacements (Calcaterra S. et al., 2010)

because of the increase in the areas of transversal sections, the ‘‘soil discharge’’ being practically constant. The Varco d’Izzo landslide has been analyzed by Del Prete and Del Prete (2009), which mapped only only a small portion of a much larger and complex landslide.

5.2.2 Results

For this site ENVISAT images were processed. The results were then compared with ancillary data obtained during the same period by traditional monitoring campaigns. Twenty-four ENVISAT images (Track 086 Frame 798) in *ascending* orbit over the period 01/28/2007 through 07/11/2010 underwent the entire elaboration process in order to produce the velocity map and the deformation time series.

The first step was to register the images needed to elaborate the Amplitude map represented in figure 5.2.2.1.

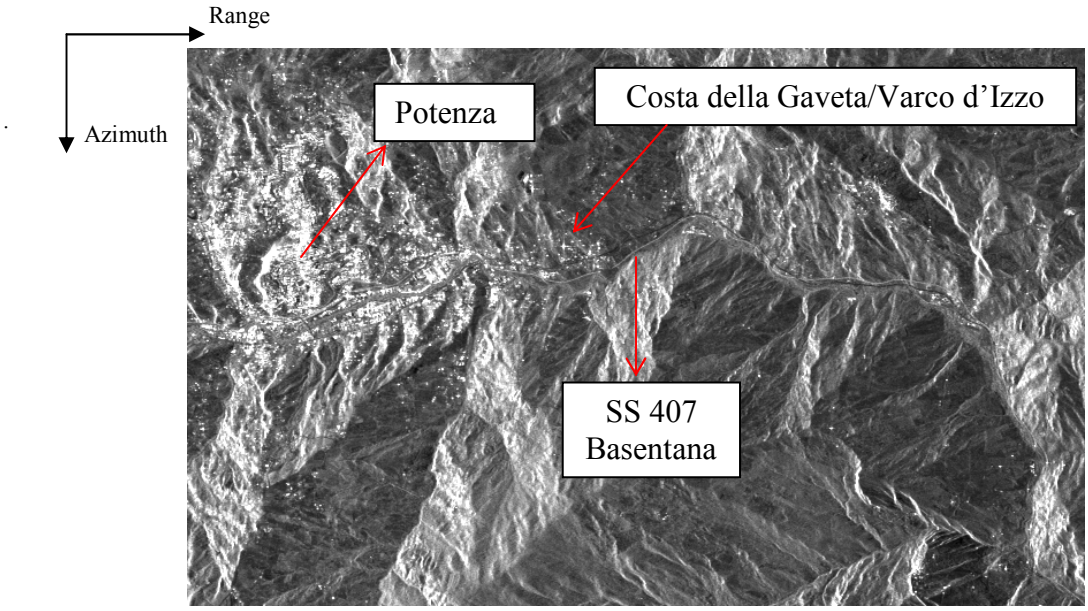

Figure 5.2.2.1. Amplitude map of the study area.

Potenza city (white area) and the SS 407 Basentana road can be clearly seen on the left hand side.
In order to reduce decorrelation, the next step was to identify interferometric pairs with sufficiently low spatial and temporal baseline values. The following limits were set: 250 m and 211 days, respectively. In this way, sixty interferograms were generated (Fig. 5.2.2.2).

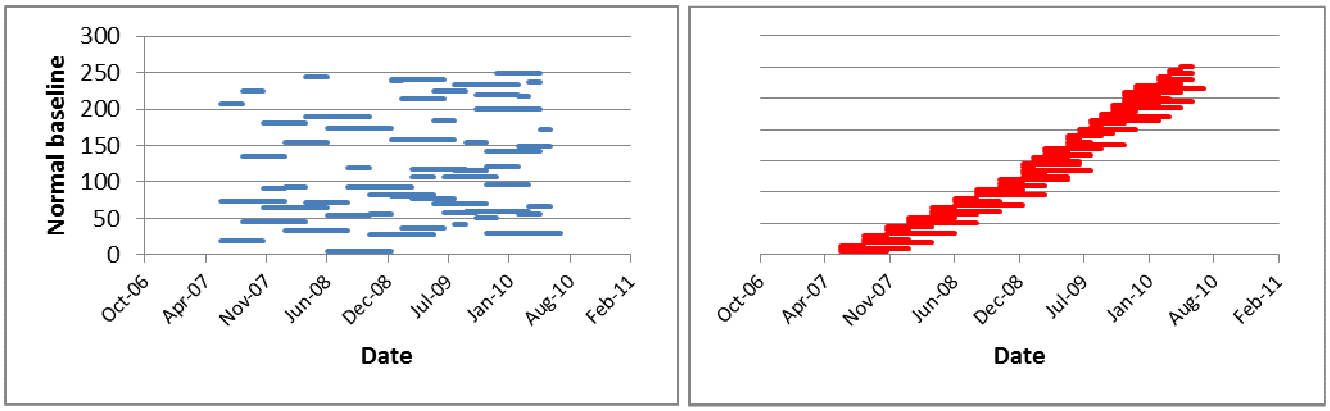

Figure 5.2.2.2. Interferograms and perpendicular baselines.

The mean coherence map, which allows to evaluate the reliability of the derived measurements, was then elaborated (Fig. 5.2.2.3). In order to identify the points to use for further analyses, a 0.4 coherence threshold was set. This value allows to obtain a phase standard deviation equal to 15°, using a 15x3 multilook.

Finally, the mean velocities map (along the LOS) was developed (Figure 5.2.2.4) after identifying a stable point (Water Purification Plant of Acquedotto Pugliese located in Masseria Romaniello).

It is worth mentioning that mean velocities were estimated for a few points inside the mapped landslide perimeter because of the images' low resolution and of low number of natural reflectors in the considered area.

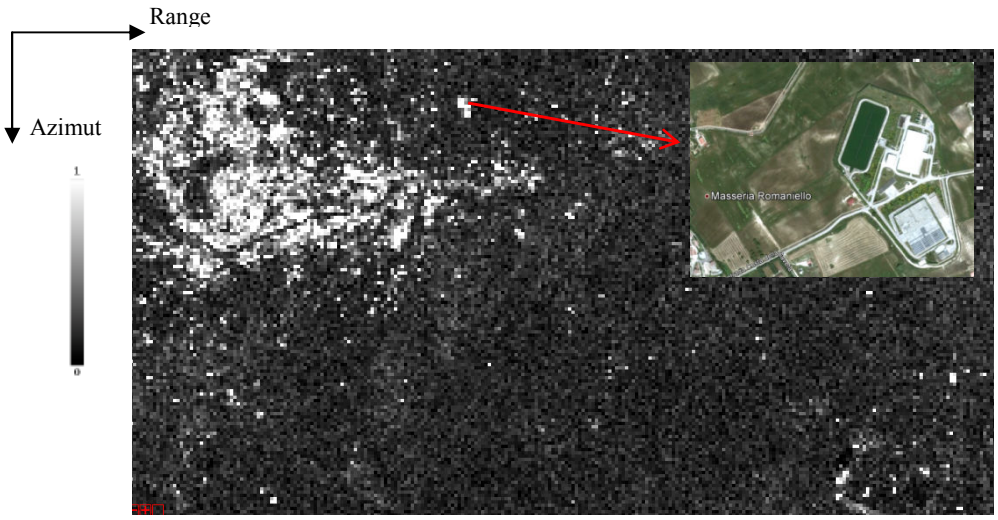

Figure 5.2.2.3. Mean coherence map.

As far as the Costa della Gaveta landslide concerns, accordingly with GPS measurements, decreasing rate of velocity have been detected from upslope (I10 inclinometer) to downslope (SS 407 Basentana road). It is worth pointing out that even on the western side (outside of the landslide

scar) mean velocity of displacements higher than 5 mm/year have been detected, probably due to the widening of the phenomenon. On the other hand, for Varco d'Izzo landslide, only in correspondence of the GPS points (F2 and F3) high velocity values have been encountered, while the slope is substantially stable.

Location of instruments (GPS points and inclinometric tubes) placed during previous *in situ* geognostic campaigns are also shown in the Fig. 5.2.2.4.

Among such instruments there is a GPS station network which was installed in 2006 by the Italian Geological Service (Calcaterra S. et al., 2010) in order to monitor some relevant structures.

This network consists of 13 fixed stations, integral with stable constructions or with purpose-made pillars, both built inside the studied terrain. A similar station was placed near the Masseria

Romaniello Water Purification Plant, which is believed to be a landslides-unaffected area. Fixed stations allow continuous measurement of superficial displacements by remote acquisition (Fig. 5.2.2.5).

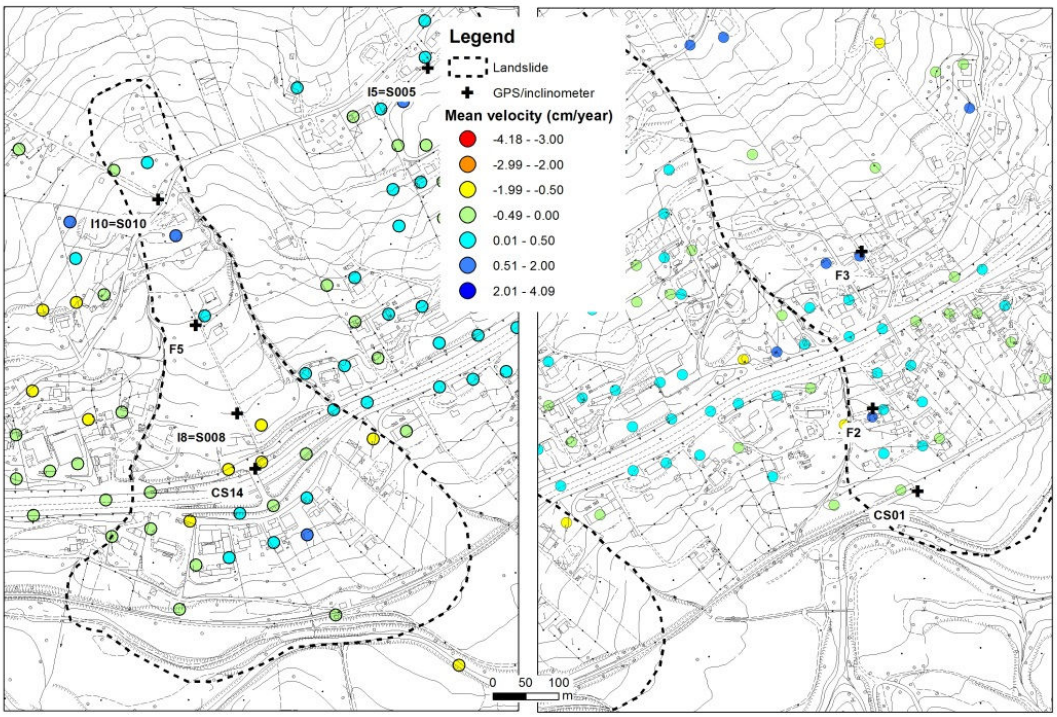

Figure 5.2.2.4. LOS velocity maps of Costa della Gaveta (left) and Varco d'Izzo (right) landslides for the January 2007-July 2010 period.

Analyses of topographic data, geomorphologic evidence and inclinometric measurements allowed to identify the landslide's geometric and kynematic characteristics and to calculate the superficial displacement velocities values, which were then compared with satellite data. Ground-registered velocities proved to be ten-fold higher than the interferometric ones (for instance, 1.6 cm/year for the F2 point and 2.0 cm/year for the F5 point vs. approximately 0.47 e 0.37 cm/year,

Figure 5.2.2.5. Examples of GPS installations.

respectively). It must be taken into account that satellite-registered velocities are referred to the sensor-target connecting line (LOS – Line of Sight), which is oriented West-East. Therefore, in order to compare ground (GPS) and interferometric measures, it was necessary to elaborate a map, shown in Figure 5.2.2.6, which allowed to estimate the percentage of real movement that the

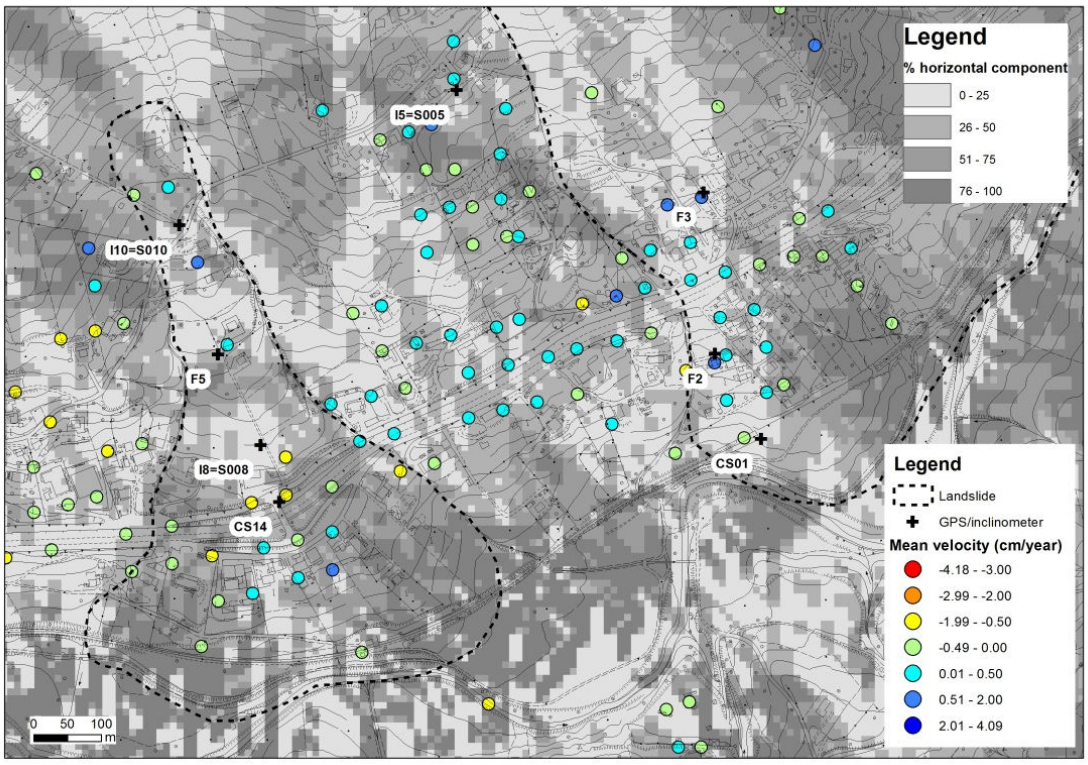

Figure 5.2.2.6. Real movement percentage map, calculated on the basis of the acquisition and site's geometries. The arrows show the directions of the horizontal components of the velocity vector along the LOS.

satellite is able to identify in relation to the acquisition geometry and to the site's topographic characteristics (Plank et al., 2012).

Table 5.2.2.1 compares the mean velocities for eight reference points; for six of them there appears to be a fairly good agreement between the two monitoring techniques.

For example considering the F5 point, located inside the Costa della Gaveta landslide, the estimated velocity magnitude was 1.8 cm/year by GPS measurements and 0.47 cm/year along the LOS with satellite data elaborations.

The latter value, owing to the acquisition geometry and to the site's topographic characteristics, accounts for approximately 30% of the real movement and so, after adjustments, turns out to be 1.6 cm/year. In the same way, considering the F3 point, located inside the Varco d'Izzo landslide, the estimated velocity magnitude was 10 cm/year and 1 cm/year by GPS and satellite measurements, respectively. After adjusting for a 12% of real movement on the basis of acquisition geometry and of the site's topography, satellite obtained measurement corresponds to 8.3 cm/year.

Table 5.2.2.1. Comparison between ground and interferometric measurements.

Costa della Gaveta	**Velocity (cm/year)**			
	GPS	SAR	%	Total
I10	3.60	0.56	15	3.70
F5	1.80	0.47	30	1.60
CS14	0.72	-0.57	55	1.00
I8	0.98	-1.25	40	3.10
Varco d'Izzo	**Velocity (cm/year)**			
F3	10.00	1.00	12	8.30
F2	1.30	0.37	20	1.80
CS01	0.84	-0.34	20	1.70
I5	1.30	0.37	38	1.00

It is worth pointing out that recently a specific project for the acquisition of high resolution Cosmo-SkyMed images for this site has been signed with Italian Spatial Agency. Figure 5.2.2.7 shows the comparison between ENVISAT and Cosmo-SkyMed images referred to Costa della Gaveta test site; it is possible to highlight the wide zones characterized by bright pixels in the ENVISAT scene that represent areas affected by strong geometrical distorsions (foreshortening, layover and shadowing effects). In such areas, as described in Chapter 4, no useful points for interferometric processing have been identified. For this reason, these areas were not monitored. The causes of such distorsions may be identified in both the low resolution of ENVISAT images and, most of all, the incidence angle used for the images' acquisition, which is known to be fixed

and equal to 23° for ENVISAT. On the contrary, last generation satellites can vary such angle between 20° and 50°. This, together with their higher resolution, allows to obtain superior quality images. Actually, the opportunity to set the incidence angle optimizes the images' quality also in relation to the site's morphology. An example is shown in Figure 5.2.2.8, in which layover and foreshortening maps from ENVISAT (incident angle 23°) and Cosmo-SkyMed (incident angle 37°) acquisitions and processed according to the algorithm described by Notti et al. (2010) are compared.

In order to apply this algorithm a geographical information system (GIS) procedure has been implemented. The procedure consists in a routine developed in Model Builder (Fig. 5.2.2.9) that allows to predict the areas in which layover and foreshortening will occur.

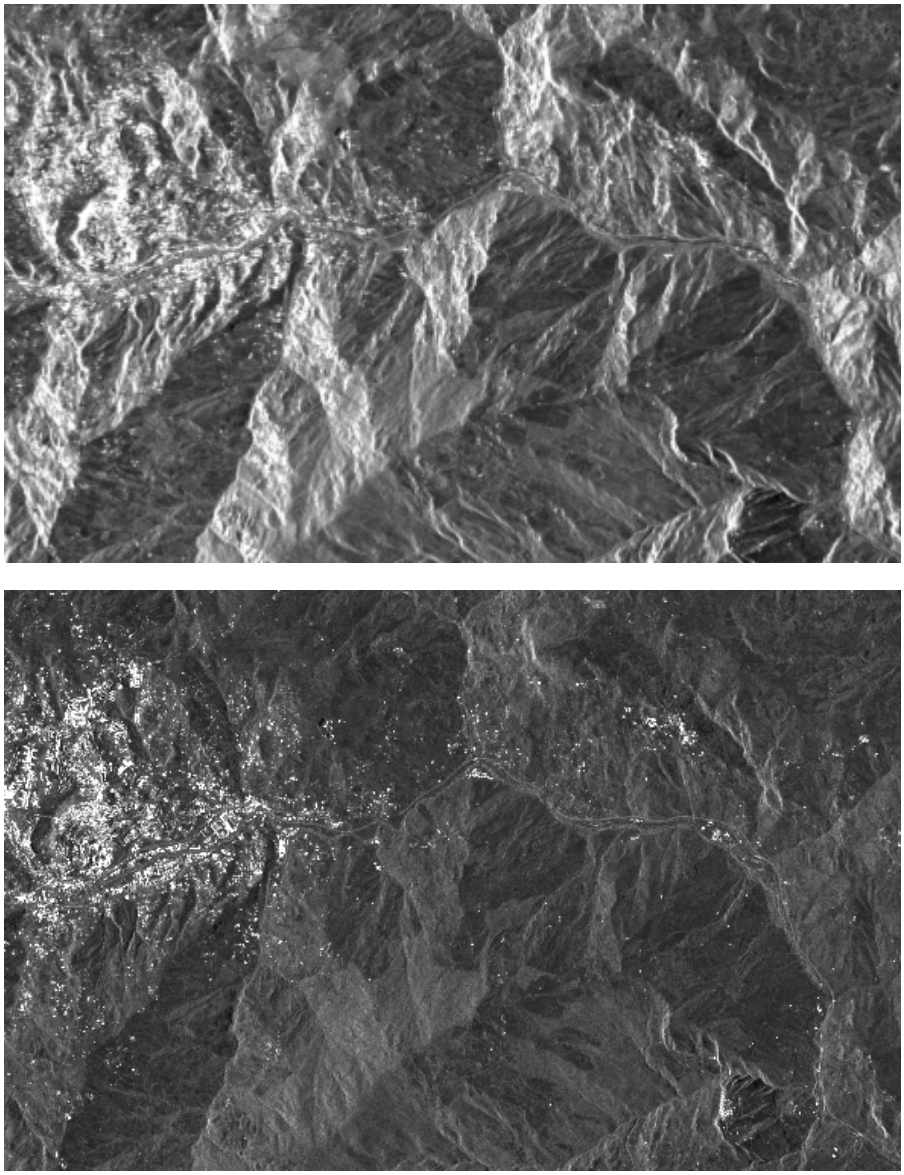

Figure 5.2.2.7. ENVISAT amplitude image (above), Cosmo Sky-Med amplitude image (below)

Starting from the geometry of the ground surface (slope and aspect models obtained from a DEM) and acquisition geometry of the radar (incident angle and the angle from north of the satellite track) is possible to perform in a semi-automatic way the R_{index}:

$$R_{index} = -\sin(\arctan(\tan(S) * \sin(A\alpha)) - \theta)$$

where S is the slope, Aα is the aspect correct with angle from north of the satellite track and θ is incident angle of LOS.

Such parameter is an index that can vary from negative values to 1. The negative and lower values (<0.3) represent the zones affected by layover and foreshortening effects, larger values indicate slopes that are averse to the radar LOS, and therefore good oriented.

Finally, in the area affected by landslide phenomena, a comparison between percentage of measurability of movement maps for ENVISAT- and Cosmo-SkyMed-acquired images (Fig. 5.2.2.10) was made. As already observed for layover and foreshortening maps, last generation images processing increases the measurability of movement percentage inside landslide areas, thus allowing to estimate the possible deformation more precisely.

It is worth pointing out that the increase of such value is not related to a better visibility in terms of scatterers covering; anyway, such limit could be overcome by means of artificial scatterers installation.

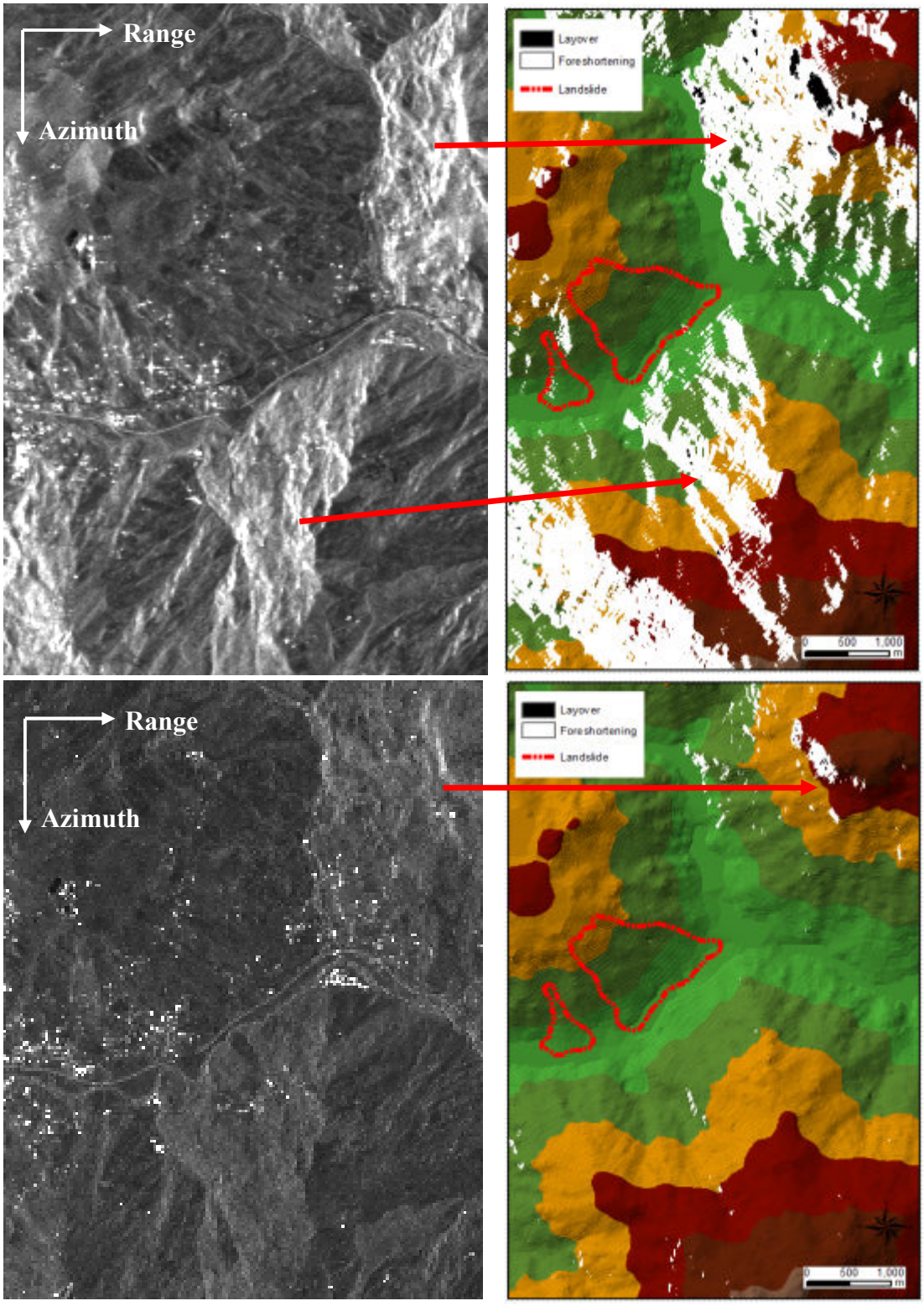

Figure 5.2.2.8 Comparison between ENVISAT and Cosmo-SkyMed layover and foreshortening maps.

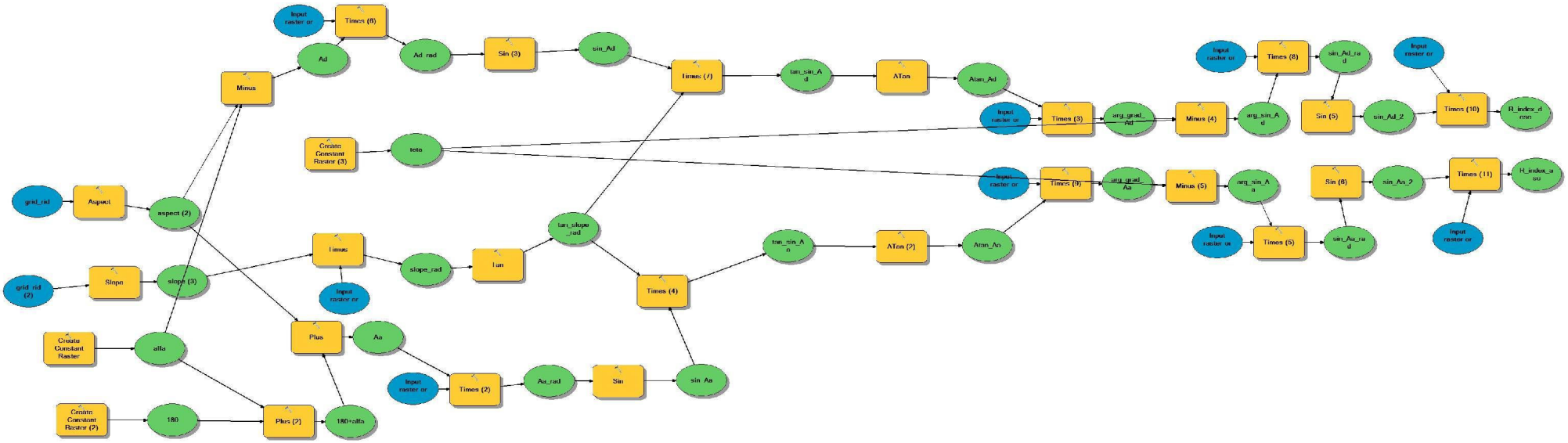

Figure 5.2.2.9. Model to perform the R-Index

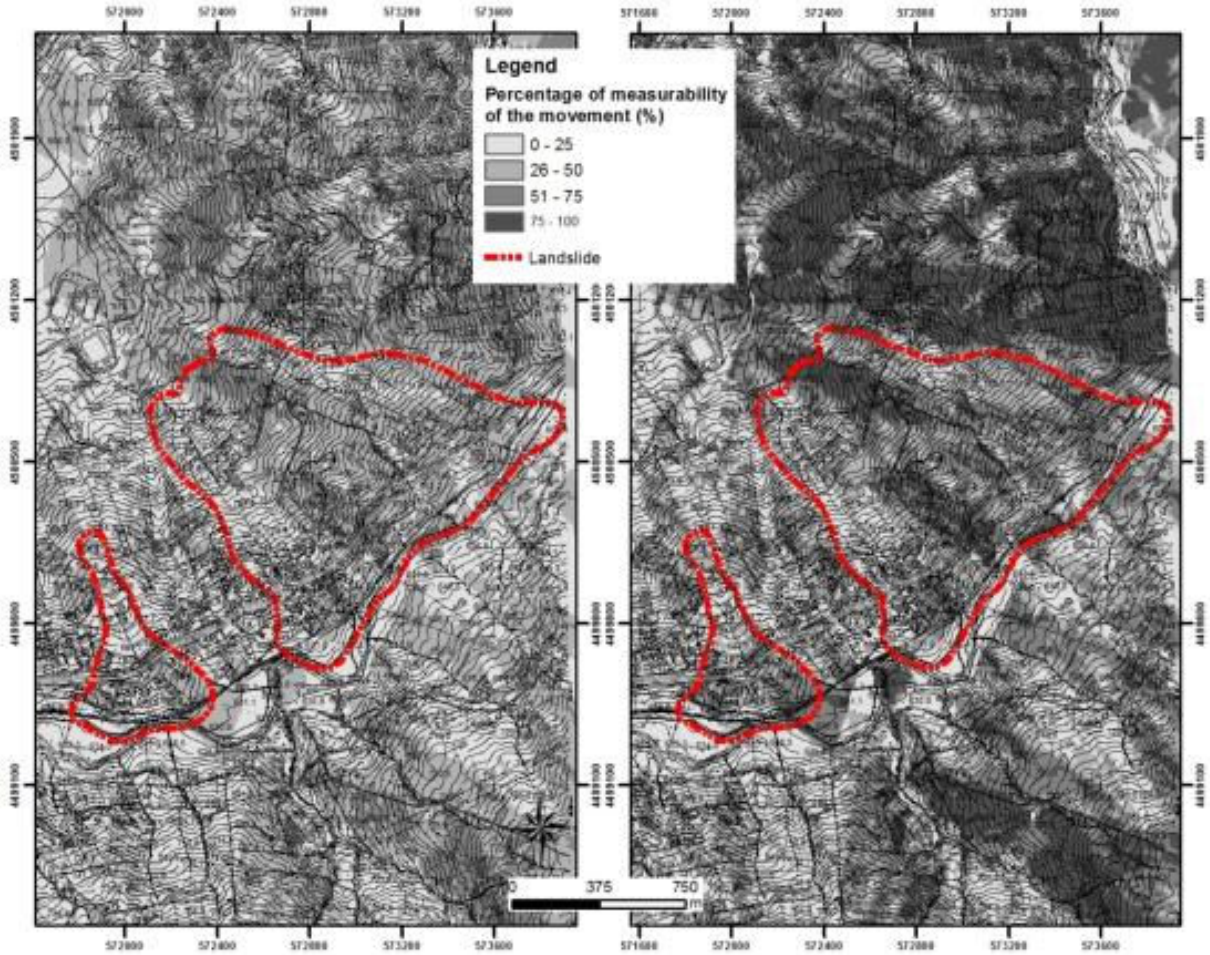

Figure 5.2.2.10. Comparison between percentage of measurability of the movement performed by: ENVISAT (left), Cosmo-SkyMed (right).

5.3 Moio della Civitella (Salerno)

5.3.1 Geological settings and landslides

The Moio della Civitella test site, located in the Cilento and Vallo di Diano National Park (Salerno province), was selected among the urban centres presenting higher values of PS density and velocity in Campania. At the same time, the different types of landslides affecting the area, and their interaction with the anthropogenic structures and infrastructures (as demonstrated by the observed damage to buildings), make the village one of the most interesting with respect to the analysis of the landslide hazard and mitigation of the related risk.

Moio della Civitella, whose first settlement dates back to VI÷IV century BC, is a small village of some 1700 inhabitants and is composed of two urban centres, Moio and Pellare (Fig. 5.3.1.1).

Figure 5.3.1.1. Moio della Civitella town.

The area is geologically characterized by the presence of the Crete Nere-Saraceno Fmn. (Bonardi et al. 1988), a structurally complex formation (Fig. 5.3.1.2), Cenozoic in age, belonging to the North Calabrian Unit. The formation is mainly made up of argillites with intercalated carbonate and silicoclastic arenites, often weathered at the outcrop. In the study area, this terrain, showing the typical features of the highly tectonized rocks of the southern Italian Apennines (diffuse and pervasive tectonic discontinuities, intense fracturing, extremely variable bedding, etc.) is overlain by a Quaternary cover consisting of heterogeneous debris in a silty-clayey matrix. The differences in lithology, and in the hydrogeological behaviour of the terrains as well, are among the main factors predisposing instability at Moio della Civitella. The area, characterized by hilly morphologies with low-gradient slopes at elevations between 600 and 200 m a.s.l., is intensely affected by erosional and gravitational processes. Among them, landslides occupy a top-rank

position, as it is well demonstrated by Figure 5.3.1.3. Such map is an extract from the IFFI project (Inventory of Landslides in Italy) a national project dedicated to landslide inventory and mapping in Italy (Amanti et al. 2001).

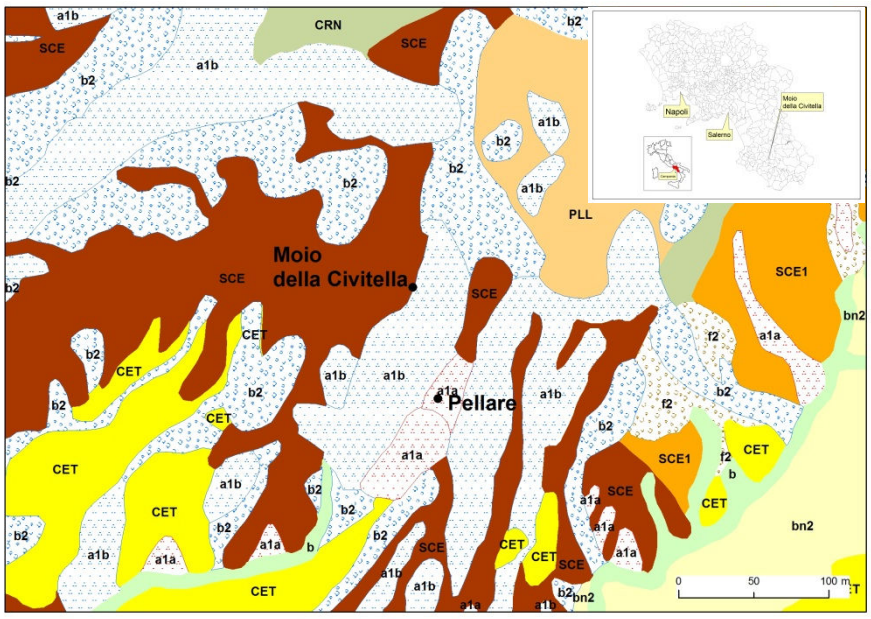

Figure 5.3.1.2. Geological scheme of the Moio della Civitella area (APAT 2006 – redrawn).

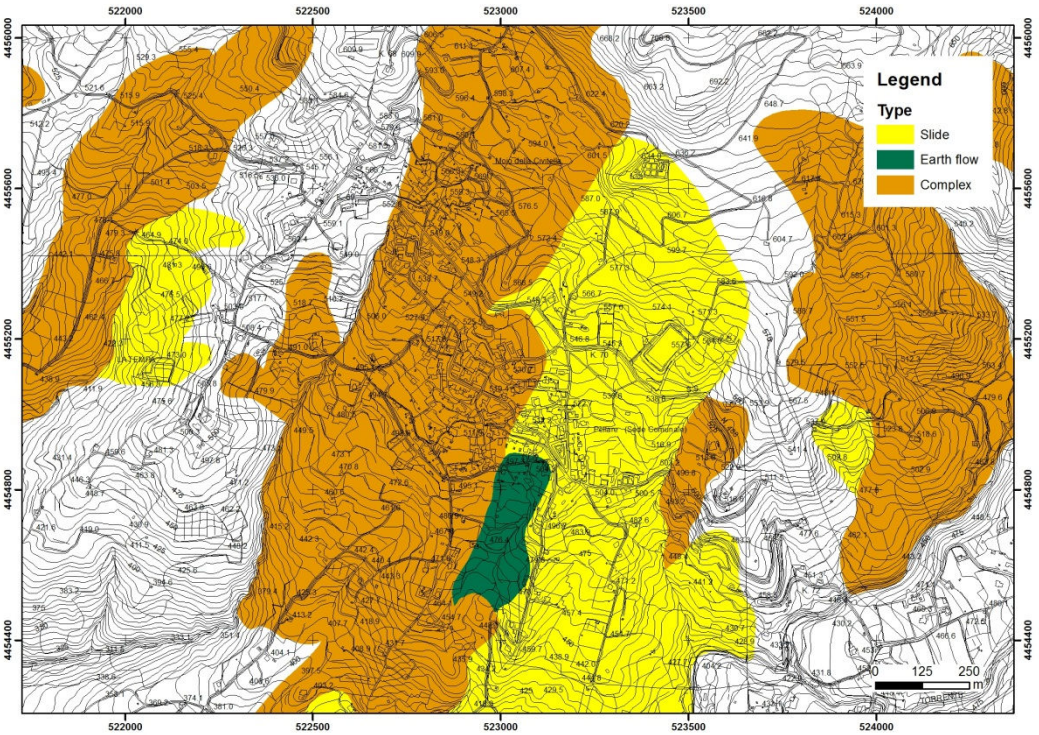

Figure 5.3.1.3. Landslide inventory map (IFFI project).

Following the Cruden & Varnes (1996) classification, the prevailing typologies are complex landslides and rotational slides evolving to translational slides. The main slope movements derive from ancient phenomena which have involved large portions of the slopes, if not their whole extension. This is also the case for the landslides that directly affect the urban centres. As common in many similar settings of the southern Italian Apennines, the rotational component of the complex slope movements is generally limited to the source areas, whilst most of the landslide body consists of the flow component, which may reach overall lengths on the order of several hundreds of metres. Multiple, or superimposed, phenomena are also frequent. As regards state of activity, landslides are generally dormant, whilst rainfall-triggered reactivations are common during the rainy seasons, generally involving limited parts of the landslides. As shown in the landslide map, the largest slope movements directly involve the inhabited areas, the lifelines and the main communication routes.

A detailed geomorphological mapping is currently being carried out, aimed at updating the available landslide inventory map, and at creating the morphological database information necessary for the ongoing monitoring campaigns. On the basis of the preliminary field surveys and interpretation of past monitoring data (boreholes, inclinometers, piezometers), the following elements have to be re-marked:

- below the topsoil horizon, an almost continuous debris cover is present, about 3 to 25 m thick, made up of arenaceous and conglomeratic blocks in a silty-clayey matrix;
- between the debris cover and the Crete Nere-Saraceno Fmn., a clayey horizon deriving from the weathering of the bedrock can be found, whose thickness varies from 0.5 to 5 m;
- the available piezometers revealed groundwater levels regularly hosted by the debris cover, located very close to the ground surface (depth < 5 m);
- with the exception of some minor reactivations, the main slope movements seem to be dormant at the present.

5.3.2 Traditional monitoring

Moio della Civitella territory, and, more in detail, the two urban centers of Pellare and Moio, have been thoroughly investigated with a topographic measure points and inclinometers network in order to study superficial and sub-superficial movements (Calcaterra et al., 2008, Calò, et al., 2012).

Seven inclinometric columns were progressively installed (Figure 5.3.2.1), with depths ranging between 7.5 and 13 m; four of them (I1, I2, I3 and I4) provided measurements for the 2007-2009 period, while the most recent ones (I5, I6 e I7) were used between years 2008 and 2009. Measurements' characteristics are shown in Table 5.3.2.1.

Limited superficial displacements of 1,6 cm were identified by I1 inclinometer over the April 2007-March 2009 time span (Figure 5.3.2.2), while the deep measurements clearly indicate the presence of an active slip surface located at depth of about 4 m. Inclinometers I5 e I6 registered equal and more extended superficial displacements (2,7 cm) and show active shear surfaces, respectively, at depth of about 3 and 10 meters. As far as the I4 concerns, have been measured only millimetric movements, confirming the present inactivity of the large slope movement.

Displacements occurred in the S-SW direction, in agreement with the terrain's morphology. Finally, measurements from the I2 and I7 inclinometers were excluded as they proved to be unreliable, probably because of a wrong installation procedure.

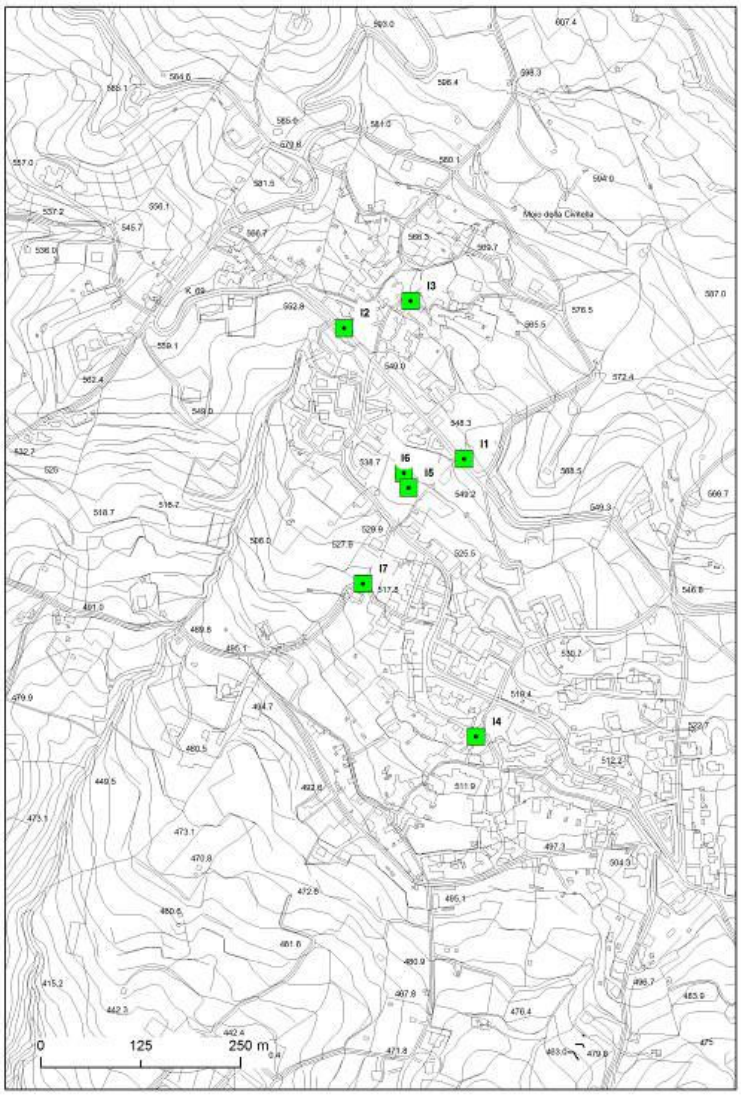

Figure 5.3.2.1. Inclinometers' position in Moio della Civitella

As reported in Calò 2009, the nearby location of the boreholes I5 and I6, there is a clear difference in the depth of the shear surface in the inclinometer readings: at I5, a shear surface is located at 3-3.5 m, whilst, on the other hand, readings at I6 indicate a more developed shear surface

at 9.5 m. This may be explained by the limited depth (8.5 m) of the borehole I5, that thus does not allow to detect the deep shear surface (at 9.5 m).

Table5.3.2.1.Characteristics of inclinometric measurements

Inclinometer	Depth (m)	Reference measure	Readings	Position
I1	11	April 2007	6	Moio
I2	13	April 2007	4	Moio
I3	12	April 2007	5	Moio
I4	7,5	April 2007	3	Pellare
I5	8,5	January 2008	2	Pellare
I6	10,5	January 2008	2	Pellare
I7	7,5	January 2008	2	Pellare

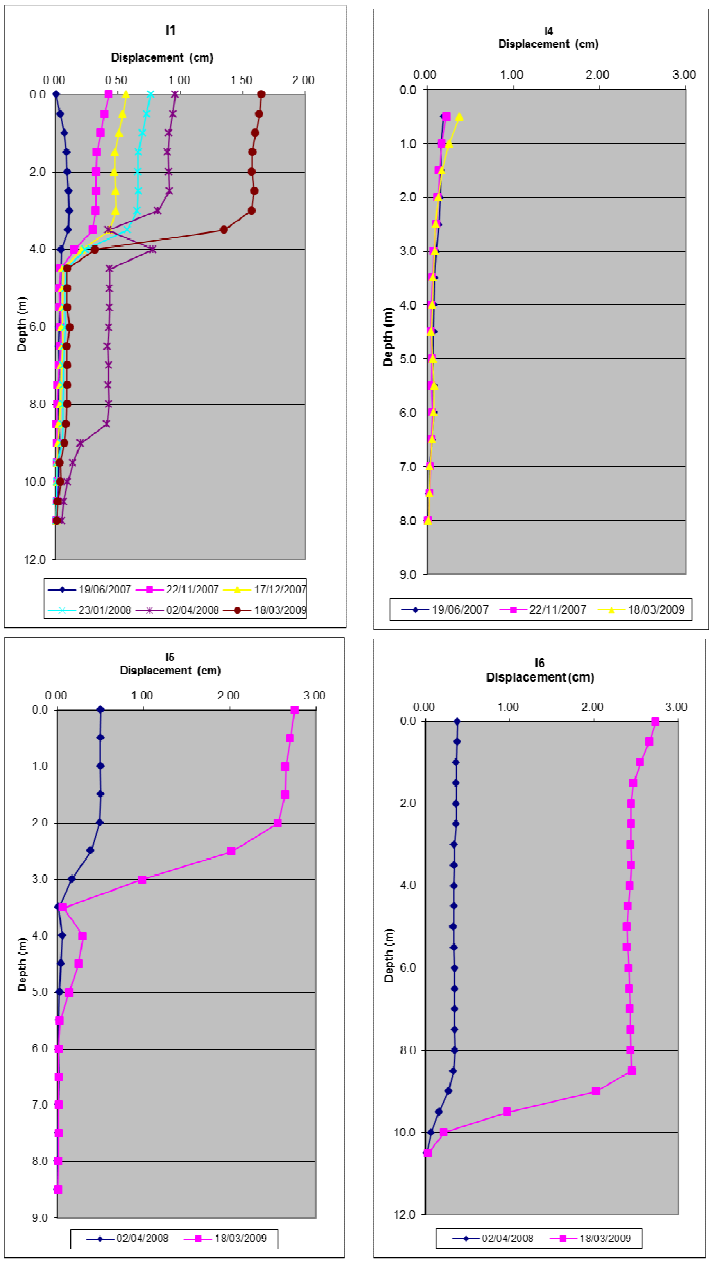

Figure 5.3.2.2. Inclinometric measurements.

As mentioned in Calò 2009, starting from year 2007, a topographic measure points network was installed (Figure 5.3.2.2). Before installation, several *in situ* campaigns were carried out in order to identify the most appropriate positions to measure possible instabilities and, at the same time, to evaluate their reciprocate visibility.

The final network was composed of 73 measure points, divided between the two urban centers and installed on man-built structures (buildings and road system); three control stations has been used as reference benchmarks for the measurement of the whole network.

The survey was conducted using a Total Station, that allows to reach very accurate results: angles were measured with a precision of 1" while distances were measured with a standard mode, with a precision of 1 mm + 1.5 ppm. Depending on weather conditions (temperature, humidity and pressure), that influence the resulted accuracy, the adopted instrument allows measurements on very long distances, up to 3 km.

Four measures were registered for Moio starting from June 2007, while Pellare was monitored staring from December of the same year. No significant displacements were identified and movements' values were of approximately 1 mm over the March 2008-March 2009 period.

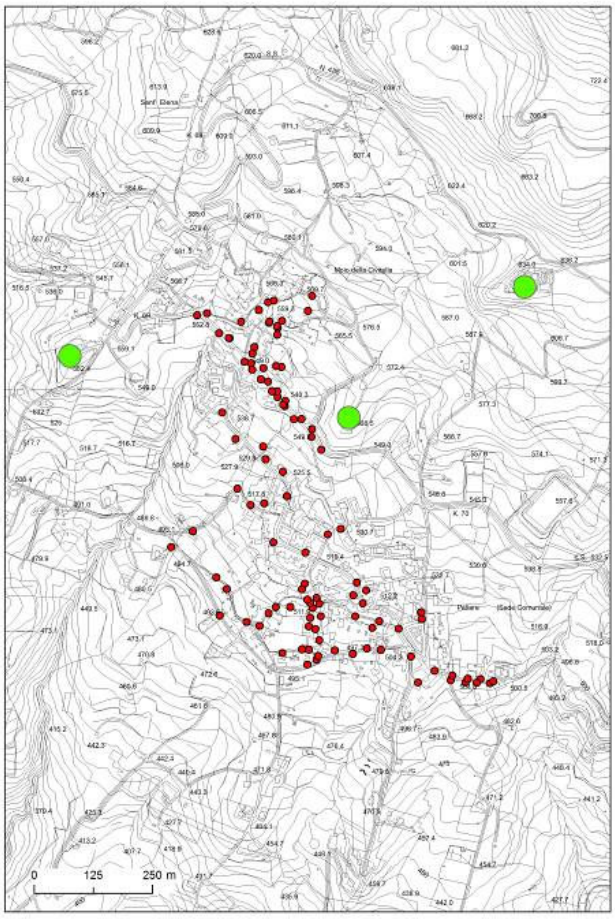

Figure 5.3.2.2. Topographic network; control points (green).

5.3.3 GPS monitoring

In addition to the traditional monitoring techniques previously described, a continuous acquisition GPS network composed of four points was set up starting from April 2008 (Fig. 5.3.3.1). The network's structure was the following: one master point, named MOIO, located in a stable part of the studied area, and three rover points (P1, P2 e P3), installed inside the landslide area. Points P1 and P2 were active between April 2008 and May 2009 and April 2008 and March 2009, respectively. Point P3, instead, provided measurements only during the March 2009-May 2009 period.

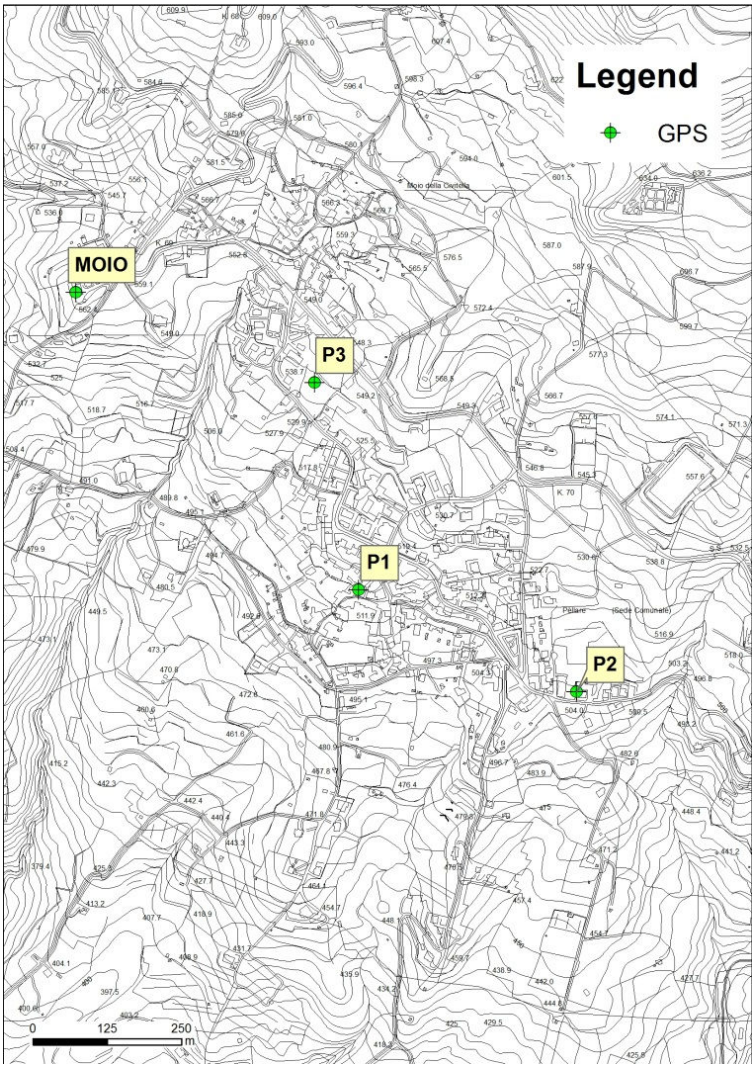

Figure 5.3.3.1. GPS network.

Subsequent elaborations allowed to calculate the three components of displacement, dx, dy and dz, corresponding to the E-W, N-S and vertical directions, respectively. Table 5.3.3.1 shows the results for the three monitored points. Points P1 and P2 registered a global displacement of approximately 2 cm, with predominant horizontal component (dx and dy); the vertical component

showed ten-fold lower values. Point P3 proved to be essentially stable (0,6 cm). Displacement's direction was also calculated (Figure 5.3.3.2), which appeared to be in agreement with terrain's morphology even in this case.

Table 5.3.3.2. GPS displacement components.

Point	Period	dx (m)	dy (m)	dz (m)
P1	April 2008 – May 2009	0.021	0.025	0.003
P2	April 2008 – March 2009	0.012	0.018	0.004
P3	March 2009 – May 2009	0.004	0.005	0.001

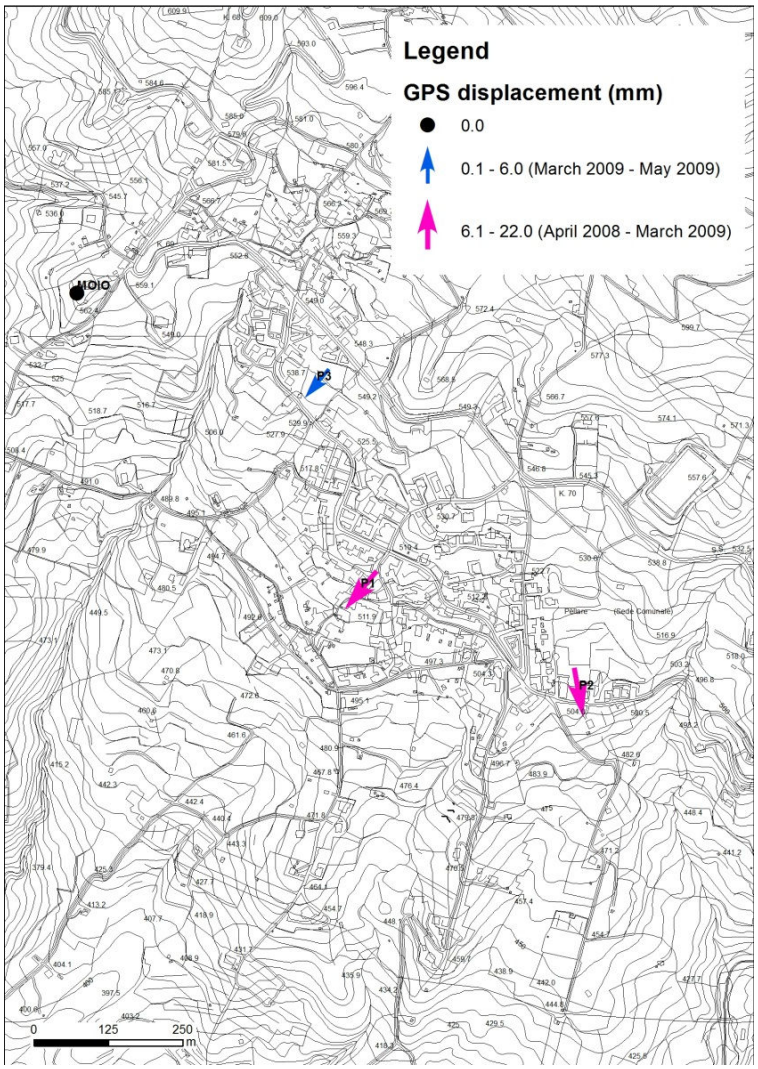

Figure 5.3.3.2. GPS displacement vector.

5.3.4 Interferometric measurements

The aim of this study was to assess the landslides' activity in two urban centres, Moio and Pellare (Calcaterra et al., 2008 and Calò et al., 2012) where slide-flows and roto-translational slides are the prevailing types of slope instabilities. Accessible ENVISAT images (53 ascending and 33 descending) for the 2002-2010 period have been elaborated. The availability of images acquired from different orbits allowed the combination of results in order to obtain the E-W and vertical velocity components.

A total of 53 images were available for the ascending track (Track 358 Frame 801); thirty-seven interferograms with spatial and temporal limits of 200 m and 210 days, respectively, were obtained. All images were then co-registered and the mean coherence map (Figure 5.3.4.1) was elaborated.

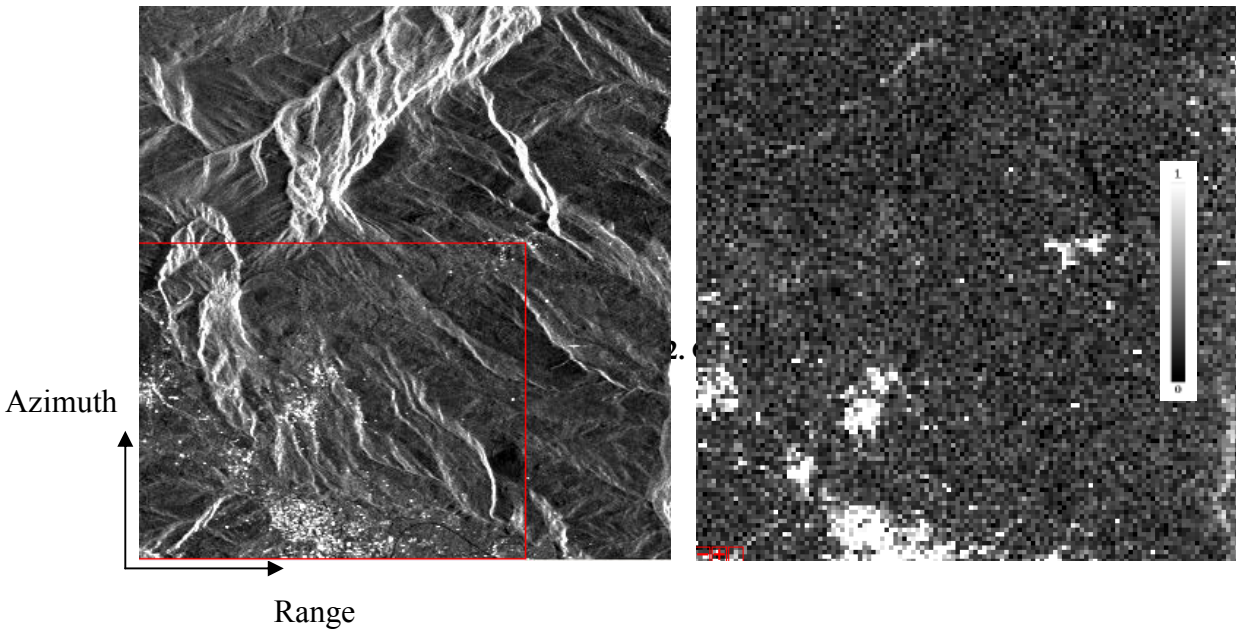

Figure 5.3.4.1. Amplitude and mean coherence map.

The next step was to identify those points with above-threshold coherence value. Owing to the necessity to have a sufficient number of points covering the entire study area, displaying, at the same time, a phase standard deviation of approximately 20° using a 15x3 multilook, two coherence value limits were set (0,40 and 0,35). Another crucial part of the interferometric chain was to determine a stable reference point; for this purpose, MOIO master point of the previously described GPS network was used. Processing was thus completed and the mean velocities map was elaborated (Figure 5.3.4.2).

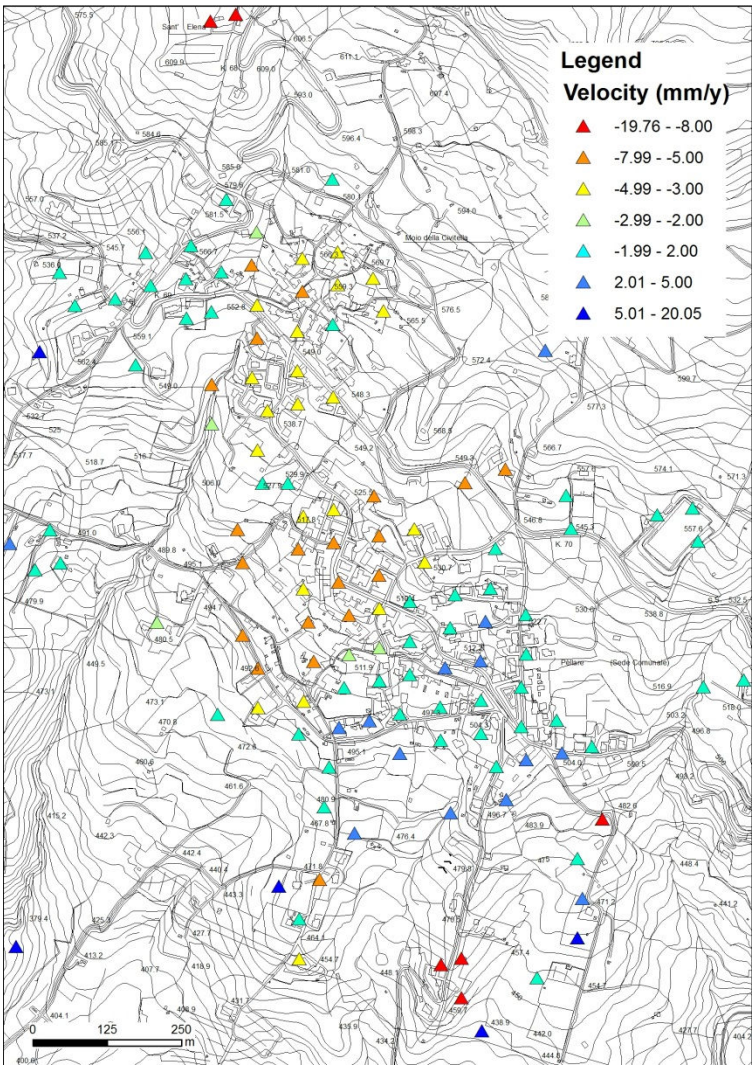

Figure 5.3.4.2. LOS velocity map for ascending images.

Reduced displacement velocities of 5-8 mm/year magnitude in EW direction (target-sensor connecting line in ascending orbit), as indicated by the negative sign, were calculated for both Moio (north) and Pellare (south) urban centers. This finding is also confirmed by traditional monitoring results previously shown.

Thirty-three descending images (Track 494 Frame 2799) were processed. The same maximum baselines as those of the ascending images were used. Even in this case, and for the already discussed reasons, it was necessary to identify two coherence threshold values, which were set at 0.5 and 0.4, respectively. A mean velocities map was then processed (Figure 5.3.4.3). This geometry's results mainly confirm the findings of the ascending one, with the exception that velocities have a positive sign (sensor-target connecting line in descending orbit), and almost the same direction (EW).

Combination of the results of both ascending and descending geometries shows that displacement's predominant component is the horizontal over the vertical one, since the two tracks' velocities have opposite signs (see example Figure 5.3.4.4).

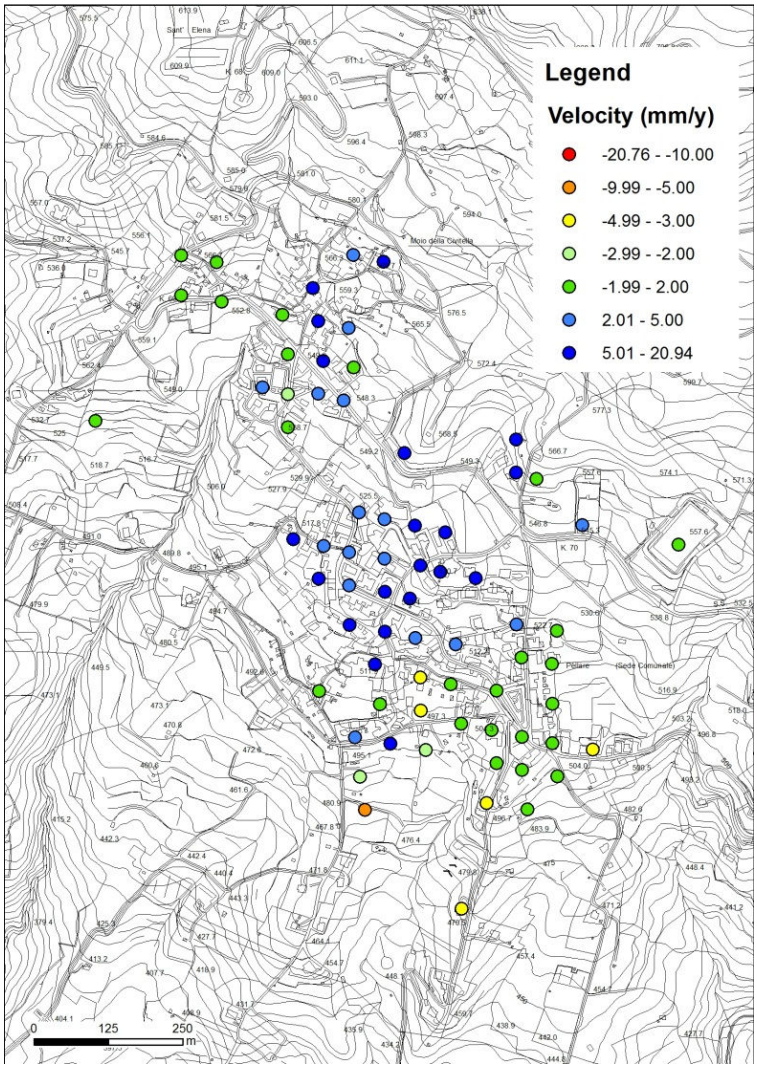

Figure 5.3.4.3. LOS velocity map for descending images

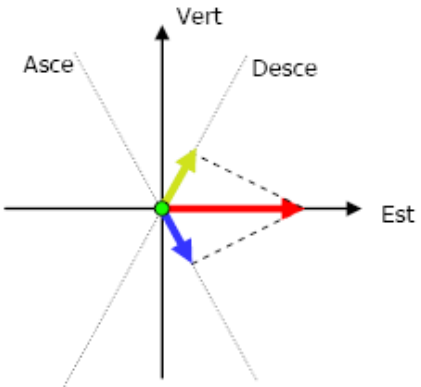

Figure 5.3.4.4. Horizontal displacement projected on LOS direction.

Table 5.3.4.1. Results of the decomposition.

Point	V_a (mm/y)	V_d (mm/y)	V_v (mm/y)	V_h (mm/y)
I1	-3.27	4.89	0.82	11.05
I3	-5.57	8.03	1.23	18.42
I4	-6.42	9.65	1.63	21.76
I7	-3.38	6.27	1.49	13.07
P2	3.07	-3.65	-0.27	-9.10

where V_a and V_d are the mean velocity in ascending and descending, and s_{xasce}, s_{zasce}, s_{xdesce}, and s_{zdesce} represent the direction cosines of the respective velocity vectors V_a and V_d. Table 5.3.4.1 shows the results of decomposition for points acquired by both geometries; the horizontal component appears to be at least ten times greater when compared to the vertical one. Finally, time series for two significant points and rainfall acquired by a recording rain gage located near Moio were compared in order to find a relation between rain peaks and displacements activation. As shown in the following graphs (Figure 5.3.4.5), no such relation was demonstrated, according to Herrera et al., 2010, probably due to two principal reasons: a) the temporal sampling of these satellites, which is 35 days for each SAR image in the best of cases, and b) the error associated with each measurement of the time series.

.

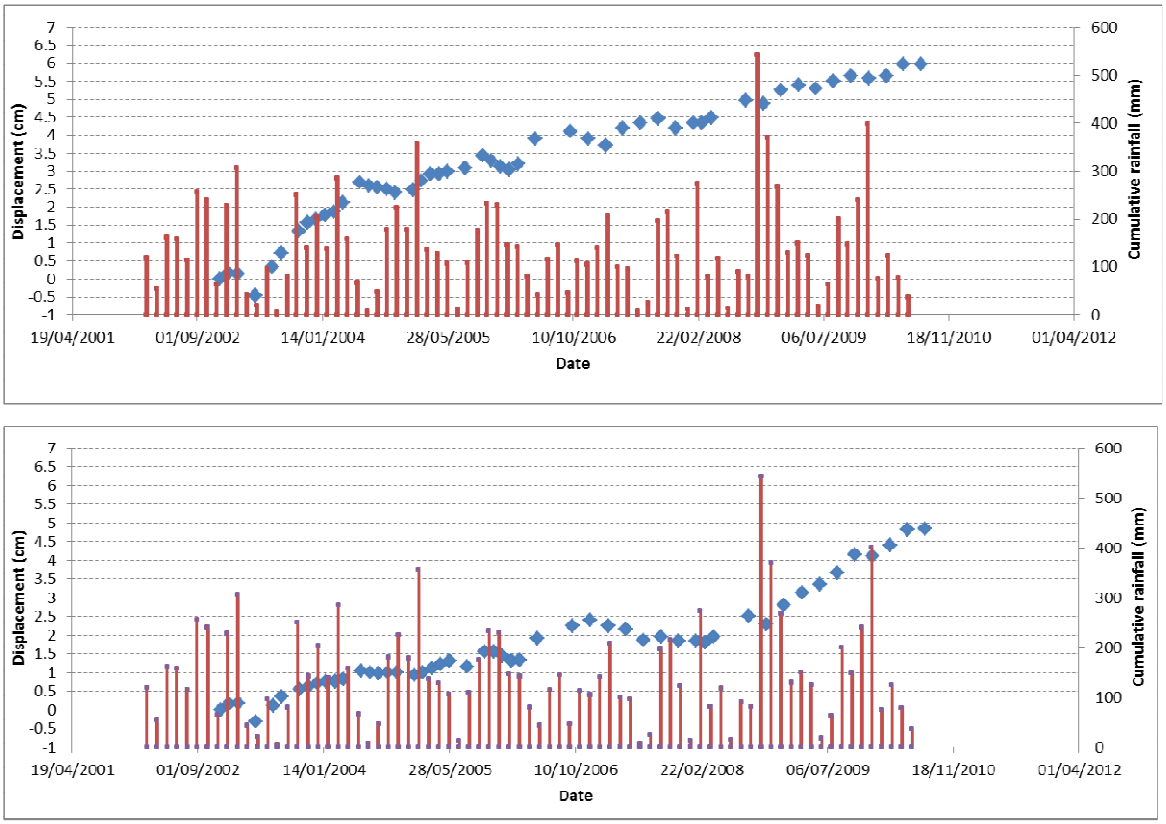

Figure 5.3.4.5. Cumulative rainfall and time series of displacement.

For these reasons and considering the analysed phenomena kinematics and triggering mechanisms, an attempt was made to identify a relation between the rate of rain which could trigger an event and the possible related accelerations. The latter could be recognized looking at the curve's variation of the gradient that describes the deformations temporal trend (Fig. 5.3.4.6). In some cases the accelerations actually corresponded to rain peaks. It is worth pointing out that the response to rain can be quite variable, owing to the different geotechnical characteristics of landslides soils and the morphological shape of the slope.

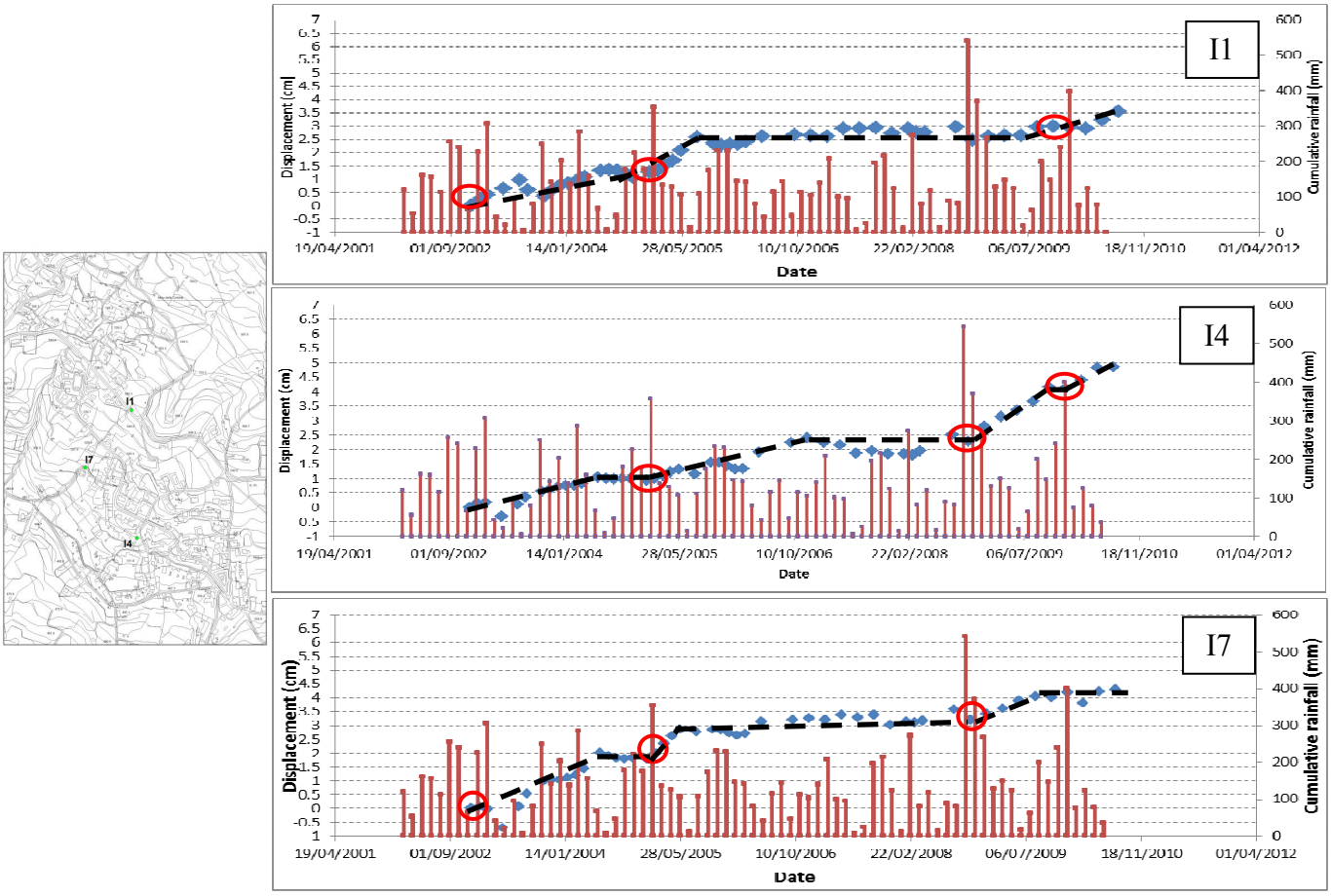

Figure 5.3.4.6. Example of relationship between cumulative rainfall and probable acceleration of landslide.

5.4 Calitri (Avellino)

5.4.1 Geological settings and landslides

Calitri is a small town in the Avellino province, Campania region, Italy, lying on the left side of the Ofanto River (Fig. 5.4.1.1). In the Calitri area, the oldest outcropping deposits belong to the Varicoloured Clay Group (Lower Cretaceous – Lower Miocene), made up of chaotic scaly clays (Fig. 5.4.1.1). The latter are interposed as olistostromic lenses within the Pliocene deposits of the Ariano Irpino Super Synthem, in the area represented by the Ruvo del Monte and Andretta synthems (clayey to arenaceous-conglomeratic sediments).

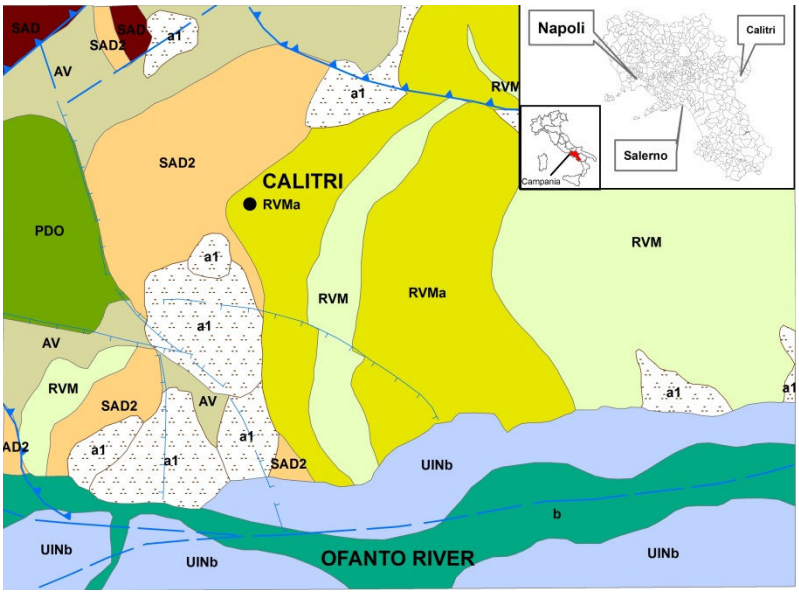

Figure 5.4.1.1. Geological scheme of the Calitri area (APAT 2006 – redrawn). Legend: UINb: alluvial deposits; a1: old and recent landslides; RVM, RVMa: Ruvo del Monte Synthem; SAD, SAD2: Andretta Synthem; PDO: Paola Doce Formation; AV: Varicoloured Clay Group.

The southern slope of the Calitri hill is affected, since historical times, by a large complex landslide (roto-translational evolved into earthflow), which prevailingly involves the pelitic terms (silty and marly clays, sands) of the Ariano Irpino Super Synthem. The last reactivation of the Calitri landslide, studied by several authors (e.g. Del Prete and Trisorio Liuzzi 1981; Hutchinson and Del Prete 1985; Budetta et al 1990; Parise and Wasowski 1998, 1999; Martino and Scarascia Mugnozza2005), occurred about three hours and a half after the main shock of the Campania-Basilicata 23 November 1980 M=6.9 earthquake (Martino and Scarascia Mugnozza 2005). Del Prete and Trisorio Liuzzi (1981) assessed the volume of the 1980 reactivation in the order of about 23 Mm^3, while, on the basis of some inclinometer readings, Hutchinson and Del Prete (1985) placed the maximum depth of the rototranslational body's rupture surface at about 100 m from ground surface (Fig. 5.4.1.2).

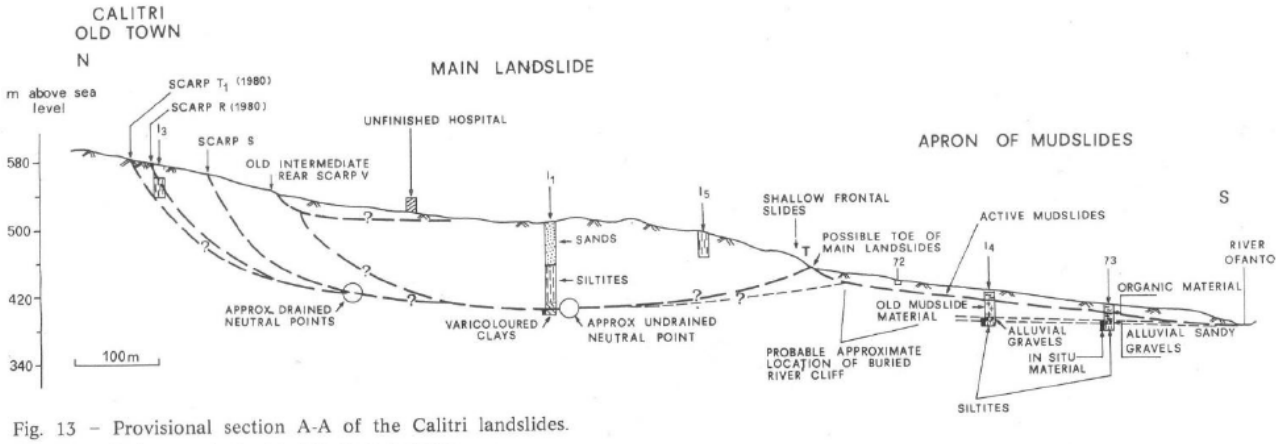

Fig. 13 – Provisional section A-A of the Calitri landslides.
Sezione provvisoria A-A della frana di Calitri.

Figure 5.4.1.2. Section of the landslide (after Hutchinson and Del Prete 1985).

Boreholes drilled in the toe zone revealed the shallower depth of the earthflow, which sealed about 4 m of alluvial terrace deposits (Hutchinson and Del Prete 1985; Budetta et al 1990). Several historical records of landslide activity at Calitri were found (Parise and Wasowski 1999; Martino and Scarascia Mugnozza 2005), the oldest of which dates back to 1694. The present-day state of activity of the landsides at Calitri has been briefly reported by Calò (2009) who, in the time span 1995-2009, recognized several small active landslides, mainly interesting the erosion areas in the eastern part of the main landslide (Fig. 5.4.1.3).

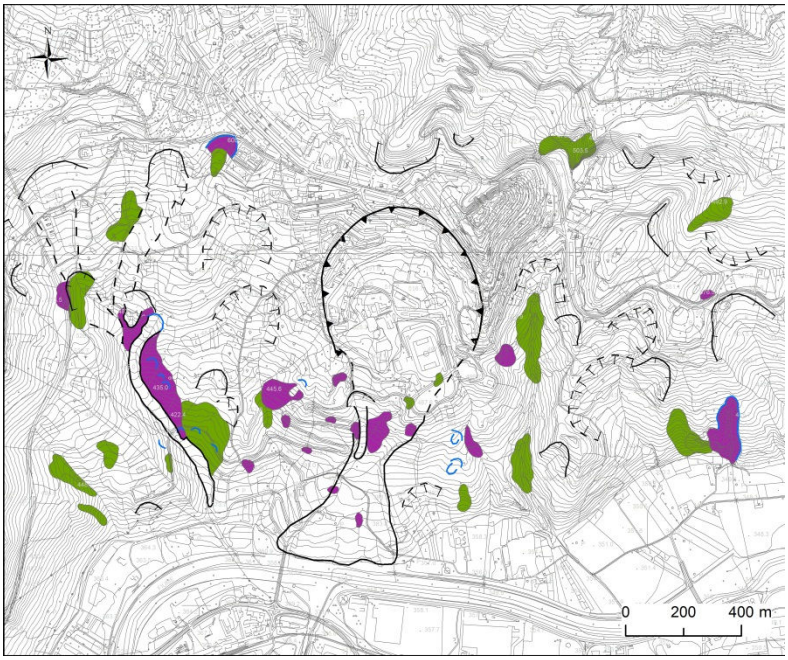

Figure 5.4.1.3. Landslide-inventory map of the southern side of the Calitri hill (Calò 2009, modified). Legend: Blue = active landslide; Black = dormant landslide; Violet = active erosion area; Green = dormant erosion area.

5.4.2 Procedures for SAR data interpretation

In Calitri test site PS interferometric data interpretation was applied. Direct interpretation of a given PS dataset in ascending and descending orbits acquisition is indeed difficult and often causes real motion perception problems to the user. Many times data acquired under a different LOS produce ambiguity in the definition of the real movement of the terrain. This ambiguity in the PS data display represents one of major constraint in the spreading and in the use of this kind of data and their interpretation for landslides monitoring problems.

For this purpose there are two different procedures proposed by TeleRilevamento Europa (T.R.E., 2006) and Campania Region (2008) respectively, which allow an easier interpretation of the PS data. Ascending and descending PS data used for this purpose were provided for by the Italian Ministry of Environment and processed by T.R.E.

The syntethic PS algorithm, developed by the SAR team at the Politecnico of Milan and Tele-Rilevamento Europa (T.R.E. 2008). Thus the components of the velocity vector in the horizontal direction East-West and in vertical direction (Zenith - Nadir) can be assessed.

In order to obtain the decomposition of the velocity vector, a resampling of the PS data on a geographical grid with a regular mesh is necessary. The methodology for the combination of PS ascending and descending data is outlined in Fig. 5.4.2.1.

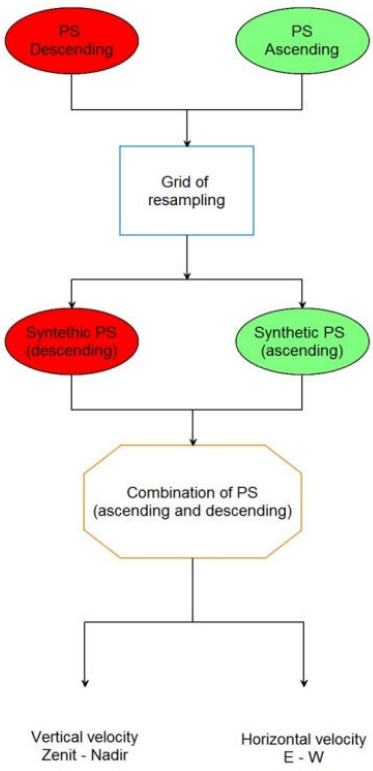

Figure 5.4.2.1. Synthetic PS procedure flow-chart.

The mean velocity value of PS points inside each mesh is calculated in order to obtain synthetic PS values for each cell. Such value is assigned to the center of gravity of the mesh.

For each cell the coefficient of variation is then calculated, allowing for comparison between different types of data. The coefficient of variation is defined as the ratio of standard deviation (σ_x) and the arithmetic means of speed value ($\bar{x}$). As such, it may be influenced by the contemporary presence of positive and negative values and thus, it becomes critical in presence of non-linear distortions:

$$RSD = \sigma_r = \frac{\sigma_x}{\bar{x}}; \qquad (1)$$

also, meshes with a coefficient of variation greater than 0.5 and lower than -0.5 are discarded.

This procedure is applied to both ascending and descending data sets, as to assess the component of velocity vector on a common grid of 'pseudo-PS'.

In the present work, based on the data acquired by ERS and ENVISAT satellites, the incident angles in ascending and descending geometry are the same and correspond to 23°.

TELLUS procedure has been tested by the Campania Region in the TELLUS project (PODIS Project Campania, 2008).

A ‘pre-processing’ statistical analysis based on frequency distributions of PS mean velocities in all the available datasets was carried out. Q1 (25%), Q2 (50%) and Q3 (75%) quartiles were calculated. The range (Q3 - Q1) is defined as the “interquartile range” (IQR). Mean velocity falling outside this interval (outliers) were discarded. More precisely, the values in the range [Q1 - (1.5 × IQR)] and [Q3 + (1.5 × IQR)], which are also characterized by a low average velocity, are considered to be the most reliable and therefore are defined as “normal”.

The procedure provides a morphometric approach, represented by the “correction” of the PS data, achieved by its projection on the slope considering both the slope angle and aspect information obtained from a Digital Terrain Model with a 10m × 10m cell resolution. Such “correction” is not applied to PS with slope angle value close to 3° and, consequently, provided with flat aspect. For this reason, prior to PS values statistical analysis, a database “cleaning” (elimination of PS with slope angle value lower than 3°) is necessary.

The mean velocity vector V_{mLOS} is projected along the direction of the maximum slope angle (Fig. 5.4.2.2) where:

a = 90° – b = Incident angle – slope

b = 180° – c = (90 - Incident angle) + slope

c = 180° – (90 - Incident angle) – slope

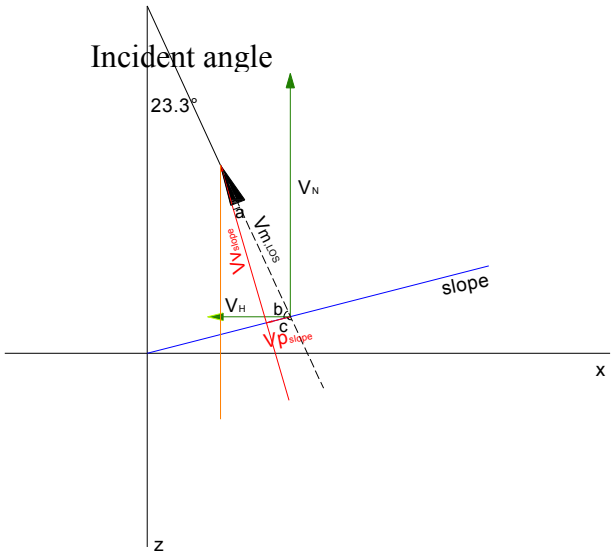

Figure 5.4.2.2. Projection of the velocity vector along the direction of the maximum slope angle ("Morphometric correction" after PODIS Project Campania, 2008, modified).

The value of the projected velocity vector (V_{pslope}) is:

$V_{pslope} = V_{mLOS} \cos b = V_{mLOS} \cos (90 – \text{Incident angle} + \text{slope})$ (5)

or

$= V_{mLOS} \sin a = V_{mLOS} \sin (\text{Incident angle} - \text{slope})$ (6)

and in orthogonal direction (V_{vslope}) is:

$V_{vslope} = V_{mLOS} \cos a = V_{mLOS} \cos (\text{Incident angle} - \text{slope})$ (7)

or

$= V_{mLOS} \sin b = V_{mLOS} \sin (\text{Incident angle} + \text{slope})$. (8)

The obtained V_{pslope} is decomposed and projected along the slope aspect (Fig. 5.4.2.3) in ascending and descending orbit of acquisition, where:

f = aspect – (90 – Azimuth angle)
g = 90° - f
h = 90° - i
i = (270 + Azimuth angle) - (180° - aspect)

The V_{pslope} projected along the slope aspect is equal to:

$V_{pasc} = V_{pslope} \cos f = V_{pslope} \cos (\text{aspect} – (90 – \text{Azimuth angle}))$

$= V_{pslope} \sin g = V_{pslope} \sin ((180 – \text{Azimuth angle}) – (90 – \text{Azimuth angle}))$ (9)

and

$V_{pdesc} = V_{pslope} \cos i = V_{pslope} \cos (\text{aspect} + (90 + \text{Azimuth angle})$

$= V_{pslope} \sin h = V_{pslope} \sin (- \text{Azimuth angle} - \text{aspect})$. (10)

For the ERS and ENVISAT datasets, the incidence angle of the sensor is equal to 23,3° and for the latitudes of interest a deviation of the orbit azimuth of 12,3° is calculated. Therefore:

a=23.3° - slope

b=66.7° - slope

c=98.3°

f=aspect - 77.7°

g=167.7° - aspect

h=-(12.3° + aspect)

i=102.3° + aspect

The result of this correction cannot replace the original PS, but it can resolve the reading ambiguities with respect to the slope instability morphodynamics.

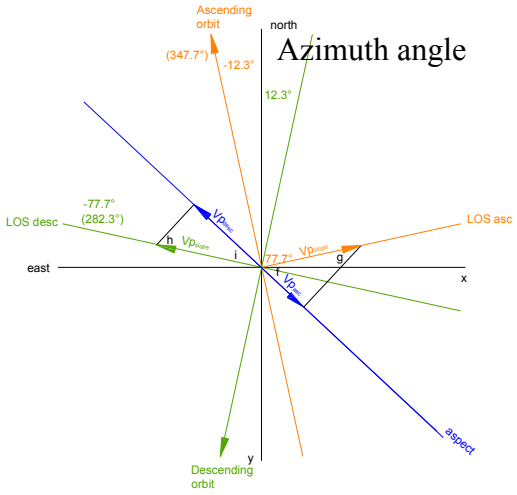

Figure 5.4.2.3. Projection of the velocity vector along the slope aspect ("Morphometric correction" after PODIS Project Campania, 2008, modified).

5.4.3 Results

Both the above procedures were applied to the entire available dataset. In order to provide clearer results, we focus here on a limited area near the scar of the Calitri main landslide re-activated by the November 23rd, 1980 earthquake.

For the first procedure, and in particular during the data resampling, three different regular mesh sides have been used (50, 70 and 100 m). For each mesh the number of PS, the average velocity and standard deviation were calculated, in order to establish which mesh provided the best results. The results highlight a significant difference in synthetic PS obtained for different size of the mesh, as shown in Table 5.4.3.1.

Table 5.4.3.1. Synthetic PS obtained by the processing.

Satellite (m×m)	Synthetic PS
ERS 50×50	17
ENVISAT 50×50	18
ERS 70×70	11
ENVISAT 70×70	14
ERS 100×100	6
ENVISAT 100×100	7

Most of the synthetic PS are located at the upper-middle part of the landslide because this zone coincides with the most urbanized area. The decomposition of the mean velocity vector of synthetic PS calculated according to the vertical (V_V) and horizontal direction E-W(V_E), gave the results shown in Fig. 5.4.3.1

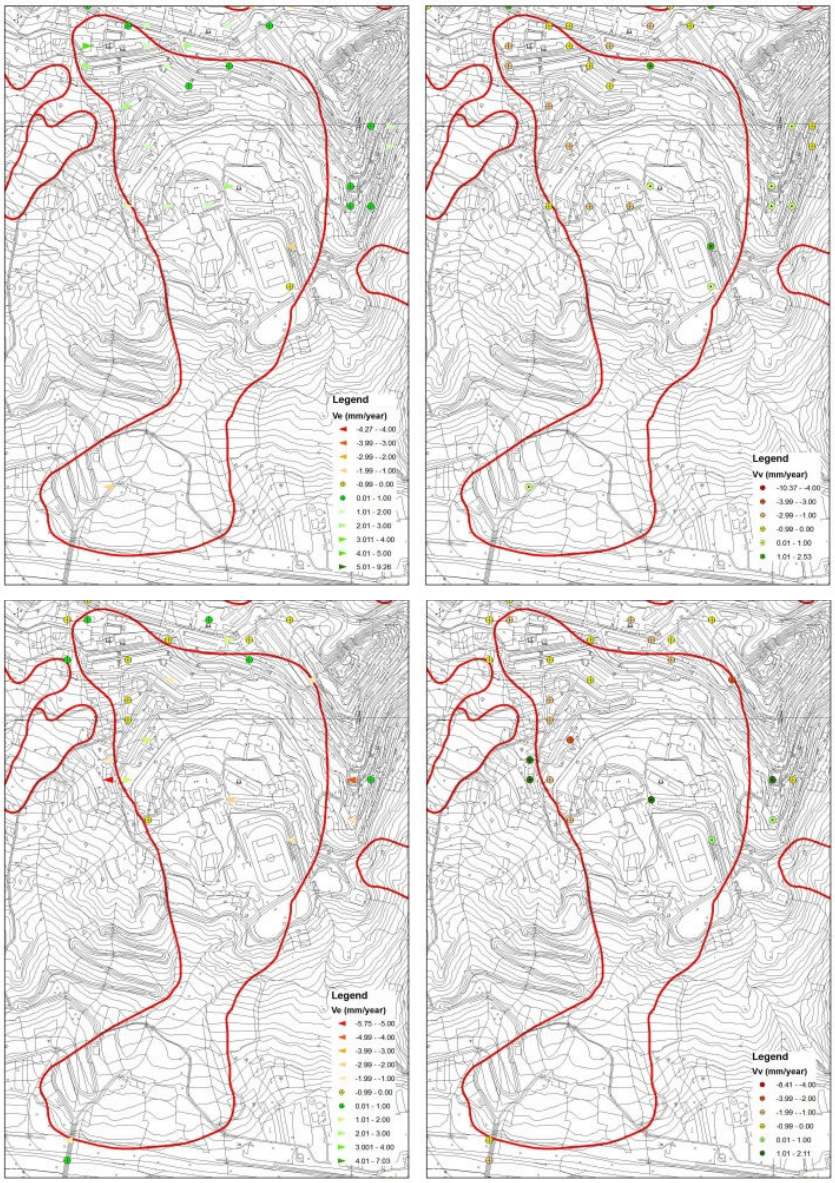

Figure 5.4.3.1. Horizontal and vertical component for synthetic PS: ERS (above), ENVISAT (below).

For both ERS and ENVISAT satellite missions, the synthetic PS show that the horizontal components of displacement are always in agreement with the morphology of the territory. In particular, in this area ERS shows the dominance of the horizontal component, while the ENVISAT synthetic PS offers a prevalence of the vertical component.

Following the second procedure, after the phase of pre-processing, i.e. elimination of PS with slope values lower than 3° and PS outliers, the results reported in Tab. 5.4.3.2 have been obtained. Accordingly, about 20% of PS data acquired in both satellite missions were discarded.

Table 5.4.3.2. PS obtained from pre-processing.

Satellite	Total PS	PS pre-processing
ERS asc	67	51
ERS desc	116	93
ENVISAT asc	148	122
ENVISAT desc	82	65

The results show that mean velocity values of all PS are very low, varying between -1 and 1 mm/year for PS ascending and descending ERS and ascending ENVISAT.

On the other side, higher values (about 3 mm/year) have been found for the PS descending ENVISAT in the north-west of the landslide.

Fig. 5.4.3.2 reports the components of the ascending and descending PS, along with the average velocity vectors obtained from this procedure.

Finally, is possible to highlight that using the PS Synthetic procedure, most of the synthetic PS resulted to fall in the middle-upper part of the analyzed landslide and both ERS and ENVISAT PS horizontal displacement components follow the slope attitude. ERS showed dominance of the horizontal component, while for the ENVISAT synthetic PS the vertical component prevails. Since the ERS and ENVISAT dataset cover two different time periods, we presume that this difference could be related to a different behavior of the landslide over time. This is also confirmed by the inclinometer readings measured for the period 1992-1994 which show a dominance of horizontal component. In our experience displacement components values (VE and VV) always proved to be rather low and often negligible.

The results deriving from the application of the TELLUS procedure show that also in this case very low values of the mean velocity components are obtained. A possible explanation lies in the fact that, owing to very low vector values in the original PS data set, the subsequent vector decomposition produced negligible slope direction components, which proved to be strongly correlated to the slope angle values, as also reported by Cascini et al. 2009, 2010.

Therefore, both procedures provide similar results and they suggest that the studied landslide is apparently stable.

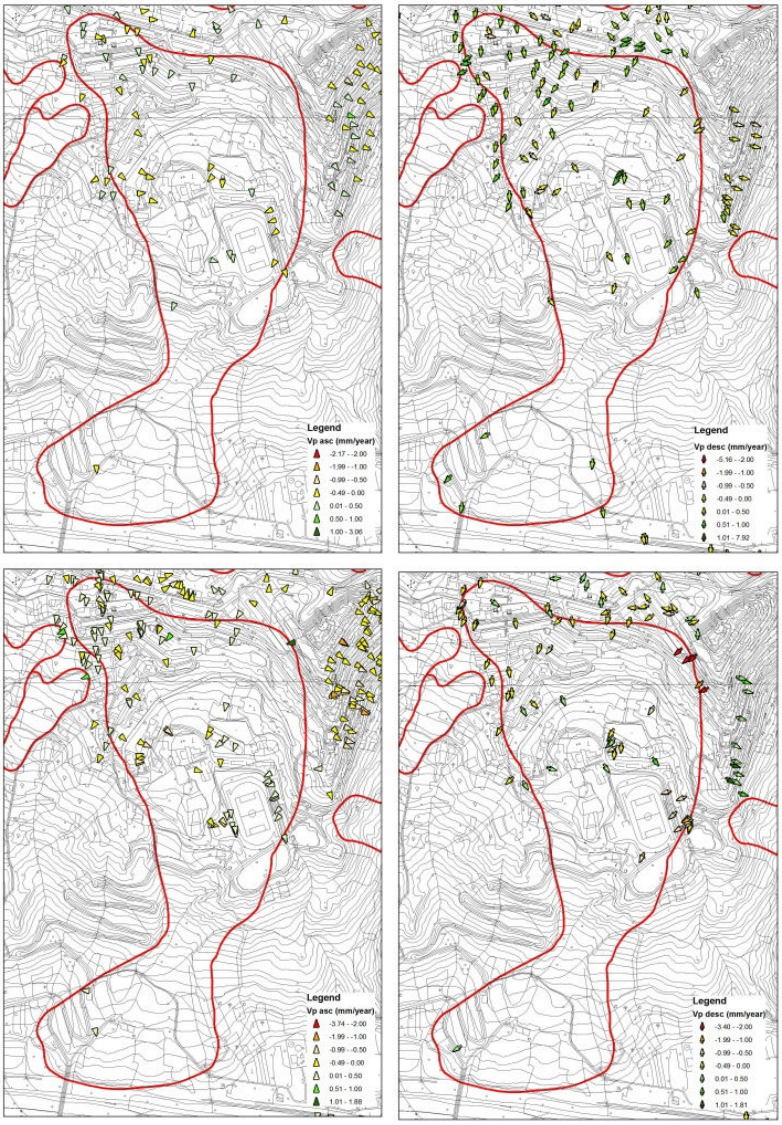

Figure 5.4.3.2. Component of velocity for ERS (above) and ENVISAT (below) PS by means of TELLUS procedure.

CHAPTER 6

6. Conclusions

Prevision, prevention and mitigation of a variety of instability phenomena, such as landslides, subsidence and sinkholes require reliable procedures and technologies to reduce the hazard posed to human life. In particular, monitoring plays a key-role in natural hazard management by providing cost-effective solutions to mitigate or minimize disaster losses. Remote Sensing methods have been successfully adopted for a wide range of applications in disaster management; among them the Differential Interferometry Synthetic Aperture Radar (DInSAR) proved to be a valuable tool to detect ground deformations.

The DInSAR technique is by now well-established and its operational use for almost continuous monitoring of large areas of the Earth surface is now starting. The aim of the present work was to verify the suitability of differential interferometric techniques as complementary tools for slow-moving landslides monitoring by comparing the interferometric results with conventional ground-based data (Meisina et al. 2006, 2008, Herrera et al., 2010).

Differential interferometric techniques have been applied to monitor ground deformations on different case studies, located in the center-southern Appennine of Italy. The test sites are prone to different types of slow-moving landslides, from slides to complex phenomena, in the same geological and morphological contexts.

The first phase of this work consisted in learning the basic concepts of DInSAR applied to slow-moving phenomena throughout the detailed study of SAR images processing techniques. The ability to "understand" SAR data correctly, crucial for a reliable interferometric processing whatever the context of application is, was first acquired under the supervision of the researchers of the Department of Biomedical, Electronics and Telecommunications Engineering of the University of Naples Federico II and then during the research period spent at the Department of Signal Theory and Communications of the Universitat Politecnica de Catalunya.

The application of DInSAR to the different study areas and its subsequent results allowed to critically analyze constraints and advantages of this technique in the field of landslide monitoring.

The analysis first focused on the problem of **slope-facing,** which greatly affects the possibility to use this technique. The influence of this factor is related to specific reasons of the acquisition system geometry (semi-polar orbit). Indeed, for polar orbits slopes that are ideal for InSAR

monitoring are those facing in a general East or West direction. This maximizes sensitivity of the SAR instrument, because it is pointed in the direction of the assumed slope movement. Slopes that are facing in a North or South direction may be effectively monitored with InSAR; however, the detectable movement is lower for these slopes, and this is related to the slope geometry.

In Agnone test sites, the slope was East-facing and the landslide's principal component had a W-E direction, as also demonstrated by the available topographic and GPS measures. Such configuration has thus allowed to carry out the preliminary steps of the interferometric process (interferograms and coherence maps) obtaining promising results. Anyway, owing to the limited number of available images (11 in descending orbit), the whole interferometric process didn't produce reliable results in terms of velocity rate.

Moio della Civitella test site is composed of two urban centres, Moio and Pellare, both developing on West-oriented slopes. For this site, images in both ascending and descending acquisition geometries were available; this made it possible to combine the results obtained by the two processing and so to compute both the horizontal and vertical displacement components, ultimately allowing for a better phenomenon understanding.

On the contrary, the two test sites of Costa della Gaveta and Calitri, had unfavorably exposed slopes.

The slope affected by Costa della Gaveta and Varco d'Izzo phenomena are predominantly South-oriented. This limitation was partly overcome by the landslides principal components, both W-SW directed, which allowed to identify the active movements. In order to perform a preliminary evaluation of the magnitude of the detectable deformation, the percentage of movement of a potential landslide measurable by the D-InSAR technique is calculated (Plank et al., 2012). For this purpose, a specific GIS (Geographical Information System) routine was implemented. The results here obtained represent a consistent pre-survey assessment of the potential applicability of the D-InSAR technique for mass movement monitoring prior to radar surveys (Cascini et al, 2009). This allows stakeholders to evaluate the appropriateness of D-InSAR application to a certain area of interest and, subsequently, to optimize the global costs. Moreover, as GIS is commonly used in the field of Earth sciences, even researchers with little or no experience in D-InSAR may successfully implement this GIS procedure. Furthermore, by repeated analyses for different radar acquisition geometries is possible to identify the most suitable imaging geometry (incidence angle and orbit). Nevertheless, also other factors, such as the spatial resolution of the radar sensor, data availability (repeat cycle) and atmospheric disturbances, have to be taken into account when deciding whether to use D-InSAR or not.

Actually, for Costa della Gaveta the best results were obtained: six out of eight evaluated points showed the same ground velocities in both traditional and interferometric monitoring techniques.

Calitri test site was the most disadvantaged as both the slope aspect and the landslide direction were N-S oriented. For this reason, the work focused on the interpretation of PS data furnished by MATTM and elaborated by means of the algorithm developed by T.R.E.

The analysis then dealt with another problem which may limit the use of the DInSAR technique, that is the **slope grade.** Steep slopes are often difficult to study with interferometric technique because of the geometrical distorsions in the SAR images (layover, foreshortening and shadow effects). In addition, complicated topography creates some problems in eliminating the residual topographic phase, especially when an accurate DEM is not available. Slope grades that are much less than the SAR incidence angle are preferable (Colesanti e Wasowsky, 2006). In this work slope grade did not significantly affect the results obtained in the different studied sites, owing to the similar morphological contexts with rather gentle slopes. An additional factor which may have limited the possible bias deriving from topographic aspects was the use of high resolution DEMs (10 m x 10 m), obtained from Technical Regional Maps, which also allowed a more precise georeferencing of results.

An aspect which greatly affected this work's elaborations and induced careful thinking was the **Image Coherence**. The interferometric coherence is one of the main factors in determining suitability. Slopes with heavy brush, fast growing vegetation and deciduous forests are generally not suitable for interferometric monitoring unless natural or artificial (e.g., buildings, infrastructures, corner reflectors) point targets are present. And this is what usually characterizes the landslides areas.

As already pointed out, coherence threshold have to be set in order to identify the points to further analyze by means of interferometric processing; moreover, such coherence allow to assess the error related to deformations' estimation in terms of phase standard deviation. Thus, coherence affects both quantity and quality of analyzed points.

All the studied areas showed a limited number of natural reflectors because of a low grade of urbanization. For this reason and in order to select an adequate number of points for a complete phenomenon representation, it was necessary to set low coherence thresholds. Such thresholds have been set up taking into account the function relating coherence and phase standard deviation for various numbers of looks. Indeed, by means of such function, coherence values producing phase standard deviations lower than 20°, corresponding to deformation standard deviations of 1.5 mm,

have been set for all cases. Considering the rate of the deformations of the studied phenomena, such value is believed to be certainly acceptable.

The Agnone landslide here described develops in a totally rural area, with no natural reflectors. In order to overcome such limit, artificial permanent scatterers (Trihedral Corner Reflector - TCR) have been manufactured and installed. This kind of artificial reflector was chosen on the basis of scientific studies (Sarabandi et al., 1995, Ferretti et al, 2007, Doerry, 2008). TCRs were actually identified on the basis of evaluations of the Radar Cross Section (RCS), which is the parameter that mostly affects the visibility of such devices. The latter, together with the use of high resolution Cosmo-SkyMed images, has brilliantly solved the problem of low coherence values: the obtained values proved to be quite high (0.7-0.8), with low phase standard deviations (10°).
The problem of low coherence values was also faced in Costa della Gaveta site, where the almost complete absence of natural reflectors only allowed a partial monitoring of the landslide's slope. Recently, a specific project for the acquisition of high resolution Cosmo-SkyMed images for this site has been signed with ASI and TCRs will soon be installed in this area as well.

The availability of **Existing Site Data** has proved to be a crucial point for the development of this thesis. First of all, the availability of a recent DEM is important for the application of InSAR, as described above. High resolution DEMs (10 m x 10 m), obtained from Regional Technical Maps, have been used for all studied sites.

Moreover, the availability of site survey and control data, coupled with orthophotography, is very useful to maximize the accuracy of the positioning of the InSAR data. These data help to provide a means to interpret the interferometric-derived movement information and to determine the overall impact of any significant movement. In this perspective and in order to successfully apply the SUBSIDENCE software, in situ derived data allowed to set relevant parameters, such as the points considered to be stable (seeds), used in the subsequent phase of triangulation (integration) to estimate the displacements' velocities. The identified seeds, obtained from GPS measurements (for example in Moio della Civitella and Costa della Gaveta), allowed to check and to validate the interferometric results referred to the points which were localized in instable zones and whose movements have been measured by means of in situ GPS. A correct validation of the interferometric elaborations was achieved by comparing the latter results with traditional monitoring campaigns acquired data (inclinometers, levelling measurements and GPS measurements), as in the Moio della Civitella and Costa della Gaveta cases. Although the aforementioned problems (slope aspect, low coherence, etc.) have been encountered in both sites, this work shows that in all the studied areas the use of interferometric techniques displays results

which prove to be consistent with field surveys and traditional monitoring approaches (inclinometers, topographic measurements and GPS measurements).

Encouraged by these findings, interferometric technologies must be increasingly used in the future, even considering the excellent results of already developed projects, such as MORFEO (MOnitoraggio del Rischio da Frana con tecniche di Earth Observation, Landslide Risk Monitoring by Earth Observation techniques), in which industries, CNR (National Council of Research) and University departments took part, and the First Italian Extraordinary Plan for Environmental Remote Sensing proposed by the Italian Ministry of Environment.

MORFEO was a pilot project whose aim was to develop pre-operative Civil Protection services for landslides by means of Earth Observation technologies. It consisted in an integrated System which was able to supply products and services in support of prevision and monitoring activities for Civil Protection emergencies' management. Among the products there were interferometric analyses for superficial deformations' monitoring.

The First Italian Extraordinary Plan for Environmental Remote Sensing aimed at the rapid creation of a database to **support decision making processes** in all hydrogeological upheaval at-risk areas and at fostering methods and results data set sharing. These objectives assume a strategic value for PST-A. The data set was to be created by means of an evolved and specific remote sensing plan and by the integration of pre-existing or newly developed Statal or Local data sets.

In the near future, the second stage of the Italian Extraordinary Plan for Environmental Remote Sensing and the availability of VHR last generation images acquired by TerraSAR-X, COSMO-SkyMed and SENTINEL constellations will hopefully allow us to obtain better results in terms of ground resolution and time revisiting by means of algorithms that produce increasingly reliable results. On this point it is worth mentioning that over the past years many improvements have been brought to the SUBSIDENCE software, which is now able to work also on other types of algorithms defined as high resolution. Such algorithms select points on the basis of the amplitude (Centolanza et al., 2012) or of the spectral correlation (Iglesias et al., 2012). Application of such well-established algorithms to the studied areas here described has been attempted, but unfortunately poor results were obtained due to the low resolution of available images (ENVISAT ASAR) and, most of all, to the sites' morphology.

In conclusion, the technology here analyzed has undoubtedly allowed to move a step forward in the field of landslide monitoring, especially in phenomena preliminary studies (vast areas, several decades long database, slow or extremely slow deformations, etc.), but full knowledge of in situ monitoring techniques is crucial for its appropriate use.

Appendix: DInSAR processing with SUBSIDENCE software

The SUBSIDENCE software, which implements the Coherent Pixels Technique (CPT) developed by the Department of Theory of the Signal and Communications of the UPC, comprises all steps associated to the interferometric processing: extraction of parameters from SLC, image co-registration with external DEM for a better precision, interferometric filtering, differential interferogram generation, pixels selection and model adjustment. After the whole processing it is obtained for each selected pixel: the linear deformation velocity, the DEM error, the atmospheric phase screen and the deformation time series. All products are geocoded in UTM coordinates and they can be visualized with GIS or GoogleEarth.

The SUBSIDENCE software is composed by 2 parts: PRISAR and SUBSOFT.

PRISAR consists of a set of C routines designed for: reading the necessary parameters from the SLC headers, the calculation of the interferograms and the coherences, while SUBSOFT is an application in IDL that uses the PRISAR's outputs previously calculated (interferograms and coherences) to extract the deformation evolution of the area of interest. Both PRISAR and SUBSOFT are run by IDL.

All routines utilities are controlled and configured by both general and specific parameter files. These latter are located in a specific directory (*datafiles*). The structure of the directory is defined as follows (Fig. 1):

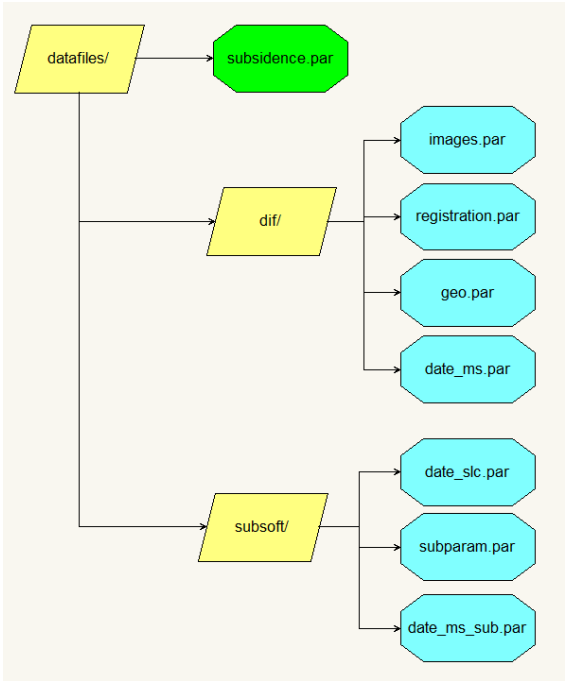

Figure 1. Datafiles structure

To carry out a full processing, one has to follow these steps:

a) Configuration of the general parameters file subsidence.par;

b) Configuration of the specific parameters files of PRISAR (images.par, registration.par, geo.par and date_ms.par);

c) Configuration of the specific parameters files of SUBSOFT (date_slc.par, subparam.par, date_ms_sub.par);

d) Subsidence execution.

a) The subsidence.par file is a flag archive which controls each part of the whole processing. Moreover it contains the information about the paths of the files involved in the processing, such as the location of each SLC data or the final results directory:

   - the directory where the results of the chosen processes will be stored;
   - the SLC images directory;
   - the SLC parameters files directory (where they will be stored or generated);
   - the registered images directory;
   - the interferograms directory;
   - the DEM (Digital Elevation Model) directory;
   - the DEM data format.

b) It can be divided in two parts: the first is dedicated to the interferograms selection criteria (temporal and spatial baseline) and the second one to the PRISAR processing itself.

   Interferograms selection: There are several methods to make an interferogram selection:

   - It can generate automatically all the possible pairs or impose restrictions between the possible pairs (automatic).

   - It can specify an interferogram set using the parameters file date_ms.par (manual) and making a list of interferograms we want to generate. This choice reduce the number of the interferograms and it can be useful in the case of a large set of images.

   - There is also an ideal selection based on a Delaunay triangulation. There is the possibility of generating an interferograms set referred to the same master.

PRISAR processing: The first step in the interferometric chain is to extract all the parameters for each image. The extraction routines are integrated in the main routine. The software is able to extract parameters from ERS, ENVISAT, TerraSAR-X, Radarsat2 and Cosmo-SkyMed images.

Once got all the parameters for each image involved in the processing we can proceed with interferometric chain. There are many step between the images set and the interferograms set.

Below will be described the different steps:

- Control point: This step carries out the automatic calculation of the checkpoints useful for the registration;

- Registration: we will perform the images registration. **Coarse registration**: Align the cropped images with an accuracy of a pixel for the whole image. This step is performed doing the amplitude correlation of a portion of both images. **Fine registration**: Align the cropped images with an accuracy of a fraction of pixel, processing each pixel separately. This step can be done also with amplitude correlation of block divided images or with geocoding techniques that require an external DEM and the orbital information;

- Registration type: It indicates the registration method that will be carried out (amplitude correlation or with an external DEM);

- Orbits: The orbital calculations will be carried out using information deriving from the registration process. This step is useful to evaluate the perpendicular baseline;

- Interferograms: we will perform the generation of the interferograms;

- Filtering: to carry out the azimuth/range filtering of the interferograms (for low and high resolution images);

- Coherence: Coherence maps calculation (cross-correlation value);

- Differential interferogram: to process the differential interferogram calculation. Starting from the interferogram we will subtract the topography information and the flat earth to isolate the movement information;

- Differential coherence: we calculate the coherences using differential interferograms that have been calculated in the previous step (we will calculate the coherences without topography);

- Clean: Here will be cancel the directories of those interferograms that do not respect the restriction pointed in the interferograms selection criteria.

c) Also in case we can divide this step into two parts: the first is devoted to the interferograms

selection criteria and the second one to the SUBSOFT processing itself.

Interferograms selection: Also for the SUBSOFT processing we can select an interferogram set between the interferograms generated with PRISAR.

- The set can be generated manually from date_ms_sub.par;
- Otherwise SUBSOFT itself will generate a list using the restriction parameters such as spatial baseline, temporal baseline and shift doppler.
- Moreover, here we can be specify the multilook of the interferograms.

SUBSOFT processing (Linear part of the processing)**:** Also for SUBSOFT routines the first step is focused on the pixel selection. We can select pixels with three methods:

- Coherence pixel selection can detect distributed targets. It is a fast and simple method since we could get a reliable selection with few interferograms. Its main weakness is a loss of spatial resolution.
- In urban areas it is more interesting to work with other two methods of selection at high resolution: a) Amplitude Selection and b) Sublook Correlation, instead of detecting distributed targets we look for point targets and we will have only one scatter in our cell resolution. This will achieve a better spatial resolution in detection of movements for scenarios with a high density of point targets.

The process for the **linear component** consists in:

- Coherence selection: will be selected those pixels that overcome the coherence threshold in a certain percent of the interferograms, guaranteeing a coherence minimum in all of them;
- Calibration: the SVA and the radiometric calibration will be carried out;
- Amplitude selection: the amplitude selection method;
- Sublook correlation selection: here will be done the pixels selection by spectral correlation between Sublooks;
- Write sublook: we generate sublooks of the registrated images for the pixels selection method by Sublook Correlation. Also it applies the SVA routine to each image and writes the absolute value of the image in the image directory;
- Triangulation: the triangulation process between the selected pixels;
- Seek minimization: Process to calculate the ideal increments;

- Data generation: Generation of the information for the following routine;
- CGM: it to search the increments using the CGM method;
- Unwrapping: the unwrapping process of the increments to get the absolute values;
- Unwrapping CGM: the CGM unwrapping method;
- Test Unwrapping: the unwrapping test of the increments;
- Mask: Generation of the linear deformation map using the selected points.
- Map: Generation of the interpolated velocity, DEM error map.

The process for the **non-linear component** consists in:

- Residue: Generation of not linear residue for each interferogram;
- Unwrapping: the unwrapping method at high spatial resolution;
- CGM: indicates the unwrapping method;
- Atmosphere interferogram: Extraction of the atmospheric artifacts;
- Delete atmosphere: Elimination of the atmosphere of the first image, which is in all the images;
- Generation residue: Process to generate a new residue at high spatial resolution;
- Temporal evolution: Estimation of not linear movement at high resolution for every SLC;

Finally, there is the part of representation of the results:

- Geocode: the georeferencing process;
- KML: generation of kml file in order to show in GoogleEarth or GIS.

References

Almagià R., 1910. Studi geografici sulle frane in Italia. Memorie della Società Geografica Italiana, XIV, Roma.

Amanti M., Chiessi V., Bertolini G., Ramasco M., De Nardo M.T., 2001. Guida alla compilazione della scheda frane IFFI (Inventario Fenomeni Franosi in Italia), Allegato 1 al Progetto IFFI. Servizio Geologico Nazionale, Roma.

Amelung, F., Galloway, D.L., Bell, J.W., Zebker, H.A., Laczniak, R.J., 1999. Sensing the ups and downs of Las Vegas: InSAR reveals structural control of land subsidence and aquifer-system deformation. Geology, 27 (6), pp. 483-486.

Arnaud A., Adam N., Hanssen R., Inglada J., Duro J., Closa J., and Eineder M., 2003. ASAR ERS interferometric phase continuity. International Geoscience and Remote Sensing Symposium, 21-25 July 2003, Toulouse (France), (CDROM).

Berardino P., Fornaro G., Lanari R., Sansosti E., 2002. A new Algorithm for Surface Deformation Monitoring based on Small Baseline Differential SAR Interferograms. IEEE Transactions on Geoscience and Remote Sensing, 40, 11, pp. 2375-2383.

Blanco P., Mallorqui J.J.,Duques., Navarrete D., 2006. Advances on DInSAR with ERS and ENVISAT data using the Coherent Pixels Technique (CPT), Proc. IGARSS 2006, Denver(USA).

Blanco P., 2009. SAR Differential Interferometry for deformation monitoring under a multi-frequency approach. Doctoral Thesis

Bonardi G., D'Argenio B., Perrone V., 1988. Geological map of southern Apennine (scale 1:250000), Memorie Società Geologica Italiana, 41, (in Italian).

Bonnard C., Noverraz F., Dupraz H., 1996. Long-term movement of substabilized versants and climatic changes in the Swiss Alps. In: Senneset K (ed) Landslides. Seventh international symposium on landslides. Balkema, Rotterdam, pp 1525–1530.

Bonnard C., 2008. Introduction to Lanslide: mechanisms of landslides and specificities of large landslides. Presentation at laram summer school, Ravello, Italy, 2008.

Bressani L.A., Pinheiro R.J.B., Eisenberger C.N., Soares J.M.D., 2008. Movements of a large urban slope in the town of Santa Cruz do Sul (RGS), Brazil. Landslides Eng Slopes. From the Past to the Future1:293–298.

Budetta P., Calcaterra D., de Riso R., Santo A. Geology and landslides of the Upper valley of the Ofanto River southern Apennines). Memorie Società Geologica Italiana 45: 309-324. (in Italian) 1990

Burghaus S. ,Bell R., Kuhlmann H., 2009. Improvement of a terrestric network for movement analysis of a complex landslide. Presentation at FIG conference, Eilat, Israel, 2009.

Calcaterra D., Ramondini M., Calò F., Longobardi V., Parise M., Galzerano C.M., 2008. DInSAR techniques for monitoring slow moving-landslides. In: Chen Z, Zhang J-M, Ho K, Wu F-Q, Li Z-K (eds) Landslides and engineered slopes. From the Past to the Future Proceedings of the tenth international symposium on landslides and engineered slopes. Pp 1089–1094.

Calcaterra S., Cesi C., Gambino P., 2008. Reti di monitoraggio integrato GPS-geotecnico delle frane di Lago (CS) e Costa della Gaveta (PZ). In: Proceedings of XII national conference ASITA, L'Aquila, Italy, 21–24 October 2008, 1:581–586

Calcaterra S., Cesi C., Di Maio C., Gambino P., Merli K., Vallario M., Vassallo, R., 2010. Surface displacements of two landslides evaluated by GPS and inclinometer systems: a case study in Southern Apennines, Italy. Natural Hazards. DOI: 10.1007/s11069-010-9633-3.

Calò F., 2009. Analysis of slow-moving landslides in Southern Apennines by integrating ground monitoring and Remote Sensing techniques, PhD Thesis, Federico II University of Naples, Italy.

Calò F., Calcaterra D., Iodice A., Parise M., Ramondini M., 2012. Assessing the activity of a large landslide in southern Italy by ground-monitoring and SAR interferometric techniques. International Journal of Remote Sensing, 33(11), 3512.3530.

Cascini L., Fornaro G., Peduto D., 2009. "Analysis at medium scale of low-resolution DInSAR data in slow-moving landslide-affected areas". ISPRS Journal of Photogrammetry and Remote Sensing, 64(6), 598-611. doi:10.1016/j.isprsjprs.2009.05.003

Cascini L., Fornaro G., Peduto D., 2010. Advanced low- and full-resolution DInSAR map generation for slow-moving landslide analysis at different scales, Engineering Geology 112: 29-42.

Centolanza G., Iglesias R., Monells D. Mallorqui J.J., 2012. A new approach to DInSAR pixel selection with a combined multi resolution selection method. Conference on Synthetic Aperture Radar, 2012. 9th European EUSAR, pp. 485 – 488.

Chan Y. K., Koo V. C., 2008. An introduction to Syntethic Aaperture Radar (SAR), Progress In Electromagnetics Research B, Vol. 2, pp. 27–60.

Colesanti C., Ferretti A., Prati C., Rocca F., 2003. Monitoring landslides and tectonic motion with the Permanent Scatterers technique. Engineering Geology 68(1–2), 3–14.

Colesanti, C., Wasowski, J., 2006. "Investigating landslides with space-borne Synthetic Aperture Radar (SAR) interferometry". Engineering Geology, 88, 173–199.

Costantini M., Falco S., Malvarosa F., Minati F., 2008. "A new method for identification and analysis of persistent scatterers in series of SAR images," in Proc. Int. Geosci. Remote Sensing Symp.(IGARSS), Boston MA, USA, 7-11 July 2008, pp. 449-452.

Cotecchia V., 1971. Su taluni problemi geotecnici in relazione alla natura del terreni della regione pugliese. Rivista Italiana di Geotecnica, I.

Cotecchia V., Melidoro G., 1974. Some principal geological aspects of the landslides of Southern Italy. Bulletin of Engineering Geology and the Environment, 9(1), 23-32.

Crosetto M., Castillo M., Arbiol R., 2003. Urban subsidence monitoring using radar interferometry: Algorithms and validation. Photogrammetric Engineering and Remote Sensing, 69 (7), pp. 775–783.

Crozier M.J., 1986. Landslides: Causes, Consequences & Environment. Croom Helm, London, England, p. 252.

Cruden D.M., 1991. A simple definition of a landslide. IAEG Bull., 43, 27-29.

Cruden D.M, Varnes D.J, 1996. Landslide types and processes. In: Turner AK, Schuster RL (eds) Landslides: investigation and mitigation (Special Report). Washington, DC, USA: National Research Council, Transportation and Research Board Special Report 247, pp 36–75.

Curlander J.C., R.N. McDounough, 1991. Synthetic Aperture Radar, Systems and Signal Processing, John Wiley&Sons, NewYork.

Delacourt C., Allemand P., Squarzoni C., Picard F., Raucoules D., Carnec C., 2004. Potential and limitation of ERS-Differential SAR Interferometry for landslide studies in the French Alps and Pyrenees. Proceedings of Fringe 2003 Workshop, SP-550, ESA (CD-ROM).

Del Prete M., Del Prete R.,2009. Classification, hazard and occurrence of flow-like mass movements in relation to the geology of a large area of Southern Italy. Journal of Technical and Environmental Geology. 1-2-3-4: 6-96.

Del Prete M., Trisorio Liuzzi G., 1981. Results of the preliminary study of the Calitri landslide (AV) mobilized by the 23/11/1980 earthquake, Geologia Applicata ed Idrogeologia, 16, p. 153–65, (in Italian).

Di Maio C., Vassallo R., Vallario M., Pascale S., Sdao, F., 2010. Structure and kinematics of a landslide in a complex clayey formation of the Italian Southern Apennines. Engineering Geology, 116: 311 – 322. DOI:10.1016/j.enggeo.2010.09.012.

Dikau R., Brunsden D., Schrott L., 1996. Landslide Recognition. Identification, Movement and Causes. M.-L. Ibsen (Eds.)Wiley & Sons, Chichester.

Doerry A.W. (2008). Reflectors for SAR Performance Testing. SANDIA REPORT SAND 2008-0396 Unlimited Release Printed January 2008.

Duro J., Closa J., Biescas E., Crosetto M., Arnaud A., 2005. High Resolution Differential Interferometry using time series of ERS and ENVISAT SAR data. Proc. of the 6th. Geomatic Week Conference, February 2005, Barcelona, Spain (CDROM).

Esu F., 1977. Behaviour of slopes in structurally complex formations. Proc. Int. Symp. “The geotechnics of Structurally Complex Formations”, Capri, 2, pp. 292–304.

Ferretti A., Prati C., Rocca F., 2000. Nonlinear subsidence rate estimation using permanent scatterers in differential SAR interferometry. IEEE Transactions on Geoscience and Remote Sensing, 38 (5), pp. 2202-2212.

Ferretti A., Prati C., Rocca F., 2001. Permanent scatterers in SAR interferometry. IEEE Transactions on Geoscience and Remote Sensing 39(1),8–20.

Ferretti A., Prati C., Rocca F., Casagli N., Farina P., Young B., 2005. Permanent Scatterers technology: a powerful state of the art tool for historic and future monitoring of landslides and other terrain instability phenomena. In: Hungr O, Fell R, Couture R, Eberhardt E (eds) International conference on landslide risk management. Taylor & Francis Ltd., Vancouver, pp 389–397.

Ferretti A., Savio G., Barzaghi R., Borghi A., Musazzi S., Novali F., Prati C. and Rocca F., 2007 Sub-millimeter Accuracy of InSAR Time Series: Experimental Validation. IEEE Transactions On Geoscience And Remote Sensing, VOL.45, NO.5, MAY 2007

Franceschetti, G. and R. Lanari, 1999. "Synthetic Aperture Radar Processing", CRC Press, Boca Raton (FL), March (1999), ISBN 8493-7899.

Franklin J.A., 1984. Slope instrumentation and monitoring. In: Brunsden D, Prior DB (eds) Slope instability. Wiley, New York, pp 143–170.

Fruneau B., Achache J., Delacourt C., 1996. Observation and modelling of the Saint-Etienne de Tinee landslide using SAR interferometry. Tectonophys, 265 (3–4), pp. 181–190.

Gabriel A. K., Goldstein R. M., Zebker H. A., 1989. Mapping small elevation changes over large areas: Differential interferometry, J. Geophys. Res., 94, 9183–9191, doi:10.1029/JB094iB07p09183.

Galloway D.L., Hudnut K.W., Ingebritsen S.E., Phillips S.P., Peltzer G., Rogez F., Rosen P.A., 1998. Detection of aquifer synthetic aperture radar, Antelope Valley, Mojave Desert, California. Water Resources Research, 34 (10), pp. 2573-2585.

Goldstein R. M., Engelhardt H., Kamb B., Frolich R. M., 1993. Satellite radar interferometry for monitoring ice sheet motion: application to an Antarctic ice stream. Science, 262 (5139), 1525-1530.

Guida D., Iaccarino G., Lazzari S., 1988. Map of the landslides of the upper Basento valley. In: Proceedings of the conference Ambiente Fisico Uso e Tutela del Territorio di Potenza. Italian National Centre of Research (CNR) Publication 1225.

Guida D., Iaccarino, G., 1991. Fasi evolutive delle frane tipo colata nell'alta valle del F. Basento (Potenza). Studi Trentini di Scienze Naturali. Acta Geologica, 68, pp. 127-152.

Hanssen R., 2001. Radar interferometry. Kluwer Academic Publishers, Dordrecht (The Netherlands).

Henderson F.M., Lewis, A.J., 1998. Principles and Application of Imaging Radar. Manual of Remote Sensing, 2. John Wiley and Sons, New York, 886 pp.

Herrera G., Tomás R., Lopez-Sanchez J.M., Delgado J., Vicente F., Mulas J., Cooksley G., Sanchez M., Duro J., Arnaud A., Blanco P., Duque S., Mallorquí J.J., De la Vega Panizo R., 2009. Comparison of advanced differential interferometry techniques: Murcia metropolitan area case study. ISPRS J Photogramm Remote Sens 64 (5): 501–512.

Herrera G., Notti D., García-Davalillo J.C., Mora O., Cooksley G., Sánchez M., Arnaud A., Crosetto M., 2010. Landslides analysis with C and X band satellite SAR data: the Portalet landslide area. Landslides 7:1–12.

Hilley G.E., Burgbman R., Ferretti A., Novali F., Rocca F., (2004). Dynamics of slow moving landslides from Permanent Scatterer Analysis. Science 304, 1952–1955.

Hooper A., Zebker H., Segall P., Kampes B., 2004. A new method for measuring deformation on volcanoes and other natural terrains using InSAR persistent scatterers, Geophys. Res. Lett., 31, L23611, doi:10.1029/2004GL021737.

Hooper A., 2008. A multi-temporal InSAR method incorporating both persistent scatterer and small baseline approaches, Geophys. Res. Lett., 35, L16302, doi:10.1029/2008GL034654.

Hu X. W., Tang H. M., Li J.S. 2008. General digital camera based experiments for large-scale landslide physical model measurement. In: Chen Z., Zhang J-M, Ho K, Wu F-Q, Li Z-K (eds). Landslides and engineered slopes: from the past to the future proceedings of the tenth international symposium on landslides and engineered slopes, pp 249–255.

Hungr O., Evans S. G., 1988. Engineering evaluation of fragmental rockfall hazards, Proceedings 5th International Symposium on Landslides, Lausanne, Switzerland, 1, 685–690.

Hutchinson J.N., Del Prete M., 1985. Landslides at Calitri, southern Apennines, reactivated by the earthquake of 23rd November 1980, Geologia Applicata ed Idrogeologia 20(1), p. 9–38.

Iglesias R., Monells D., Centolanza G., Lopez Dekker P., Mallorqui J.J., (2012). A new approach to DInSAR Pixel Selection with Spectral Correlation in Time between Sublooks. Proceedings EUSAR 2012, Nurberg Germany, pp. 665-668.

Jongmans D., Renalier F., Kniess U., Bièvre G., Schwartz S., Pathier E., Orengo Y., Villemin T., Delacourt C., 2008. Characterisation of the Avignonnet landslide (French Alps) using seismic techniques. In: Chen Z, Zhang J-M, Ho K, Wu F-Q, Li Z-K (eds) Landslides and engineered slopes: from the past to the future. Proceedings of the tenth international symposium on landslides and engineered slopes. Taylor & Francis, Xi'an, pp 395–401.

Joughin I., Winebrenner D., Fahnestock M., Kwok R., Krabill W., 1996. Measurement of ice-sheet topography using satellite radar interferometry. J. Glaciology, 42 (140).

Joughin I., Fahnestock M., Kwok R., Gogineni P., Allen C., 1999. Iceflow of Humboldt, Petermann, and Ryder Gletscher, northern Greenland. J. Glaciology, vol. 45, no. 150, pp. 231–241.

Keaton J.R., and DeGraff J.V., 1996. Surface observation and geologic mapping. In: Turner AK, Schuster RL (eds) Landslides: investigation and mitigation (Special Report). Washington, DC, USA: National Research Council, Transportation and Research Board Special Report 247, pp 178–230.

Kwok R., Fahnestock M.A., 1996. Ice sheet motion and topography from radar interferometry. IEEE Transactions on Geoscience and Remote Sensing, 34 (1), pp. 189-200.

Lanari R., Mora O., Manunta M., Mallorqui J.J., Berardino P., Sansosti E. 2004. A small baseline approach for investigating deformations on full resolution Differential SAR Interferograms. IEEE Transactions on Geoscience and Remote Sensing, 42: 1377–1386.

Leva D., Nico G., Tarchi D., Fortuny-Guasch J., Sieber A. J., 2003. Temporal analysis of a landslide by means of a ground-based SAR Interferometer. IEEE Trans. Geosci. Remote Sens., 41 41 4 Part 1, 745 752 , April 2003.

Liu S., Wang Z. 2008. Choice of surveying methods for landslides monitoring. In: Chen Z, ZhangJ-M, Ho K, Wu F-Q, Li Z-K (eds). Landslides and engineered slopes: from the past to the future. Proceedings of the tenth international symposium on landslides and engineered slopes. Taylor & Francis, Xi'an.

Lu Z., Mann, D., Freymueller J.T., Meyer D.J., 2000. Synthetic aperture radar interferometry of Okmok volcano, Alaska: Radar observations. Journal of Geophysical Research, 105 (B5), pp. 10791-10806.

Luzi G., Pieraccini M., Mecatti D., Noferini L., Macaluso G., Tamburini A., Atzeni C., 2007. Monitoring of an Alpine Glacier by Means of Ground-Based SAR Interferometry. Geoscience and Remote Sensing Letters, 4 3 July 2007 495 499 .

Maria F.A., Gianfranco F., Hélène V.I., 2004. Rock slope stability analysis based on photogrammetric surveys. In: Lacerda W., Ehrlich M. ,Fontoura S.A.B., Sayao A.S.(eds). Landslides: evaluation and stabilization. Ninth international symposium on landslides. A. A. Balkema Publishers, Leiden, pp 789–794.

Martino S., Scarascia Mugnozza G., 2005. The role of the seismic trigger in the Calitri landslide (Italy): historical reconstruction and dynamic analysis, Soil Dynamics and Earthquake Engineering, 25, p. 933–950.

Massonnet D., Rabaute T., 1993. Radar interferometry: Limits and potential. IEEE Trans. Geosci. Remote Sensing, 31 455 464 , Mar. 1993.

Massonnet D., Rossi M., Carmona C., Adragna F., Peltzer G., Feigl K., Rabaute T., 1993. The displacement field of the Landers earthquake mapped by Radar Interferometry. Nature, 364, pp. 138–142.

Massonnet D., Briole P., Arnaud A., 1995. Deflation of Mount Etna monitored by spaceborne radar interferometry, (Nature 375, 567-570).

Massonnet D., Thatcher W., Vadon H, 1996. Detection of postseismic fault zone collapse following the Landers earthquake. Nature, 382, pp. 489-497.

Massonnet D., Holzer T., Vadon H., 1997. Land subsidence caused by the East Mesa geothermal field, California, observed using SAR interferometry. Geophys. Res. Lett., 24 (8), pp. 901–904.

Massonnet D., Sigmundsson F., 2000. Remote sensing of volcano deformation by radar interferometry from various satellites. In: Mouginis-Mark et al. (eds), Remote sensing of active volcanism. Geophysical Monographs 116, American Geophysical Union, pp. 207-221.

McGuffey V., Modeer J., Victor A., Turner A.K., 1996. Subsurface exploration. In: Turner AK, Schuster RL (eds) Landslides: investigation and mitigation (Special Report). National Research Council, Transportation and Research Board Special Report 247, Washington, DC, USA, pp 231–277.

Meisina C., Zucca F., Fossati D., Ceriani M., Allievi J., 2006. Ground deformation monitoring by using the permanent scatterers technique: the example of the Oltrepo Pavese (Lombardia Italy). Eng Geol 87: 240–259.

Meisina C., Zucca F., Notti D., Colombo A., Cucchi A., Savio G., Giannico C., Bianchi M., 2008. Geological interpretation of PSInSAR data at regional scale. Sensors, 8, pp. 7469-7492.

Metternicht, G., Hurni, L., Gogu, R., 2005. Remote sensing of landslides: an analysis of the potential contribution to geospatial system for hazard assessment in mountainous environments. Remote Sensing of Environment, 98, pp. 284-303.

Mihalinec Z., Ortolan Z., 2008. Landslide ‘‘Granice’’ in Zagreb (Croatia). In: Chen Z, Zhang J-M, Ho K,Wu F-Q, Li Z-K (eds) Landslides and engineered slopes: From the past to the future. Proceedings of the tenth international symposium on landslides and engineered slopes. Taylor & Francis, Xi’an, pp 1587–1593.

Mikkelsen P.E., 1996. Field instrumentation. In: Turner AK, Schuster RL (eds) Landslides: investigation and mitigation (Special Report). National Research Council, Transportation and Research Board Special Report 247, Washington DC, USA, pp 278–316.

Mills J.P., Buckley S.J., Mitchell H.L., Clarke P.J., Edwards S.J., 2005. A geomatics data integration technique for coastal change monitoring. Earth Surf Proc Land 30 (6): 651–664.

Mohr J.J., Reeh N., Madsen S.N., 1998. Three-dimensional glacial flow and surface elevation measured with radar interf. Erometry. Nature, 391 (6664), pp. 273–276.

Mora O., Mallorquí J.J., and Broquetas A., “Linear and nonlinear terrain deformation maps from a reduced set of interferometric SAR images,” IEEE Trans. Geosci. Remote Sensing, vol. 41, pp. 2243-2253, Oct. 2003.

Nadim F., Kjekstad O., Peduzzi P., Herold C. and Jaedicke C., 2006. Global landslide and avalanche hotspots. Landslides, Vol. 3, No. 2, 159-174.

Olalla C., 2004. Recent developments in landslide monitoring. In: Lacerda W, Ehrlich M, Fontoura SAB, Sayao AS (eds) Landslides: evaluation and stabilization. Ninth international symposium on landslides. A.A. Balkema Publishers, Leiden, pp 549–555.

Oppikofer T., Jaboyedoff M., Baillifard F., Pedrazzini A. & Traveletti J., 2006. Interpretation of Laser Scanner 3D data used to determine circular failure surface of shallow landslides. In “Laser Scanner 3D”, 2nd European Optech Seminar, Milan, p. 7.

Oppikofer T., Jaboyedoff M., Blikra L.H. & Derron M.-H., 2008. Characterization and monitoring of the Åknes landslide using terrestrial laser scanning. Proc. 4th Canadian Conference on Geohazards: From Causes to Management, pp. 211-218.

Parise M., Wasowski J., 1998 Evolutive aspects and landslide activity in the surroundings of Calitri, Proc. Intern. Conf. on "La prevenzione delle catastrofi idrogeologiche: il contributo della ricerca scientifica", Alba, Italy, 5-7 November 1996, vol. 1, p. 135–144, (in Italian).

Parise M., Wasowski J., 1999. Landslide activity maps for landslide hazard evaluation: three case studies from Southern Italy, Natural Hazards, 20, p. 159-183.

Patacca E., Sartori R., Scandone P., 1990. Tyrrenian basin and apenninic arcs: kinematic relations since late Tortonian times. Memorie della Società Geologica Italiana, 45, 425-451

Pedersen R., Sigmundsson F., Feigl K.L., Árnadóttir T., 2001. Coseismic interferograms of two Ms=6.6 earthquakes in the South Iceland Seismic Zone, June 2000. Geophysical Research Letters, 28 (17), pp. 3341-3344.

Peltzer G., Rosen P.A.,1995. "Surface displacement of the 17 Eureka valley, California, earthquake observed by SAR interferometry, "Science, vol. 268, pp. 1333 – 1336, June 1995.

Peltzer G., Rosen P., Rogez F., Hudnut K., 1996. Post seismic rebound in fault step-overs caused by pore fluid flow. Science, 273, pp. 1202-1204.

Peltzer G., Crampé F., King G., 1999. Evidence of the nonlinear elasticity of the crust from Mw7.6 Manyi (Tibet) earthquake. Science, 286 (5438), pp. 272-276.

Peltzer G., Crampé F., Hensley S., Rosen R., 2001. Transient strain accumulation and fault interaction in the eastern California shear zone, Geology, 29, 975–978, *doi:*10.1130/0091-7613(2001)029<0975:TSAAFI>2.0.CO;2.

Perissin D., Prati C., Rocca F., 2009. PSInSAR Analysis over the Three Gorges Dam and urban areas in China. 2009 Urban Remote Sensing Joint Event

Perrone A., Iannuzzi A., Lapenna V., Lorenzo P., Piscitelli S., Rizzo E., Sdao F., 2004. High-resolution electrical imaging of the Varco d'Izzo earthflow (southern Italy). J Appl Geophys 56:17–29.doi:10.1016/j.jappgeo.2004.03.004

Pescatore T., Renda P., Schiattarella M., Tramutoli M., 1999. Stratigraphic and structural relationships between Mesocenozoic Lagonegro basin and coeval carbonate platforms in southern Italy. Tectono-physics 315: 286–295.

Plank S., Singer J., Minet C. & Thuro K. (2012) - Pre-survey suitability evaluation of the differential synthetic aperture radar interferometry method for landslide monitoring, Int. J. of Remote Sensing, 33(20), 6623-6637.

PODIS Project Campania, 2008. Technical descriptive notes of the elaboration made by the PODIS TELLUS Project (PON ATAS 2000-2006) on the PSinSAR data of Campania region. (http://www.difesa.suolo.regione.campania.it Last accessed: June 10, 2011). (in Italian)

Popescu M.E., Seve G., 2001. " Landslide Remediation Options After The International Decade For Natural Disaster Reduction (1990 - 2000), Keynote Lecture", Proc. Conf. Transition from Slide to Flow - Mechanisms and Remedial Measures, ISSMGE TC-11, Trabzon, 73-102

Prati C., A. Ferrett, Perissin D., 2010. Recent advances on surface ground deformation measurement by means of repeated space-borne SAR observations, J. Geodyn., 49, 161–170, *doi:*10.1016/j.jog.2009.10.011.

Proto M., Bavusi M., Bernini R., Bigagli L., Bost M., Bourquin F., Cottineau L.-M., Cuomo V., Vecchia P.D., Dolce M., Dumoulin J., Eppelbaum L., Fornaro G., Gustafsson M., Hugenschimdt J., Kaspersen P., Kim, H. Lapenna V., Leggio M., Loperte A., Mazzetti P., Moroni C., Nativi S., Nordebo S., Pacini F., Palombo A., Pascucci S., Perrone A., Pignatti S., Ponzo F.C., Rizzo E., Soldovieri F., Taillade F., 2010. Transport Infrastructure Surveillance and Monitoring by Electromagnetic Sensing: The ISTIMES Project. Sensors 2010, 10, 10620-10639.

Reilinger R.E., Ergintav S., Bürgmann S., McClusky S., Lenk O., Barka A., Gurkan O., Hearn L., Feigl K.L., Cakmak R., Aktug B., Ozener H., Töksoz M.N., 2000. Coseismic and postseismic fault slip for the 17 August 1999, M=7.5, Izmit, Turkey earthquake. Science, 289 (5484), pp. 1519-1524.

Reyes C.A., Fernandez L.C., 1996. Monitoring of surface movements in excavated slopes. In: Senneset K (ed). Landslides. Seventh international symposium on landslides. Balkema, Rotterdam, pp 1579–1584.

Rignot E.J., Gogineni S.P., Krabill W.B., Ekholm S., 1997. North and northeast Greenland ice discharges from satellite radar interferometry. Science, 276, pp. 934-937.

Rosen P.A., Hensley S., Joughin I.R., Li F.K., Madsen S.N., Rodriguez E., and Goldstein R., 2000. Synthetic aperture radar interferometry, IEEE Proc. 88, pp. 333-376.

Salvi S., Atzori S., Tolomei C., Allievi J., Ferretti A., Rocca F., Prati C., Stramondo S., Feuillet N., 2004. Inflation rate of the Colli Albani volcanic complex retrieved by the permanent scatterers SAR interferometry technique. Geophysical Research Letters, 31 (12), L12606.

Sarabandi, K., and T. C. Chiu, An optimum corner reflector for calibration of imaging radars, IEEE Trans. Antennas Propagation, submitted for publication (Feb. 1995).

Seymour M.S., Cumming I.G., 1994. "Maximum Likelihood Estimator for SAR Interferometry, "in Proc. 1994 Int. Geosci. Remote Sensing Symp. IGARSS 94, Pasadena, USA, 1994, p.2272-2275.2.5,6.2

Skepton A. W. and Hutchinson J. N. 1969. Stability of natural slopes and embankment foundations, in: Proceedings of the Seventh International Conference on Soil Mechanics and Foundation Engineering, Sociedad Mexicana de Mec´ana de Suelos, Mexico City,
State of the Art Volume, 291–340.

Smith M.J., Chandler J., Rose J., 2009. High spatial resolution data acquisition for the geosciences: kite aerial photography. Earth Surf Proc Land 34(1): 155–161.

Soeters R., VanWesten C.J., 1996. Slope instability recognition, analysis, and zonation. In: Turner AK, Schuster RL (eds). Landslides: investigation and mitigation (Special Report). National Research Council, Transportation and Research Board Special Report 247, Washington, DC, USA, pp 129–177.

Stabile T. A., Giocoli A., Perrone A., Palombo A., Pascucci S., Pignatti S., 2012. A new joint application of non-invasive remote sensing techniques for structural health monitoring J. Geophys. Eng. 9 S53 doi:10.1088/1742-2132/9/4/S53

Tarchi D., Ohlmer E., Sieber A. J., 1997. Monitoring of structural changes by radar interferometry. Res. Nondestruct. Eval. 9 213 225.

Tarchi, D., Casagli, N., Fanti, R., Leva, D., Luzi, G., Pasuto, A., Pieraccini, M., Silvano, S., 2003. Landslide monitoring by using ground-based SAR interferometry: An example of application to the Tessina landslide in Italy. Engineering Geology, 68 (1-2), pp. 15-30.

Terzaghi K., 1950. Mechanism of landslides, in Application of Geology to Engineering Practice, Berkey Vol., Geological Society of America, p.83-123.

Travelletti J., Oppikofer T., Delacourt C., Malet J.-P., Jaboyedoff M., 2008. Monitoring landslide displacements during a controlled rain experiment using a long-range terrestrial laser scanning (TLS). International Archives of Photogrammetry and Remote Sensing, 37 (Part B5), pp. 485-490.

T.R.E. (2008) PSInSARTM user's manual. TeleRilevamento Europa, Milan, Italy, 84 p. (in Italian).

Turner A.K., McGuffey V.C., 1996. Organization of investigation process. In: Turner AK, Schuster RL (eds) Landslides: investigation and mitigation (Special Report). National Research Council, Transportation and Research Board Special Report 247, Washington, pp 121–128.

Van Westen C.J., 2007. Mapping landslides: recent developments in the use of digital information. In: Turner A, Schuster RL (eds) Landslides and society ? Proceedings of the first North American conference on landslides, Vail, Colorado, USA, June 3–8, 2007. Association of Environmental and Engineering Geologists, Vail Colorado, USA, pp 221–238.

Varnes, D.J., 1978. Slope movement types and processes. In Special Report 176: Landslides: Analysis and control (R.L. Schuster and R.J. Krizek, eds), TRB, National Research Council, Washington, D.C., pp. 11-33.

Vezzani L., Ghisetti F. & Festa A., 2004. Carta Geologica del Molise. *S.EL.CA* , Florence, Scale 1:100,000.

Walstra J., Chandler J.H. , Dixon N., Dijkstra T.A., 2004. Extracting landslide movements from historical aerial photographs. In: Lacerda W, Ehrlich M, Fontoura SAB, Sayao AS (eds). Landslides: Evaluation and stabilization. Ninth international symposium on landslides. A.A. Balkema Publishers, Leiden, pp843–850.

Wasowski J., Lollino P., Limoni P.P., Del Gaudio V., Lollino G., Gostelow P., 2004. Towards an integrated field and EO-based approach for monitoring peri-urban slope instability. In: Lacerda W, Ehrlich M, Fontoura SAB, Sayao AS (eds). Landslides: evaluation and stabilization. Ninth international symposium on landslides. A.A. Balkema Publishers, Leiden, pp 809–816.

Webster T.L., Dias G., 2006. An automated GIS procedure for comparing GPS and proximal LiDAR elevations. Comput Geosci 32 (6): 713–726.

Werner C., Wegmüller U., Strozzi T., Wiesmann A., 2003. Interferometric point target analysis for deformation mapping. Proceedings of IGARSS, 21–25 July 2003, Toulouse (France), CDROM.

Wicks C., Thatcher W., Monastero F., Hasting M., 2001. Steady-state deformation of the Coso Range, East-Central California, inferred from satellite radar interferometry. Journal of Geophysical Research, 106 (B7), pp. 13769-13780.

Wright T., Parsons B., Fielding E., 2001. Measurement of interseismic strain accumulation across the North Anatolian Fault by satellite radar interferometry. Geophysical Research Letters, 28 (10), pp. 2117-2120.

Xia Y., Kaufmann H., and Guo X.F., 2004. Landslide monitoring in the Three Georges Area using D-InSAR and corner reflectors. Photogrammetric Engineering and Remote Sensing, 70/10, 1167-1172.

Yin J.H., Zhu H.H., Jin W., 2008. Monitoring of soil nailed slopes and dams using innovative technologies. In: Chen Z, Zhang J-M, Ho K, Wu F-Q, Li Z-K (eds) Landslides and engineered slopes: from the past to the future. Proceedings of the tenth international symposium on landslides and engineered slopes. Taylor &Francis, Xi'an, pp 1361–1366.

Zhang Q., Wang L., Zhang X.Y., Huang G.W., Ding X.L., Dai W.J., Yang W.T., 2008. Application of multi-antenna GPS technique in the stability monitoring of road side slopes. In: Chen Z, Zhang J-M, Ho K, Wu F-Q, Li Z-K (eds) Landslides and engineered slopes: from the past to the future. Proceedings of the tenth international symposium on landslides and engineered slopes. Taylor & Francis, Xi'an, pp 1367–1372.

Acknowledgements

Many people helped me throughout my PhD research. I am deeply grateful to all of them.

Prof. Antonio Iodice and Dr. Giuseppe Ruello (University of Naples) helped me understand the principles of Interferometry and satellite image processing, and provided very useful suggestions. I also wish to thank them and their team for having welcomed welcoming me in their Department.

Prof. Filippo Barattolo and Prof. Maurizio Fedi (University of Naples) coordinators of the PhD School, allowed me to enrich my studies with a challenging international experience.

Antonio Cammarota (University of Naples), precious for his willingness and for his expertise in field measurements.

Dr. Carmine Galzerano for his thorough knowledge of the Moio site.

Dr. Carmine Lucadamo, Dr. Gabriele De Luca, Dr. Pamela D'allestro and Dr. Serena Tessitore (and her sister Gabriella) for their crucial help during survey measurements.

Prof. Albert Aguasca, Prof. Xavier Fabregas and Dr. Carlos Lopez (UPC – Barcelona) gave me clarifying suggestions during the weekly SAR meetings at UPC.

Dr. Dani Monells (UPC – Barcelona) shered with me his knowledge and time and was of great help for every issue regarding SAR processing. But above all, he proved to be a real friend and warned me against Ruben's teasing! For all of this, I am very indebted with him.

Dr. Ruben Iglesias (UPC – Barcelona), as well as Dani, I really thank him for the talks about SAR processing, but especially for his special lessons of Spanish/Catalan. I will never forget his funny expressions in Spanish words! I also wish to thank his wife, Rachel, who showed kind affection to my family.

Dr. Alberto Alonso, Dr. Giuseppe Centolanza and Dr. Alba Yerro (UPC – Barcelona) I thank them very much for their help and for their support. Sharing the daily coffee break with them made the work very enjoyable! Thanks also to their girlfriend/boyfriend which showed howed kind affection to my family.

The eight months spent in Barcelona were simply unforgettable, and I wish to thank them and all the people I met there for the wonderful experience (Mrs Alicia, Dr. Esther Cantos, Dr. Beni Vazquez and Dr. Aynie Khoe) .

Last but not least, my supervisors:

Prof. Domenico Calcaterra (University of Naples) with whom I graduated and who has been my professional guide since then. For this research many thanks go to him also for the specific

agreement with the Ministry of Environment (MATTM) for the acquisition of PS interferometry data and of the related SAR images of the study sites.

Prof. Jordi J. Mallorqui (UPC - Barcelona) was my tutor during the eight-months period spent in Barcelona at UPC. I am very grateful to him for his warm welcome me, and for the stimulating discussions we had.

Dr. Ing. Massimo Ramondini (University of Naples) followed passionately all my research project and made this work possible. Thanks for all!

And finally....

My sister Paola and my sister in law Marina because without their I should be “dumbfounded”.

Finally, my deepest gratitude goes to my family who made my life happy. For them, only few words: Valeria, Fabio and Paolo thanks for being you.